

**THE DOPING DEPENDENCE OF THE OPTICAL PROPERTIES
OF HIGH-TEMPERATURE SUPERCONDUCTORS.**

By

ANTON V. PUCHKOV, B.Sc.

A Thesis
Submitted to the School of Graduate Studies
in Partial Fulfilment of the Requirements
for the Degree
Doctor of Philosophy

McMaster University
© Copyright by Anton V. Puchkov, 1996.

OPTICAL PROPERTIES OF HIGH- T_c SUPERCONDUCTORS

DOCTOR OF PHILOSOPHY (1996)
(Physics)

McMaster University
Hamilton, Ontario

TITLE: The doping dependence of the optical properties of high-temperature superconductors.

AUTHOR: Anton V. Puchkov, B.Sc. (Moscow Institute for Physics and Technology)

SUPERVISOR: Professor T. Timusk

NUMBER OF PAGES: x, 111

Abstract

The phenomenon of high-temperature superconductivity (HTSC) is one of the most intensively studied ones in the modern condensed matter physics. The initial drive to produce a room-temperature superconductor led to the discovery of completely new physics, that can not be explained by the existing theories. This includes not only the properties of HTSC materials in the superconducting state but in the normal state as well. In fact, much of the current research effort is aimed at the understanding of the unconventional normal-state properties of HTSC materials, in a hope that this understanding will unlock the mystery of the superconductivity phenomenon.

The superconducting transition temperature of a HTSC material can be changed by chemical doping. While at the initial stages of the HTSC research the research effort was focused on the so-called "optimal" doping regime, the one with a highest superconducting transition temperature, recently attention has begun shifting towards the whole doping range.

The work, results of which are presented in this thesis, is aimed at the understanding of the doping dependence of the optical properties of the high-temperature superconducting materials. In particular, we are interested in the infrared energy range since it provides a wealth of information about the low-energy electronic excitations. Mostly the normal-state properties were studied. Several materials studied in this work allowed us to cover the whole metallic doping range of HTSC. The main emphasis of the work presented in this thesis is, however, the "overdoped" regime, where the transition temperature decreases as the material becomes a better metal. This part of the HTSC phase diagram was largely ignored before. We believe therefore, that the new results, presented in this thesis, are an important contribution to the general effort in the field of high-temperature superconductivity research.

Acknowledgements

I would like to thank my supervisor, Tom Timusk, for his guidance and continued support during the last four years. His many suggestions and discussions are a very valuable contribution.

I would also like to thank Dimitry Basov, for his help and for teaching me the art of infrared spectroscopy.

Over the last several years I have enjoyed illuminating discussions with a number of people. In particular, many wonderful discussions with J.P. Carbotte and C.C. Kallin are very much appreciated. I would also like to thank all the faculty members, post docs and graduate students at the *Physics Department* for answering all my questions.

I would like to thank C.V. Stager for the magnetic susceptibility measurements.

I am grateful to Andy Duncan for keeping the lab in order and for his computer expertise, and to Gord Hewitson for supplying the liquid helium.

I am very grateful to the secretaries in the *Physics office*: Rose McNiece, Wendy Malarek, and Marg Wilby; for the much appreciated help with the endless paperwork.

I would like to thank Tatiana Startseva for her help with the manuscript preparation.

Finally, my warmest thanks to Anya Rivkin, for her patience and tolerance of the strange working hours.

Preface

This thesis is a result of the author's experimental work in the field of optical spectroscopy of high-temperature superconductivity phenomenon. As any experimental work, it involved an extensive collaboration with other research groups. Below we briefly list the people who participated in the work, as well as their personal contribution.

The material presented in chapter 2 is based on the original work by A.V. Puchkov, P. Fournier, T. Timusk, and N.N. Kolesnikov [Puchkov96c]). The infrared optical measurements were performed by A.V. Puchkov and T. Timusk, the Bi2212 single crystals were grown by P. Fournier and Tl2201 single crystals were grown by N.N. Kolesnikov. The text of the paper was written by A.V. Puchkov.

The work presented in chapter 3 is a part of a broader review article entitled "*Pseudogap state in high- T_c Superconductors: an Infrared Study*" by A.V. Puchkov, D.N. Basov, and T. Timusk. [Puchkov96d] While the manuscript was in a process of refereeing at the time of writing this thesis, no copyright transfer has been made. The author of this thesis performed reflectivity measurements on Bi2212, (Bi/Pb)2212, and Tl2201 materials. The measurements on Y123 and Y124 materials were performed by D.N. Basov and are reproduced in this thesis, with permission of D.N. Basov and appropriate annotation, to give a reader a broader view on the subject.

Chapter 4 consists of two articles, one has been published in Physical Review B [Puchkov95c] and another one [Puchkov96a] is to appear in Physical Review B **54**, p. 6686, 1996. The work was done in collaboration with a research group from the University of Illinois at Urbana-Champaign. The single crystals of BKBO at different doping levels were grown by P.D. Han and D.A. Payne, while the ellipsometric measurements were performed by M.A. Karlow and S.L. Cooper.

Contents

1	Introduction	1
1.1	Optical Properties of Solids	1
1.1.1	Maxwell's equations and the dielectric function	1
1.1.2	Kramers Kronig relations	6
1.1.3	Sum rules	7
1.1.4	The classical theory of metals	8
1.1.5	Bound electrical charges	10
1.1.6	The method of infrared reflectance spectroscopy	11
1.2	The superconductivity phenomenon: an optical perspective	14
1.2.1	Conventional superconductivity	14
1.2.2	High-temperature superconductivity	18
2	Doping dependence of the free-carrier density in high-T_c superconductors: Optical results	26
2.1	Introduction	26
2.2	Experimental details	27
2.3	Experimental results	28
2.4	Discussion	32
3	The pseudogap state in the cuprate high-T_c superconductors	38
3.1	Introduction	38
3.2	Experimental details	43
3.3	Experimental results	44
3.3.1	Underdoped cuprates.	44
3.3.2	Optimally doped and lightly overdoped cuprates.	49
3.3.3	Overdoped cuprates.	53
3.4	Discussion	56
3.4.1	General trends in $1/\tau(\omega)$ data.	56
3.4.2	Theoretical models for $1/\tau(\omega)$	59
3.4.3	The relation between ab -plane and c -axis pseudogap.	66

3.4.4	The superconducting state	66
3.4.5	Open questions	67
3.5	Conclusions	69
4	The non-cuprate high-T_c superconductor $Ba_{1-x}K_xBiO_3$	70
4.1	Introduction	70
4.2	Optical conductivity of non-metallic $Ba_{0.69}K_{0.31}BiO_3$ single crystals: Evidence for bipolaron formation. . .	72
4.3	The doping dependence of the optical properties of $Ba_{1-x}K_xBiO_3$. .	77
A	The extended Drude formalism	85
A.1	The Complex Memory Function.	85
A.2	Electron-boson scattering.	90
B	Some useful information	97
B.1	Energy units:	97
B.2	Material abbreviations:	97

List of Tables

3.1	The linear-fit parameters for the high-frequency $1/\tau(\omega)$	57
-----	---	----

List of Figures

1.1	The frequency dependence of the real and imaginary parts of optical conductivity given by the Drude theory.	9
1.2	The frequency dependence of the real and imaginary parts of optical conductivity given by the oscillator model.	11
1.3	Sketch of the experimental geometry used in the reflectance spectroscopy	12
1.4	A sketch of the renormalization of a one-particle density of states upon entering the superconducting state in the BCS theory.	15
1.5	Real and imaginary parts of the optical conductivity of a superconductor, calculated from the Mattis-Bardeen theory.	16
1.6	A comparison of T_c with the free-carrier density in a superconductor.	19
1.7	Crystal structure of Tl2201 and Bi2212.	20
1.8	T_c vs. doping level in high-temperature superconductors.	22
1.9	The typical spectrum of the real part of the optical conductivity of a HTSC material in the normal and the superconducting states.	24
2.1	The optical conductivity of Bi2212 at several doping levels.	29
2.2	The optical conductivity of Tl2201 at several doping levels.	31
2.3	The relative changes in the low-frequency conductivity spectral weight for several HTSC material series as a function of T_c	33
2.4	Evolution of optical conductivity as a function of a band filling in a simple two-band structure.	36
3.1	Schematic phase diagram of the cuprate superconductors.	39
3.2	The c-axis conductivity of an underdoped Y123 crystal.	42
3.3	Absorption and optical conductivity for underdoped Bi2212.	45
3.4	Memory function for underdoped cuprates.	47
3.5	Absorption and optical conductivity for optimally doped Y123.	50
3.6	Memory function for optimally doped cuprates.	52
3.7	Absorption and optical conductivity for overdoped Tl2201.	54
3.8	Memory function for overdoped cuprates.	55

3.9	Optical response functions for optimally doped Y123, broad frequency range.	61
3.10	An estimated boson spectral density in the pseudogap state.	63
4.1	The crystal structure of BKBO in the metallic doping regime.	71
A.1	Electron-boson model calculations with boson spectral density $\mathcal{A}_{tr}(\omega) = \omega_0\delta(\omega - \omega_0)$	93
A.2	Electron-boson model calculations with a "square" spectrum for the boson spectral density.	94
A.3	Electron-boson model calculations for the "magnetic" boson spectral density.	96

Chapter 1

Introduction

1.1 Optical Properties of Solids

1.1.1 Maxwell's equations and the dielectric function

Since this topic is described in detail in several publications, [Ashcroft76, Kittel86, Wooten72, Landau84] for the reader's convenience, we will only reproduce the essential highlights of the theory.

We start with Maxwell's equations in macroscopic form (in Gaussian units):

$$\vec{\nabla} \cdot \vec{E} = 4\pi\rho \quad (1.1)$$

$$\vec{\nabla} \times \vec{E} = -\frac{1}{c} \frac{\partial \vec{B}}{\partial t} \quad (1.2)$$

$$\vec{\nabla} \cdot \vec{B} = 0 \quad (1.3)$$

$$\vec{\nabla} \times \vec{B} = \frac{1}{c} \frac{\partial \vec{E}}{\partial t} + \frac{4\pi}{c} \vec{J}, \quad (1.4)$$

where \vec{E} and \vec{B} are the electric and magnetic fields respectively, ρ and \vec{J} are respectively the total charge and current densities and c is the speed of light in a vacuum.

There are two contributions to the charge density ρ . The first one is due to polarization of the medium in the presence of an electro-magnetic field and is given by $-\vec{\nabla} \cdot \vec{P}$, where \vec{P} is the dipole moment per unit volume. The second one is a contribution due to external charges, ρ^{ext} .

The local current density consists of four contributions: (i) The electric current

$\partial\vec{P}/\partial t$ due to the time-dependence of the polarization \vec{P} in the presence of time-varying electric field; (ii) the magnetic induction current, given by $c(\vec{\nabla} \times \vec{M})$ where \vec{M} is the magnetic dipole moment per unit volume; (iii) the electric current due to the conduction electrons, $\vec{J}^{cond} = \sigma_{dc}\vec{E}$, where σ_{dc} is the dc conductivity; and (iv) external current sources.

We will first consider the quasistatic case of a slowly varying electromagnetic field, so that the frequency of the electromagnetic radiation is small compared to the characteristic relaxation frequencies of the processes that determine the electrical and magnetic polarization of a media. In this case we can introduce the following definitions:

$$\vec{D} = \vec{E} + 4\pi\vec{P} = \epsilon\vec{E}, \quad (1.5)$$

$$\vec{H} = \vec{B} - 4\pi\vec{M} = \frac{1}{\mu}\vec{B} \quad (1.6)$$

where *constants* ϵ and μ are the static dielectric constant and the magnetic permeability, respectively. Assuming no external charges, we arrive at the set of Maxwell's equations for an isotropic material¹:

$$\vec{\nabla} \cdot \epsilon\vec{E} = 0 \quad (1.7)$$

$$\vec{\nabla} \times \vec{E} = -\frac{\mu}{c} \frac{\partial \vec{H}}{\partial t} \quad (1.8)$$

$$\vec{\nabla} \cdot \mu\vec{H} = 0 \quad (1.9)$$

$$\vec{\nabla} \times \vec{H} = \frac{\epsilon}{c} \frac{\partial \vec{E}}{\partial t} + \frac{4\pi\sigma_{dc}}{c} \vec{E}. \quad (1.10)$$

Using the Maxwell's equation and the vector identity

$$\vec{\nabla} \times (\vec{\nabla} \times \vec{A}) = \vec{\nabla}(\vec{\nabla} \cdot \vec{A}) - \nabla^2 \vec{A} \quad (1.11)$$

we obtain the wave equations:

¹In an anisotropic material μ , ϵ and σ_{dc} are replaced by the corresponding tensors

$$\nabla^2 \vec{E} = \frac{\epsilon\mu}{c^2} \frac{\partial^2 \vec{E}}{\partial t^2} + \frac{4\pi\sigma_{dc}\mu}{c^2} \frac{\partial \vec{E}}{\partial t} \quad (1.12)$$

$$\nabla^2 \vec{H} = \frac{\epsilon\mu}{c^2} \frac{\partial^2 \vec{H}}{\partial t^2} + \frac{4\pi\sigma_{dc}\mu}{c^2} \frac{\partial \vec{H}}{\partial t}. \quad (1.13)$$

We now look for a solution to Eqs. 1.12,1.13 with time dependence $\exp(-i\omega t)$:

$$-\nabla^2 \vec{E} = \frac{\omega^2}{c^2} \mu \left(\epsilon + i \frac{4\pi\sigma_{dc}}{\omega} \right) \vec{E} \quad (1.14)$$

$$-\nabla^2 \vec{H} = \frac{\omega^2}{c^2} \mu \left(\epsilon + i \frac{4\pi\sigma_{dc}}{\omega} \right) \vec{H}. \quad (1.15)$$

Since $\vec{\nabla} \cdot \vec{E} = 0$ and $\vec{\nabla} \cdot \vec{H} = 0$, the solution of Eqs. 1.14,1.15 is necessarily transverse, that is the directions of the electrical and magnetic fields are always perpendicular to the direction of propagation.

In the low-frequency limit there is a distinction between an insulator and a metal. In case of an insulator $\sigma_{dc} = 0$ and Eq. 1.14 reduces to the following:²

$$-\nabla^2 \vec{E} = \omega^2 \frac{\mu\epsilon}{c^2} \vec{E}. \quad (1.16)$$

This is the equation for an electromagnetic wave propagating in a non-absorbing medium. One can see that the velocity of the wave is given by $v = c(\epsilon\mu)^{-1/2}$.

Let us now consider the case of electromagnetic fields of frequencies high enough to be comparable to the relaxation frequencies in the medium, and the corresponding dispersion effects for $\epsilon(\omega)$ and $\mu(\omega)$. To begin with, it is obvious that at extremely high frequencies, when the wavelength of an electromagnetic wave, λ , becomes comparable to the interatomic distances in a material, a , the macroscopic description in terms of ϵ and μ becomes invalid. Still, there is always a large frequency range where, on the one hand, dispersion phenomena are important, and, on the other hand, the macroscopic description is valid. For example, the fastest relaxation time in solids is electronic, with a characteristic time of the order of a/v_e , where v_e is a typical electronic speed. However, since $v_e \ll c$, the corresponding wavelength $\lambda \sim ac/v_e$ is still much larger than a .

²From now on we will only show equations for \vec{E} since equations for \vec{H} are similar

Unlike $\epsilon(\omega)$, the magnetic permeability $\mu(\omega)$ loses its physical meaning already at relatively low frequencies. Without elaborating, we state that taking into account deviations of $\mu(\omega)$ from 1 at optical frequencies is, strictly speaking, unjustified [Landau84].

In the limit discussed in the previous paragraph, and assuming that the field intensity is small enough so that relation between \vec{D} and \vec{E} is linear, we can write:

$$\vec{D}(t) = \vec{E}(t) + \int_0^\infty f(\tau)\vec{E}(t-\tau)d\tau. \quad (1.17)$$

Here $f(\tau)$ is determined by the medium. After a Fourier transform we arrive at:

$$\vec{D} = \epsilon(\omega)\vec{E}, \quad (1.18)$$

$$\epsilon(\omega) = 1 + \int_0^\infty f(\tau)e^{i\omega\tau}d\tau \quad (1.19)$$

Therefore, if the frequency of the incident electromagnetic wave is comparable to the relaxation frequencies in the medium, ϵ in Maxwell's equations must be replaced by $\epsilon(\omega)$. The $\epsilon(\omega)$ is in principle complex: $\epsilon(\omega) = \epsilon_1(\omega) + i\epsilon_2(\omega)$. From the Eq. 1.19 one can immediately see that:

$$\epsilon_1(-\omega) = \epsilon_1(\omega), \epsilon_2(-\omega) = -\epsilon_2(\omega). \quad (1.20)$$

Therefore, while the real part of $\epsilon(\omega)$ is even, the imaginary part is odd.

In the limit of low frequencies compared to the onset of a dispersion, and if $\epsilon(\omega)$ is a smooth function, $\epsilon(\omega)$ can be expanded in powers of ω .³ The expansion of $\epsilon_1(\omega)$ contains only even powers while expansion of $\epsilon_2(\omega)$ contains only odd powers. In a dielectric material, $\epsilon_1(\omega)$ approaches the static dielectric constant, ϵ , while expansion of $\epsilon_2(\omega)$ starts in principle from a term proportional to ω .

One can consider $\epsilon(\omega)$ at low frequencies in conductors as well. However, in this case, to preserve the form of Eq. 1.16, an additional imaginary term $i4\pi\sigma_{dc}/\omega$,

³Obviously, this is not true if $\epsilon(\omega)$ has a singularity at the energy corresponding to the beginning of dispersion. Such is the case of a van Hove singularity in a joint density of states for an interband transition where, in a simplest case, $\epsilon_2(\omega) \sim (\omega - E_g)^{1/2}$ at $\omega > E_g$ and $\epsilon_2(\omega) = 0$ at $\omega < E_g$ where E_g is the interband gap energy. [Lynch85]

due to the conduction electrons, has to be added to the dielectric function (compare Eq.'s 1.14,1.16). This means that in a good conductor, propagation of a low-frequency electromagnetic wave is dissipative. The next term in $\epsilon(\omega)$ is a real constant which, however, does not have the same physical meaning as in dielectrics. Recognizing the difference between a metal and an insulator, the wave equation can be written in a more general form:

$$-\nabla^2 \vec{E} = \frac{\omega^2}{c^2} \epsilon(\omega) \vec{E}. \quad (1.21)$$

In the opposite limit of very high frequencies, $\epsilon(\omega)$ approaches unity. This has a simple physical meaning: for a sufficiently rapidly varying field the polarization processes, which lead to \vec{E} being different from \vec{D} , do not have enough time to develop. At a sufficiently high frequency of an electromagnetic field, all (or almost all) of the electrons in a medium (including the inner-shell) may be considered as free electrons, and their interactions with each other and with nuclei can be neglected. In this case a solution of a kinetic equation (for a more thorough discussion please see section 1.1.4) gives:

$$\lim_{\omega \rightarrow \infty} \epsilon(\omega) = 1 - \frac{4\pi n e^2}{m_e \omega^2}, \quad (1.22)$$

where n is the *total* density of electrons in the medium and m_e is the electronic mass. At high frequencies there is no distinction between dielectric and conducting materials. Of course, for $\epsilon(\omega)$ to have the same physical meaning as in Maxwell's equations, the frequency must not be too large:⁴ $\omega < c/a$.

The complex index of refraction, $N(\omega)$, is given by:

$$N(\omega) = n(\omega) + ik(\omega) = (\epsilon_1(\omega) + i\epsilon_2(\omega))^{1/2}, \quad (1.23)$$

so that

$$\epsilon_1(\omega) = n^2(\omega) - k^2(\omega) \quad (1.24)$$

$$\epsilon_2(\omega) = 2n(\omega)k(\omega). \quad (1.25)$$

⁴However, even if the frequency does not satisfy this requirement, $\epsilon(\omega)$ may have a well-defined physical meaning [Landau84]

Finally, the power absorption coefficient is:

$$\alpha(\omega) = \frac{2\omega}{c}k(\omega) = \frac{\omega\epsilon_2(\omega)}{cn}. \quad (1.26)$$

From the last equation one can see that it is the imaginary part of the dielectric function that is responsible for a dissipation of energy.

1.1.2 Kramers Kronig relations

It can be shown [Kittel86, Landau84] that any complex function, $f(\omega) = \text{Re}f(\omega) + i\text{Im}f(\omega)$, that satisfies the following conditions: (i) The poles of $f(\omega)$ are below the real axis; (ii) $f(\omega) \rightarrow 0$ uniformly as $|\omega| \rightarrow \infty$; (iii) The function $\text{Re}f(\omega)$ is even and $\text{Im}f(\omega)$ is odd with respect to real ω ; also satisfies the Kramers-Kronig relations:

$$\text{Re}f(\omega) = \frac{1}{\pi} \mathcal{P} \int_{-\infty}^{\infty} \frac{\Omega \text{Im}f(\Omega)}{\Omega - \omega} d\Omega \quad (1.27)$$

$$\text{Im}f(\omega) = -\frac{\omega}{\pi} \mathcal{P} \int_{-\infty}^{\infty} \frac{\text{Re}f(\Omega)}{\Omega - \omega} d\Omega \quad (1.28)$$

Here, \mathcal{P} means "principal part".

The Kramers-Kronig (KK) relations are extremely important in the analysis of optical experiments in solids since they enable us to find the real part of the response of a linear passive system if we know the imaginary part of the response at all frequencies, and vice versa. Despite the somewhat complicated mathematical representation, the physical meaning behind the KK relations is simple and fundamental: they are a direct consequence of the causality principle. Therefore, any physical response function that satisfies the KK relations is said to be causal.

In particular, the dielectric function is causal:

$$\epsilon_1(\omega) - 1 = \frac{2}{\pi} \mathcal{P} \int_0^{\infty} \frac{\Omega \epsilon_2(\Omega)}{\Omega^2 - \omega^2} d\Omega \quad (1.29)$$

$$\epsilon_2(\omega) = -\frac{2\omega}{\pi} \mathcal{P} \int_0^{\infty} \frac{\epsilon_1(\Omega) - 1}{\Omega^2 - \omega^2} d\Omega + \frac{4\pi\sigma_{dc}}{\omega}. \quad (1.30)$$

Therefore, the real and imaginary parts of $\epsilon(\omega)$ are not independent, rather one follows from the knowledge of the other *over the whole frequency range*. However, the last

condition is not likely to be satisfied in a real experimental situation. In the above equations we have used the properties of $\epsilon(\omega)$ represented by Eq. 1.20. Also, the second term on the right-hand side of Eq. 1.30 appears only for metals.

In the case of metals it is customary to consider the complex optical conductivity $\sigma(\omega) = \sigma_1(\omega) + i\sigma_2(\omega)$ instead of $\epsilon(\omega)$. The relation between the two can be written as:

$$\sigma(\omega) = i\frac{\omega}{4\pi}(1 - \epsilon(\omega)). \quad (1.31)$$

Therefore, the real part of optical conductivity is defined as $\sigma_1(\omega) = \omega\epsilon_2(\omega)/(4\pi)$ and the imaginary part is $\sigma_2(\omega) = \omega(1 - \epsilon_1(\omega))/(4\pi)$. The KK relations for the optical conductivity are:

$$\sigma_2(\omega) = \frac{2\omega}{\pi} \mathcal{P} \int_0^\infty \frac{\sigma_1(\Omega)}{\omega^2 - \Omega^2} d\Omega \quad (1.32)$$

$$\sigma_1(\omega) = \frac{2\omega^2}{\pi} \mathcal{P} \int_0^\infty \frac{\sigma_2(\Omega)/\Omega}{\Omega^2 - \omega^2} d\Omega + \sigma_{dc}. \quad (1.33)$$

Obviously, in the limit of $\omega \rightarrow 0$ the real part of optical conductivity is just the dc conductivity, σ_{dc} .

1.1.3 Sum rules

The sum rules for different optical response functions are fundamental tools of optical spectroscopy. The most important of the sum rules, the conductivity f sum rule, can be obtained as follows. In the expression for $\epsilon_1(\omega)$ at high enough frequencies we can neglect Ω in the denominator. In this case:

$$\epsilon_1(\omega) - 1 = -\frac{2}{\omega^2\pi} \int_0^\infty \Omega\epsilon_2(\Omega) d\Omega. \quad (1.34)$$

On the other hand, for the dielectric function at very high frequencies we have Eq. 1.22. Comparing the two equations we obtain the f sum rule:

$$\frac{1}{4\pi} \int_0^\infty \omega\epsilon_2(\omega) d\omega = \int_0^\infty \sigma_1(\omega) d\omega = \frac{\pi e^2 n}{2m}, \quad (1.35)$$

where n is the density of all electrons in the material and m is the bare electron mass.

Other important sum rules, which we present without derivation, include the following: [Smith85]

$$\int_0^\infty (1 - \epsilon_1(\omega))d\omega = 4\pi \int_0^\infty \frac{\sigma_2(\omega)}{\omega}d\omega = 2\pi^2\sigma_{dc}, \quad (1.36)$$

$$\int_0^\infty \omega k(\omega)d\omega = \frac{\pi^2 ne^2}{m}, \quad (1.37)$$

$$\int_0^\infty (n(\omega) - 1)d\omega = 0. \quad (1.38)$$

1.1.4 The classical theory of metals

The simplest model for the optical response of a metal was developed by Drude and Sommerfeld [Kittel86]. According to this model, when the electrons in a metal are subjected to an external field the entire Fermi surface is displaced rigidly in a direction opposite to the field by an amount proportional to the current density. The corresponding equation of motion for the momentum \vec{p} per electron in a material subjected to an electromagnetic field, $\vec{E} = \vec{E}_0 \exp(-i\omega t)$, is:

$$\frac{d\vec{p}}{dt} = -\frac{\vec{p}}{\tau} - e\vec{E}. \quad (1.39)$$

Here $1/\tau$ is a constant scattering rate (and τ is an electronic life time), determined by impurities ($1/\tau_i$), sample surface ($1/\tau_d$), phonons ($1/\tau_{ph}$), other electrons ($1/\tau_e$), etc. All these contributions are generally independent, so the scattering rates add:

$$1/\tau = 1/\tau_i + 1/\tau_d + 1/\tau_{ph} + 1/\tau_e. \quad (1.40)$$

We note that the last two contributions may become temperature (and/or frequency) dependent at high temperatures and frequencies. However, for the moment we will assume that $1/\tau$ is independent of frequency while the other case will be discussed in section 3 and appendix A. It can be easily shown [Ashcroft76] that a solution to equation 1.39 with the periodicity of an applied field, $\exp(-i\omega t)$, gives the expression for the optical conductivity:

$$\sigma(\omega) = \frac{\sigma_{dc}}{1 - i\omega\tau}, \quad (1.41)$$

where $\sigma_{dc} = ne^2\tau/m$ is the dc conductivity. If an optical conductivity has the shape given by Eq. 1.41, it is said to be Drude-like. The real and imaginary part of optical conductivity are given by:

$$\sigma_1(\omega) = \frac{\omega_p^2}{4\pi} \frac{\tau}{1 + \omega^2\tau^2} \quad (1.42)$$

$$\sigma_2(\omega) = \frac{\omega_p^2}{4\pi} \frac{\omega\tau}{1 + \omega^2\tau^2}. \quad (1.43)$$

Here, $\omega_p = 4\pi ne^2/m$ is the plasma frequency of the free carriers. An example of the frequency dependence given by Eq.s 1.42 and 1.43 is shown in Fig. 1.1.

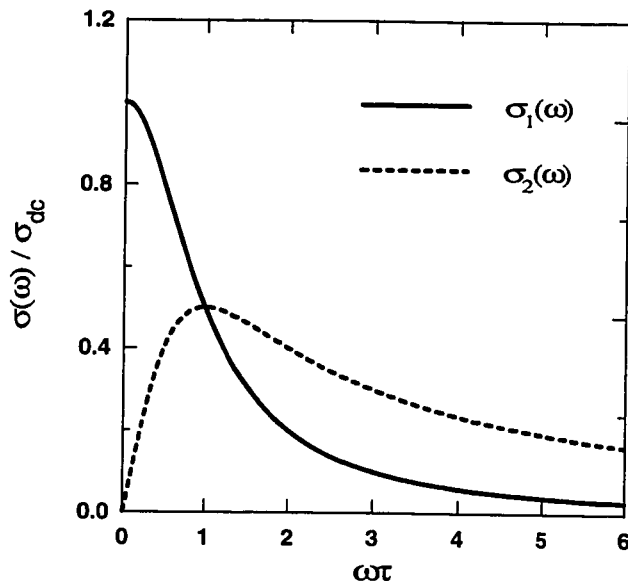


Figure 1.1: The frequency dependence of the real and imaginary parts of optical conductivity given by the Drude theory.

If the frequency ω is high enough to satisfy $\omega\tau \gg 1$, and recalling the definition of $\sigma(\omega)$, Eq. 1.31, we obtain:

$$\epsilon(\omega) = 1 - \frac{\omega_p^2}{\omega^2} \quad (1.44)$$

Therefore, at frequencies $\omega < \omega_p$ the dielectric function is real and negative. The solution for Eq. 1.21 decays exponentially in this case, *i.e.* no radiation can

propagate. One can estimate the penetration depth of an electromagnetic wave into a metal at frequencies $1/\tau \ll \omega \ll \omega_p$. Solving Eq. 1.21 with $\epsilon(\omega) = -\omega_p^2/\omega^2$ we obtain:

$$\vec{E} = \vec{E}_0 \exp\left(-\frac{z}{\delta} - i\omega t\right), \quad (1.45)$$

where z is the direction of propagation, normal to the metal surface, and $\delta = c/\omega_p$ is the penetration depth. When $\omega > \omega_p$, $\epsilon(\omega)$ is positive and the metal should become transparent.

1.1.5 Bound electrical charges

Eq. 1.39 can be extended to include bound charges present in a system, such as phonons or bound electrons. In this case one can assume that the charges are bound by a harmonic potential to a site in the solid and that the motion in this potential is subject to a viscous force. The equation of motion is given by:

$$\begin{aligned} m \frac{d^2 \vec{x}}{dt^2} &= -\frac{m}{\tau} \frac{d\vec{x}}{dt} - m\omega_e^2 \vec{x} - e\vec{E} \\ \vec{p} &= m \frac{d\vec{x}}{dt} \end{aligned} \quad (1.46)$$

Here, ω_e is the center frequency and $1/\tau$ is a damping constant.

Again, looking for a solution with time dependence $\exp(-i\omega t)$, we obtain for the optical conductivity:

$$\sigma(\omega) = \frac{\omega_p^2}{4\pi} \frac{\omega}{i(\omega_e^2 - \omega^2) + \omega/\tau}. \quad (1.47)$$

Here, ω_p is a plasma frequency, or oscillator strength. It is given by $\omega_p^2 = 4\pi n_0 e^2/m$, where n_0 is the number density of oscillators and m is their effective mass. In the limiting case of $\omega_e = 0$ one obtains expression 1.41.

Eq. 1.47 can be applied to phonons, in which case ω_e is the phonon frequency and $1/\tau$ is the phonon damping. In the case of applying Eq. 1.47 to an interband transitions it is tempting to associate ω_e with the interband energy gap and $1/\tau$ with the lifetime of the excited carriers. The association is valid only if the width of the band is a result of lifetime effects, as in atomic absorption. If, however, the width

is due to the initial and final states being located in broad bands, the association is invalid. In this case, the gap should be associated with the onset of the absorption rather than with its center frequency. [Lynch85]

An example of the frequency dependence given by Eq. 1.47 is shown in Fig. 1.2. The optical conductivity is additive so that, for example, the spectrum corresponding to a metal with an interband transition can be modeled by a sum of the spectra shown in Fig.'s 1.1 and 1.2 (with appropriate parameters).

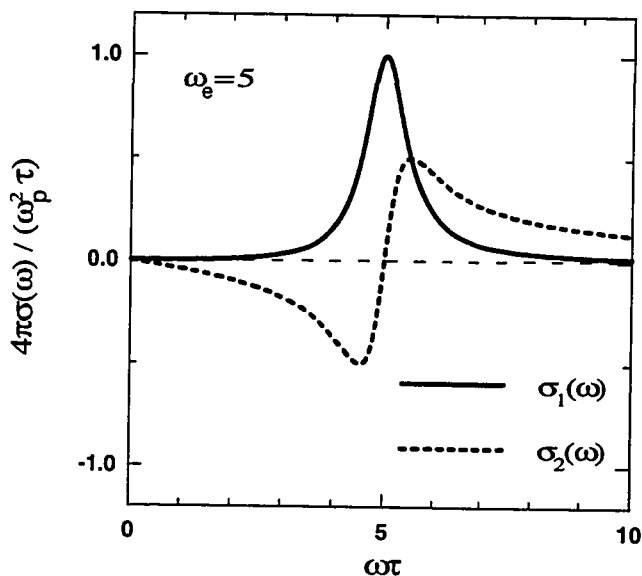


Figure 1.2: The frequency dependence of the real and imaginary parts of optical conductivity given by the oscillator model.

1.1.6 The method of infrared reflectance spectroscopy

Knowing the dielectric function (or the optical conductivity) of a material gives one a wealth of an information about free carriers, interband transitions, phonon spectra, elastic and inelastic scattering processes, etc. There are many experimental methods [Palik85] aimed at obtaining the dielectric function, each having its own advantages in a certain frequency range. For example, microwave spectroscopy is very useful in the frequency range $\Delta\omega = 10 - 30 \text{ GHz} = 0.04 - 0.12 \text{ meV}$ while optical ellipsometry gives

the optical constants with high accuracy in the range $\Delta\omega = 16000 - 48000 \text{ cm}^{-1} = 2 - 6 \text{ eV}$. However, in the frequency range $\Delta\omega = 100 - 20000 \text{ cm}^{-1} \simeq 0.01 - 2.5 \text{ eV}$, which is the most important frequency region if one is interested in the intraband or low-order interband electronic transitions (such as excitations of conducting electrons or transitions across a semiconducting gap), the method of infrared reflectance spectroscopy is so far the most powerful.

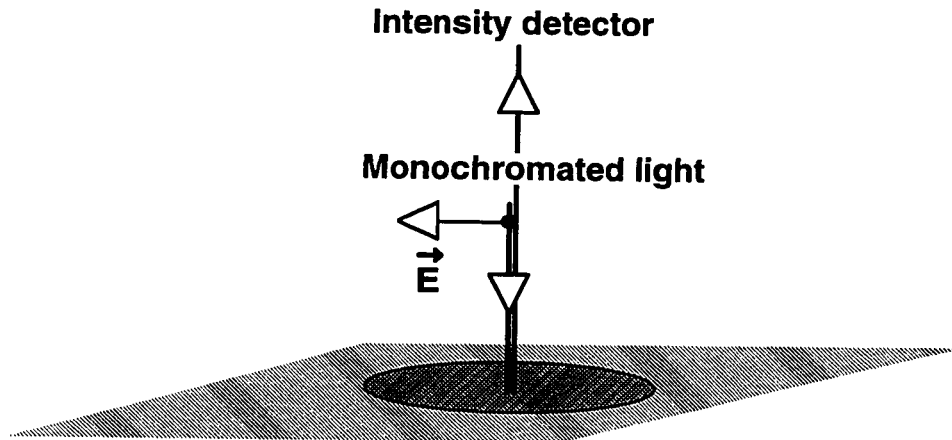


Figure 1.3: Sketch of the experimental geometry used in the reflectance spectroscopy

A sketch of the experimental geometry, used in infrared reflectance spectroscopy, is shown in Fig. 1.3. Incident monochromated light of frequency ω is directed normal to the surface of a material. The measured quantity is the intensity of the reflected light, $I_{ref}(\omega)$. If the intensity of incident radiation, $I_{inc}(\omega)$, is known then the ratio of these two can be obtained. The ratio is called the reflectance, $R(\omega) = I_{ref}(\omega)/I_{inc}(\omega)$. By changing the frequency of the incident radiation continuously a spectrum of $R(\omega)$ can be obtained. Obviously, $R(\omega) \leq 1$.

Since the ultimate goal of the experiment is to obtain both the real and imaginary parts of $\epsilon(\omega)$, that is two functions, one needs an additional quantity in addition to the measured $R(\omega)$. To obtain this additional information, Kramers-Kronig relations can be used again. The complex reflectance coefficient can be written as:

$$r(\omega) = |R(\omega)|^{1/2} \exp(i\theta(\omega)). \quad (1.48)$$

Here, $R(\omega)$ is the amplitude of the reflectance coefficient, that can be measured

directly, and $\theta(\omega)$ is the phase shift. The phase shift is related to the amplitude by the KK integral:

$$\theta(\omega) = \frac{\omega}{\pi} \int_0^{\infty} \frac{\ln R(\Omega)}{\omega^2 - \Omega^2} d\Omega. \quad (1.49)$$

The range of the KK integral extends over all frequencies, requiring extension of experimental results beyond the measured frequency interval. For the extension one can use results of other experiments, such as microwave at low frequencies or ellipsometry at high frequencies, or an extrapolation. For the extrapolations, power laws are typically used at high frequencies, $R \sim \omega^{-p}$ with $0 \leq p \leq 4$. At low frequencies the reflectance is assumed to be constant if the sample is an insulator and to follow the Hagen-Rubens relation, $R = 1 - (2\omega\rho_{dc}/\pi)^{1/2}$, where ρ_{dc} is a dc resistivity, if it is a metal. More thorough discussions of the low- and high-frequency approximations can be found elsewhere [Timusk89, Bosovic90].

As soon as both $r(\omega)$ and $\theta(\omega)$ are known, the complex index of refraction can be calculated from the relation:

$$r(\omega) = \frac{n(\omega) - 1 + ik(\omega)}{n(\omega) + 1 + ik(\omega)}, \quad (1.50)$$

and other optical constants follow from Eq.'s 1.23,1.31.

Of course, the real experiments are much more complicated than the sketchy outline presented above. For example, a Fourier-transform technique is normally used in the infrared frequency range, 100-8000 cm^{-1} , instead of the frequency-scanning approach. To obtain the experimental results presented in this thesis, the infrared frequency range reflectivity measurements were carried out using a rapid scan interferometer with the optics focused on a sample mounted in a continuous flow cryostat. For near-infrared and visible, a grating spectrometer with appropriate detector-filter combinations with overlapping frequency ranges was used. To obtain the absolute value of the reflectance, geometrical scattering losses were accounted for by *in situ* evaporation of a metallic film (Au or Al) onto the surface of the sample. The coated sample was then remeasured and the absolute value of R is then given by the ratio of spectra before and after plating, corrected for the absolute reflectance of the metallic film. [Palik85] The experimental details, as well as the interferometer design, are

described in great detail in the original work by Homes [Homes93a] and will not be presented in this thesis.

1.2 The superconductivity phenomenon: an optical perspective

1.2.1 Conventional superconductivity

The superconductivity phenomenon was discovered in mercury by Kamerlingh-Onnes in 1911, shortly after he had built the first helium liquefying machine. The phenomenon was largely unexplained until 1957 when the BCS theory [Bardeen57] (named after Bardeen, Cooper, and Schrieffer) was advanced and has subsequently proven to be one of the most successful theories in modern solid state physics. Even before the development of the BCS model there was an understanding that to become superconducting, charge carriers must be bound into bosonic pairs that would condense into a superfluid much like ordinary bosons. The problem was to find a force that would bind electrons into bosonic pairs despite their Coulomb repulsion. The discovery of the isotope effect, that is the fact that the transition temperature is inversely proportional to the square root of the mass of the ions constituting a superconductor, provided an important and much needed boost to the theoretical work in this field. The resulting BCS model identified the pairing interaction as an electron-phonon interaction.⁵ In the BCS theory the pairing occurs between electrons with opposite momenta and opposite spins. The resulting pair is called a Cooper pair. The boson condensation temperature for the density of Cooper pairs achieved in conventional metals is of order of a Fermi temperature, which is much larger than T_c in conventional superconductors. Therefore, as soon as the bosonic Cooper pairs are formed, they condense into a superfluid.

The famous formula for the superconducting transition temperature in the BCS model is:

$$k_B T_c = 1.13 \hbar \omega_D \exp\left(-\frac{1}{N(0)g}\right) \quad (1.51)$$

⁵One must distinguish, however, between the BCS model and the BCS theory. The theory is valid for any boson-exchange pairing while the model works specifically with phonons.

Here, $\hbar\omega_D$ is the Debye energy.⁶ Unfortunately, the exponential factor that includes a product of the density of states at the Fermi level, $N(0)$, and the strength of electron-phonon interaction, g , is usually very small, thus making conventional superconductivity a very low-temperature phenomenon. For example, while the Debye temperature in aluminum is almost 400 K, the T_c is only 1 K. The Fermi temperature for aluminum is 136,000 K, which is much larger than either T_c or the Debye temperature.

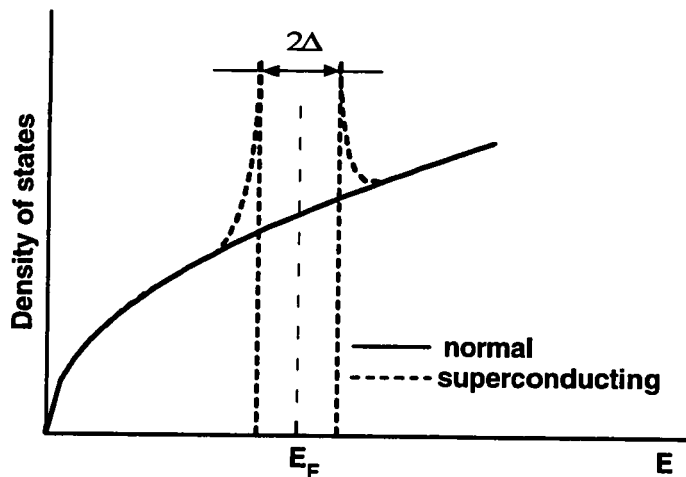


Figure 1.4: A sketch of the renormalization of a one-particle density of states upon entering the superconducting state in the BCS theory. Note a gap opening at the Fermi surface and (square root) singularities on both sides of the superconducting gap.

As a result of a superconducting transition, the electronic density of states is renormalized and the fully-developed superconducting state has a gap, 2Δ , where Δ is called the superconducting gap. This is schematically shown in Fig. 1.4. The gap results from the fact that in order to create a one-particle excitation (that is an unpaired electron) in the BCS ground state one needs to supply an energy Δ . Since there are two electrons in each of the Cooper pairs, the energy to create a lowest-energy excitation in a BCS ground state, at the same time conserving the number of

⁶In a more broad interpretation of this formula, $\hbar\omega_D$ is a characteristic frequency of bosons which mediate the electron-electron pairing. In this case g is a strength of the electron-*boson* pairing.

electrons in a system, is 2Δ – one Δ for an excited electron and another Δ for a hole that is left behind. Above the gap frequency the electronic density of states has a singularity. It is a fundamental result of BCS theory that the gap value is related to T_c in the following manner:

$$\frac{2\Delta}{k_B T_c} = 3.52. \quad (1.52)$$

There are many other exciting properties of superconductors that are, however, too numerous to be listed in this brief overview. An interested reader can find much more information elsewhere. [Kittel86, Ashcroft76, Tinkham80, Carbotte90] In the rest of this section we will concentrate on the optical properties of superconductors.

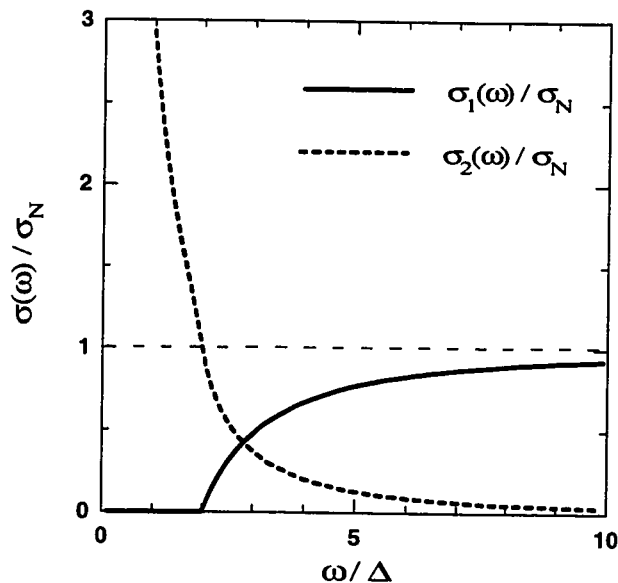


Figure 1.5: Real and imaginary parts of the optical conductivity of a superconductor, calculated from the Mattis-Bardeen theory.

Opening of a gap in the electronic density of states upon entering the superconducting state greatly affects the optical response functions of a material. Since in optical experiments no electrons are taken out of a system, the minimum energy required to create an excitation is 2Δ . Therefore, at photon energies below twice the gap energy, 2Δ , a material in the superconducting state becomes a perfect re-

flector, with $R = 1$. The real and imaginary parts of optical conductivity within weak-coupling BCS theory were calculated by Mattis and Bardeen. [Mattis58] The calculation is valid either in the extreme clean limit, defined as $2\Delta \gg 1/\tau$, or the extreme dirty limit, $2\Delta \ll 1/\tau$. Fig. 1.5 shows the Mattis-Bardeen theory results for the real and imaginary parts of optical conductivity as a function of frequency at $T = 0$. The theoretical results are in complete agreement with the experimental work. [Glover56, Glover57]

The characteristic feature of the real part of optical conductivity (that describes energy losses) of a superconductor is the formation of a low-energy gap, with $\sigma_1(\omega) = 0$ at all non-zero energies $\omega \leq 2\Delta$.⁷ One must realize, however, that the f sum rule is still in effect and the integrated value of $\sigma_1(\omega)$, or its spectral weight, remains unchanged. The spectral weight that seems to be missing is in fact contained in a δ -peak at zero frequency that is responsible for the infinite dc conductivity. The weight of the δ -peak is determined by the number of superconducting carriers, so that $\lim_{\omega \rightarrow 0} \sigma_1(\omega) = \omega_{ps}^2 \delta(\omega)/8$, where ω_{ps} is a plasma frequency of the superconducting carriers. At energies much larger than the gap energy, the real part of the conductivity in the superconducting state rises to join the normal-state conductivity.

The corresponding changes in the imaginary part of the optical conductivity can be understood by assuming the scattering rate in formula 1.31 to be zero for the superconducting carriers. One obtains $\lim_{\omega \rightarrow 0} \sigma_2(\omega) = \omega_{ps}^2/(4\pi\omega)$, that is $\sigma_2(\omega)$ in a superconducting state is dominated at low frequencies by an inductive $1/\omega$ term, as seen in Fig 1.5.

It is important to note that Fig. 1.5 is somewhat misleading because it shows not the conductivity but the ratio of conductivity to its normal-state value. One must distinguish between the clean and dirty limits of a superconductor. In the clean limit the inequality $2\Delta \gg 1/\tau$ is true and, therefore, all (or most of) the conducting carriers condense into a superfluid. In this case $\omega_{ps} \simeq \omega_p$ and, since most of the conductivity spectral weight condenses to the $\delta(\omega)$ peak, the gap feature is very weak or not observable. In the dirty limit, $2\Delta \ll 1/\tau$, only a fraction of the conduction carriers condenses into a superfluid. In this case $\omega_{ps} \ll \omega_p$ and the gap feature is intense. The superconducting gap in a conventional BCS superconductor can also be suppressed by

⁷We put $\hbar = 1$.

introducing magnetic impurities (so called gap-less superconductivity). Therefore, the manifestation of a superconducting gap is not the only effect the superconductivity phenomenon has on the optical properties. The main feature is the disappearance of $\sigma_1(\omega)$ spectral weight (and associated $1/\omega$ singularity in $\sigma_2(\omega)$) that is a direct result of the formation of a superfluid condensate.

We note that by analogy with derivation of Eq. 1.45 for the penetration depth of electromagnetic radiation into a metal, one can obtain the low-frequency penetration depth in a superconductor. This is called the London penetration depth and it is given by:

$$\lambda_L = c/\omega_{ps}. \quad (1.53)$$

Therefore, the penetration depth can be obtained from the optical results in two ways. One way involves integration of $\sigma_1(\omega)$ over frequencies much larger than the superconducting gap and determining the "missing" spectral weight. Another way involves analysis of the frequency dependence of $\sigma_2(\omega)$ at the frequencies much lower than 2Δ .

1.2.2 High-temperature superconductivity

This year is the 10th year since publication of the original paper by Bednorz and Müller, [Bednorz86] marking the discovery of high-temperature superconductivity, or HTSC, in multiphase La-Ba-Cu-O material.

Let us first ask ourselves, what value of T_c should be considered "high"? There is no intrinsic limit on T_c even in the BCS model, provided that the pairing interaction and/or density of states on a Fermi surface can be infinitely enhanced. Therefore, one way to determine if a material is a high- T_c superconductor is to compare the T_c value to the density of states at the Fermi level, $N(0)$. Two graphs that make this comparison are shown in Fig. 1.6. The first one is adopted from the work by Batlogg *et al.* [Batlogg89] and shows two experimental quantities plotted against each other: the T_c value and the Sommerfeld constant $\gamma \sim N(0)$, determined from specific heat measurements. The HTSC materials are easily identified in the plot, all of them have a much larger T_c than the conventional superconductors with the same $N(0)$.

The second plot, adopted from the work by Uemura *et al.*, [Uemura91] is similar but instead of the Sommerfeld constant, a Fermi temperature, defined as

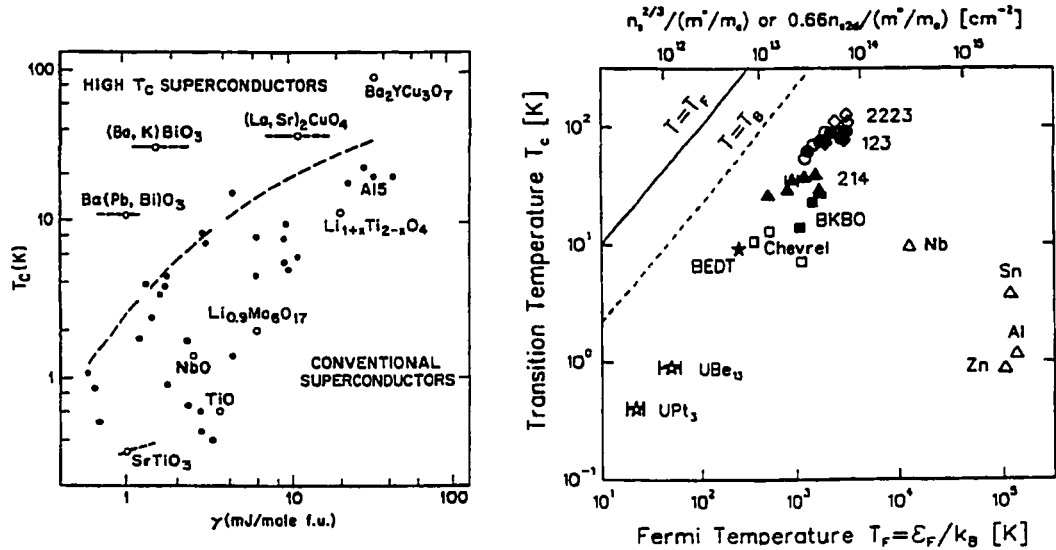


Figure 1.6: A comparison of T_c with the free-carrier density in a superconductor. The graph on the left is reproduced from an article by Batlogg *et al.* [Batlogg88] and shows T_c against the Sommerfeld constant γ , proportional to the density of states at the Fermi level, for different superconductors. The graph on the right is reproduced from an article by Uemura *et al.* [Uemura91] and shows T_c against Fermi temperature, T_F , determined from the density of superconducting carriers n_s , plotted on the top axis. Note that the formula connecting E_F and n_s is different for the 2D (the cuprates) and the 3D cases.

E_F/k_B , is plotted. Since the density of states at the Fermi surface is proportional to a power of E_F , the second graph represents the same idea as the first one: having fairly small electronic density of states the high-temperature superconductors show (relatively) very high T_c values. This may be thought of as a definition of high-temperature superconductivity.

The high-temperature superconductors not only show high T_c values, their normal-state properties are equally unusual. In fact, it is believed that these normal-state properties contain the key to the solution of the HTSC puzzle. Below we will summarize some of the essential properties of HTSC materials with, again, special emphasis on the infrared optical properties.

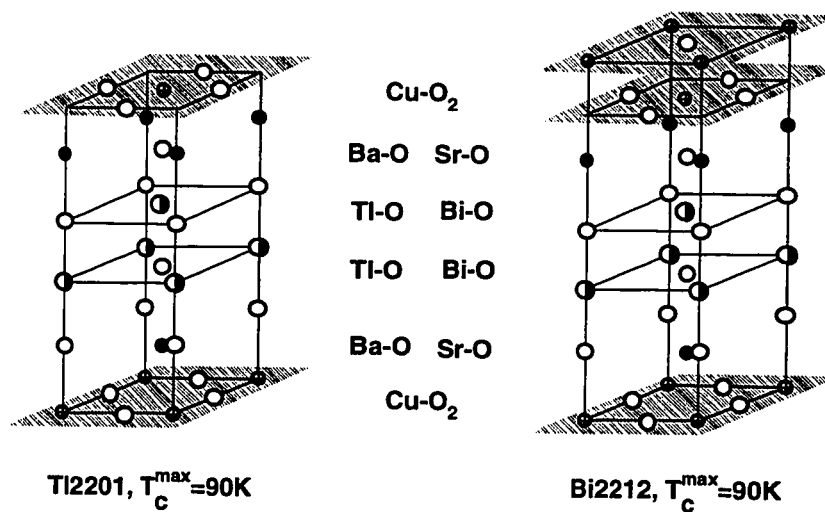


Figure 1.7: Crystal structure of Tl2201 and Bi2212.

To start with, most of the HTSC materials (with the marked exception of $\text{Ba}_{1-x}\text{K}_x\text{BiO}_3$ (BKBO) and $\text{Ba}_{1-x}\text{Pb}_x\text{BiO}_3$ (BPBO)) have a layered perovskite structure and contain Cu (therefore they are called the cuprates). The structures of two materials, $\text{Tl}_2\text{Ba}_2\text{CuO}_{6+\delta}$ (Tl2201) and $\text{Bi}_2\text{Sr}_2\text{CaCu}_2\text{O}_{8+\delta}$ (Bi2212), are shown in Fig. 1.7. These two materials have been studied intensively in the experimental work presented in this thesis. The main structural unit, common to all cuprate superconductors, is a 2-dimensional CuO_2 plane. It is in fact believed that the super-

conductivity occurs in the CuO_2 planes with the rest of the structure being merely a "charge reservoir", supplying charge carriers to the planes. In Tl2201 material the charge reservoirs are the double TlO planes while in Bi2212 they are the double BiO planes. The CuO_2 planes may enter the crystal structure in different combinations, for example Tl2201 is a single-layer material while Bi2212 is a double-layer material since two CuO_2 planes occur close together. Other HTSC materials can have a 3-layer, 4-layer and even a so-called infinite-layer structure. [Egami94, Hazen90] It is common to refer to the CuO_2 planes as the *ab*-planes while the interplane direction is usually referred to as the *c*-axis. More information on structure of HTSC materials can be found in the review articles [Egami94, Hazen90]. Since the structure of the HTSC materials is very anisotropic, the transport properties are anisotropic as well, with ratios between the interplane and in-plane dc resistivity, ρ_c/ρ_{ab} , reaching 1000-10000 in Bi2212. In this thesis, only results obtained in the *ab*-plane configuration (that is the material surface shown in Fig. 1.3 can be thought of as a CuO_2 plane) are presented.

The superconducting transition temperature of HTSC materials can be changed by doping. In most of the cuprate superconductors (with the exception of $(\text{NdCe})_2\text{CuO}_4$) the charge carriers are holes and the doping is p-type. It can be achieved by either adding O^{-2} ions to a material or by substituting positive ions by ions of smaller valence, such as La^{+3} by Ba^{+2} in $\text{La}_{2-x}\text{Ba}_x\text{CuO}_4$ (La214). In both Tl2201 and Bi2212 systems the doping is realized by adding or removing additional oxygen atoms. The extra oxygens are interstitial in these materials, that is they are located in between the double TlO or BiO planes.

The dependence of the superconducting transition temperature T_c on the doping level is not monotonic and is schematically shown in Fig. 1.8 by the solid line. It is customary to divide the metallic region of the phase diagram of HTSC materials into 3 different regimes: (1) the "underdoped" regime, where the superconducting phase is adjacent to the insulating phase and T_c increases with increasing (p-type) doping; (2) the "optimum" T_c regime, where T_c reaches the highest value within a given series; (3) the "overdoped" regime where T_c decreases with further doping while the material becomes a better metal. Below the underdoped regime lies the insulating regime where the cuprate materials are antiferromagnetic (AFM) insulators. There

is also ample evidence that a local AFM ordering may extend well into the metallic region of the phase diagram, although the exact boundary where these fluctuations into local AFM ordering disappear is not clear at the moment. The materials chosen for this study *together* cover the whole metallic doping range since Bi2212 can be underdoped and slightly overdoped, while Tl2201 can not be underdoped but can be strongly overdoped.

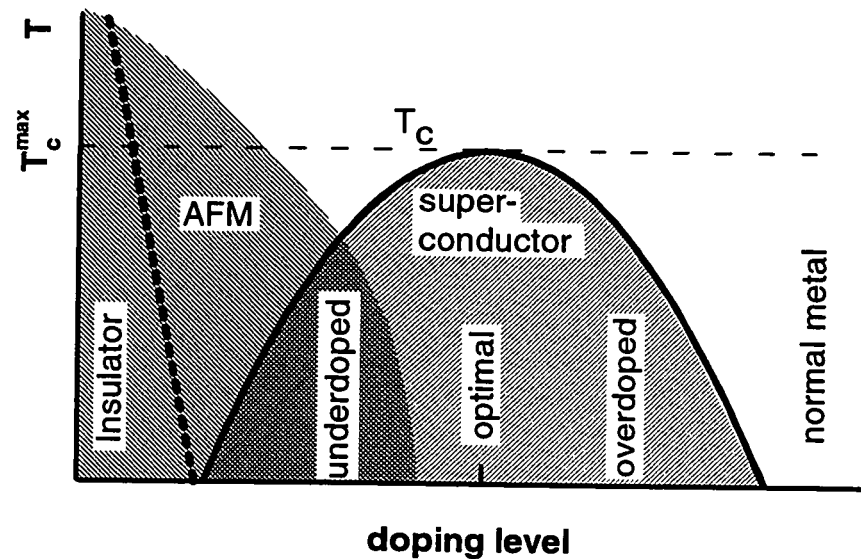


Figure 1.8: T_c vs. doping level in high-temperature superconductors.

One of the most interesting normal-state properties of the high-temperature superconductors is the linear in T behavior of the ab -plane dc resistivity, $\rho_{ab}(T)$, in the optimally doped materials [Gurvitch87, Ito93]. For example, in $\text{La}_{2-x}\text{Sr}_x\text{CuO}_4$ material with $x = 0.15$ the resistivity is linear from $T = T_c = 40$ K to over 800 K. [Takagi92] Although the electron-phonon interaction can in principle produce a high-temperature T -linear $\rho(T)$, the dependence observed in the cuprates cannot be reproduced in the electron-phonon scenario since: (i) The temperature range of the linear dependence is very large; (ii) The intercept of the high-temperature linear law with the vertical axis is almost zero, while it is expected to be negative for the electron-phonon interaction.

Without elaboration, that can be found in the original papers, other unusual normal-state properties of HTSC include: peculiar temperature dependence

of the uniform spin susceptibility [Warren89, Yoshinari90], intense electronic background in the Raman scattering intensity spectra [Sugai89], the peculiar temperature and doping dependence of the Hall effect [Stromer88, Ong87] and the thermoelectric power, [Obertelli92] the linear V-shape background in normal-state tunneling data, [Sharifi91] *etc.*

The optical properties of the high-temperature superconductors are truly unconventional. The normal-state spectrum of the real part of the optical conductivity is shown in Fig. 1.9 for an example Bi2212 material. While the spectrum is in general metallic, since $\sigma_1(\omega)$ increases monotonically as frequency approaches zero, the shape of $\sigma_1(\omega)$ is non-Drude like. For example, the dashed line in Fig. 1.9 shows a Drude curve, calculated using Eq. 1.41 with parameters chosen to fit the low-frequency part of $\sigma_1(\omega)$. One can see that the frequency dependence of the experimental $\sigma_1(\omega)$ is much slower than the $1/\omega^2$ law predicted by the Drude theory. As a result, the optical conductivity has too much spectral weight at high frequencies and can not be described using Eq. 1.41, as derived for normal metals. The excess conductivity at high frequencies in HTSC materials is called a mid-infrared, or "MIR", absorption.

In the superconducting state the HTSC materials do not reveal the clean superconducting gap that is predicted by the BCS theory and was observed in conventional superconductors. [Glover56, Glover57] While results of all of the experimental techniques show a significantly depressed one-particle density of states in the superconducting regime, the low-energy system response always remains finite. An example is the optical conductivity, the real part of which in the superconducting state is plotted in Fig. 1.9 by the thinner line. One can see that while the total spectral weight of $\sigma_1(\omega)$ is significantly suppressed as temperature is reduced below T_c , which is an unmistakable signature of the formation of a superconducting condensate, the conductivity remains finite at all frequencies even at $T = 10 \text{ K} \simeq 0.1T_c$. Furthermore, one of the most fascinating recent experimental results is that the superconducting pairing, with the corresponding reconstruction of the optical conductivity spectra, may be actually occurring at temperatures well above the bulk superconducting temperature T_c !

While most of high- T_c superconductors are cuprates, two materials, BKBO and BPBO, are exceptions. While both have T_c values remarkably large compared to the

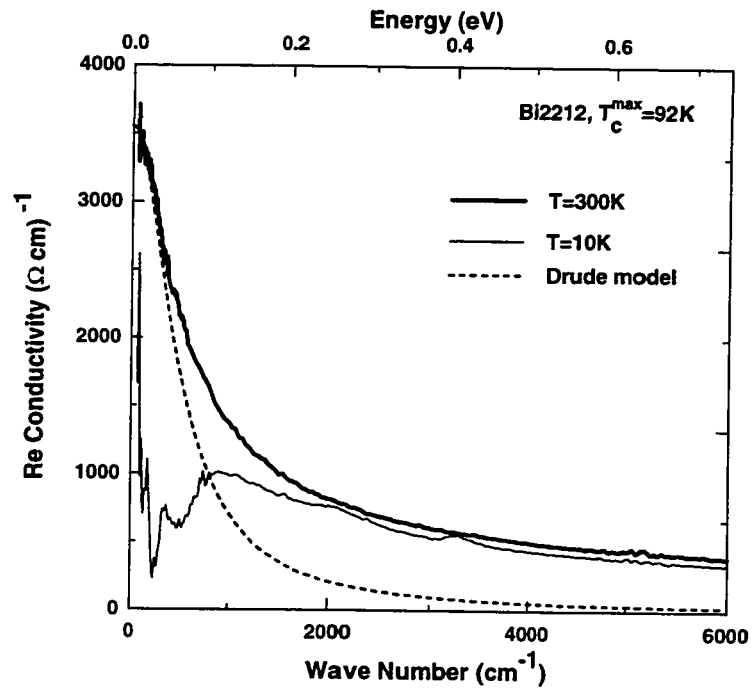


Figure 1.9: The typical spectrum of the real part of the optical conductivity of a HTSC material in the normal and the superconducting states.

density of states at the Fermi level (see Fig. 1.6), they do not contain copper and have an isotropic structure. The normal-state and the superconducting-state properties of BKBO and BPBO are in many ways similar to those of the cuprate superconductors. In particular, the optical conductivity in the metallic doping regime is non-Drude like and, although the superconducting gap onset 2Δ is easily identified at temperatures $T < T_c$, $\sigma_1(\omega)$ at frequencies below 2Δ remains finite.

A wealth of theoretical models have been advanced in an attempt to explain both the normal and the superconducting properties of the HTSC materials. The models range from the most exotic ones, such as: the resonating valence bond (RVB) model, [Anderson73, Anderson87] the $t - J$ model, [Kotliar88, Wen96] the anion superconductivity model, [Chen89, Laughlin88] the quantum phase fluctuations model, [Emery95a, Emery95b] the interplane pair tunneling model, [Chakravarty93], the polaron superconductivity models [Micnas90, Mott90]; to more conventional ones, such as: the marginal Fermi-liquid (MFL) model, [Schmitt-Rink88] nearly antiferromagnetic Fermi liquid (NAFL) model, [Montoux92, Pines94] and the model involving an enhancement of the electronic density of states due to an extended van Hove singularity. [Abrikosov93, Abrikosov94]

In the following sections of this thesis we will discuss the experimental optical results for the HTSC materials in both the normal and the superconducting states as well as their relation to the other experimental data and some of the existing theories.

Chapter 2

Doping dependence of the free-carrier density in high- T_c superconductors: Optical results

2.1 Introduction

One of the most striking features of the high- T_c phenomenon is the peculiar dependence of the superconducting transition temperature T_c on the doping level, shown in Fig. 1.8.

While the underdoped and optimally doped regimes have been studied extensively, the overdoped regime has not enjoyed this kind of attention. It is generally believed that the decrease of T_c with overdoping is associated with an increasing concentration of mobile carriers (holes). For example, a "universal" dependence $T_c(p)$, where p is a number of holes per planar Cu, was suggested where T_c reduces parabolically with p for $p > 0.16$ (overdoped regime). [Presland91, Tallon95] If true, this behavior is most unusual and surprising, since in the conventional superconductors an increased carrier density normally leads to an *increased* T_c , according to the relation 1.51.

Information about the mobile carrier density can be obtained from the spectral weight (SW) contained in the low-frequency real part of optical conductivity $\sigma_1(\omega)$. In an analogy with the f sum rule (section 1.1.3), a finite energy sum rule can be formulated. [Smith85, Timusk89] According to the finite-energy sum rule an effective

density of carriers contributing to optical transitions below a certain cut-off energy $\hbar\omega_0$, $n_{eff}(\omega_0)$, is given by a SW of $\sigma_1(\omega)$, integrated over energies from zero to $\hbar\omega_0$:

$$n_{eff}(\omega_0) = \frac{m_e}{8\pi e^2} \int_0^{\omega_0} \sigma_1(\omega) d\omega, \quad (2.1)$$

where m_e is a bare electron mass.

In the rest of this chapter we will use the finite-energy sum rule analysis of the optical conductivity of HTSC to determine whether or not the conventional view on overdoped HTSC, with the density of mobile carriers monotonically increasing with doping level, is consistent with the experimental results on the optical conductivity.

2.2 Experimental details

In order to cover a broad range of doping regimes we performed reflectivity measurements upon two families of high- T_c cuprates: Bi2212 and Tl2201. This was necessary because, with the exception of La214, none of the existing cuprates allows one to explore a full spectrum of doping regimes. For instance, Bi2212 material can be conveniently underdoped and slightly overdoped by reducing/increasing the amount of oxygen from the optimally doped level. However these crystals are not suitable for strong overdoping. On the contrary, Tl2201 samples could be only overdoped by introducing interstitial O atoms between the TlO planes so that T_c is suppressed from about 90 K in the *stoichiometric* composition down to less than 4 K in the overdoped composition.

We have performed reflectivity measurements on two underdoped ($T_c = 67$ K and $T_c = 82$ K), one optimally doped ($T_c = 90$ K), and one overdoped ($T_c = 82$ K) Bi2212 single crystal. All the Bi2212 crystals were prepared from the as-grown crystals by annealing in argon and/or oxygen. The three T2201 single crystals used in the measurements had T_c 's of 90 K (highest T_c achievable), 60 K, and 23 K (both overdoped). The single crystals used in this work were grown by P. Fournier at Stanford University (Bi2212) and by N.N. Kolesnikov at the Institute of Solid State Physics, Russia (Tl2201). The detailed information of the crystal growth technique is given elsewhere. [Fournier96, Kolesnikov95] The superconducting transition temperatures for all samples were measured in a SQUID magnetometer.

The reflectivity was measured over a broad energy range: from 30 - 50 cm^{-1} up to 20,000 cm^{-1} for Bi2212 samples; from 30 - 50 cm^{-1} up to 50,000 cm^{-1} for Tl2201 samples. The complex optical conductivity $\sigma_1(\omega) + i\sigma_2(\omega)$ of single crystalline samples was obtained from Kramers-Kronig analysis of reflectivity. To perform the required integrations it was necessary to extend the reflectance beyond the actually measured range, as described in chapter 1. Below the lowest frequency measured we have tried different types of reflectivity approximations, from the Hagen-Rubens formula with the parameters taken from the dc resistivity measurements, [Kendziora93, Manako92] to a straight line between unity at zero frequency and the last experimental point. We found that in the frequency region that will be of interest in this work ($\omega > 100 \text{ cm}^{-1}$) the particular choice of the low-frequency approximation is not important. At high frequencies, the reflectivity of Tl2201 was approximated by a constant between 50,000-300,000 cm^{-1} . For Bi2212, the results of ellipsometric measurements [Humliček90] were used between 20,000-50,000 cm^{-1} while above this frequency range a constant reflectivity approximation was used up to 300,000 cm^{-1} . Above 300,000 cm^{-1} for Bi2212 and Tl2201 the reflectivity was allowed to fall as ω^{-4} .

2.3 Experimental results

The spectral weight of the real part of optical conductivity in all of the samples measured was found to be temperature-independent at energies below 1 eV. Since this is the energy range that we will be interested in this work, in this section we will consider only the room temperature results. The low temperature results will be considered in the next chapter.

The real part of the optical conductivity for Bi2212 material at three doping levels is shown in Fig. 2.1 at room temperature. The inset on the lowest panel of Fig. 2.1 shows the difference between $\sigma_1(\omega)$ obtained for the $T_c = 82$ K slightly overdoped sample (upper panel) and the $T_c = 67$ K underdoped sample (lower panel).¹ First, the low-frequency conductivity SW increases with doping in the underdoped regime. Second, the differential conductivity spectrum has a Lorentzian (Drude-like)

¹The room-temperature $\sigma_1(\omega)$ spectra for under- and overdoped $T_c = 82$ K samples are almost identical. Therefore, the differential spectrum for the two underdoped samples will be similar.

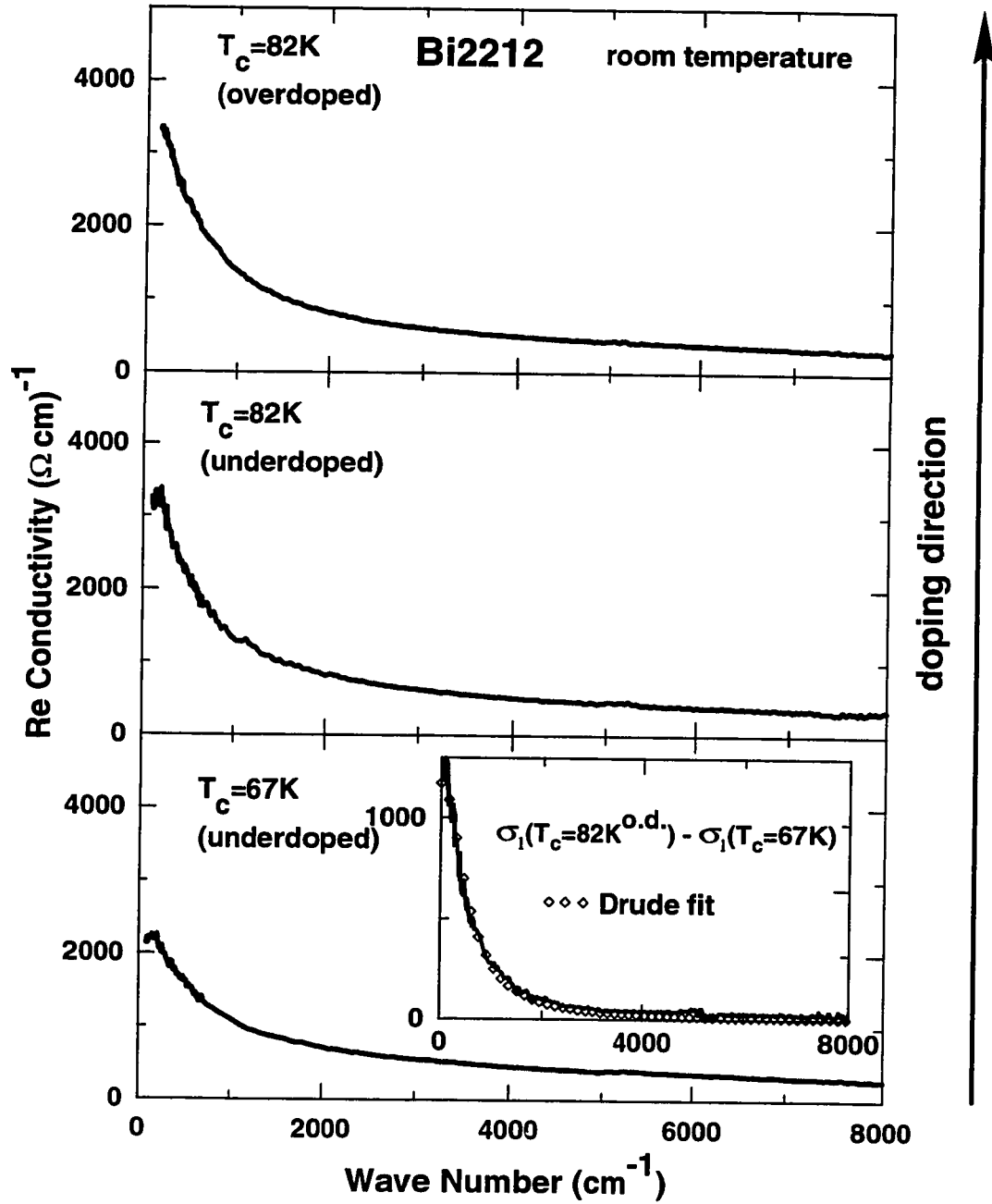


Figure 2.1: The optical conductivity of Bi2212 at several doping levels. The inset: solid line is a difference between $\sigma_1(\omega)$ shown in the upper panel and $\sigma_1(\omega)$ shown in the lower panel. The open symbols represent a fit to a Drude form.

shape characteristic for a free-carrier absorption. [Timusk89, Ashcroft76] The Drude-like shape of the differential conductivity suggests that it is a difference of two spectra that contain free-carrier contributions with similar scattering rates $1/\tau$ but different plasma frequencies (larger for the more heavily doped sample). The increase in the plasma frequency of the Drude part is consistent with the scenario where doping in the underdoped regime produces additional mobile carriers. [Orenstein90, Rotter91] One can also see from the inset of Fig. 2.1 that the increase of the low-frequency SW with doping in the underdoped regime is confined to the energy range below 1 eV.² We note that the doping-induced conductivity increase was found to be confined to below 1 eV in metallic $\text{YBa}_2\text{Cu}_3\text{O}_{7-\delta}$ as well. [Orenstein90, Rotter91]

The $\sigma_1(\omega)$ in the overdoped regime is shown in Fig. 2.2 for Tl2201 system at three doping levels, from the one with the highest T_c achievable (90 K) to the strongly overdoped one with $T_c = 23$ K. The inset in the lowest panel shows the difference between $\sigma_1(\omega)$ for the $T_c = 23$ K and $T_c = 90$ K samples. The resulting differential spectrum is qualitatively different from the one obtained for Bi2212: now there is no doping-induced increase in the conductivity SW. Instead, the SW is *redistributed* with part of it moved from the mid-infrared frequencies to the lower frequencies with (over)doping. This behavior is reminiscent of what was observed by Tamasaku *et al.* in La214 system: [Tamasaku94] although the transfer of conductivity SW from above the charge-transfer gap is nearly saturated as doping is increased above optimal, the SW is biased towards the lower-energy region with overdoping. Again, the redistribution of the SW occurs in the energy range below 1 eV. The differential spectrum can no longer be fitted to a difference of two spectra containing Drude absorption peaks with a same scattering rates but different plasma frequencies. However, now it has a shape of a difference of two Drude peaks with the same plasma frequency but different scattering rates, as is shown in the inset. The parameters used in the fit were $\omega_p = 13,000 \text{ cm}^{-1}$, $1/\tau(T_c = 23\text{K}) = 560 \text{ cm}^{-1}$, $1/\tau(T_c = 90\text{K}) = 660 \text{ cm}^{-1}$, values that are not at all unreasonable. For illustration, a Drude peak with $\omega_p = 13,000 \text{ cm}^{-1}$ and $1/\tau = 560 \text{ cm}^{-1}$ is shown in the bottom panel of Fig. 2.2.

To make the analysis more quantitative in Fig. 2.3 we have plotted the SW of the low-frequency ($\hbar\omega_0 = 1 \text{ eV}$) optical conductivity as a function of T_c . The $\hbar\omega_0 =$

²The parameters used in the fit where $\Delta\omega_p = 6200 \text{ cm}^{-1}$ and $1/\tau = 550 \text{ cm}^{-1} \ll 1 \text{ eV}$.

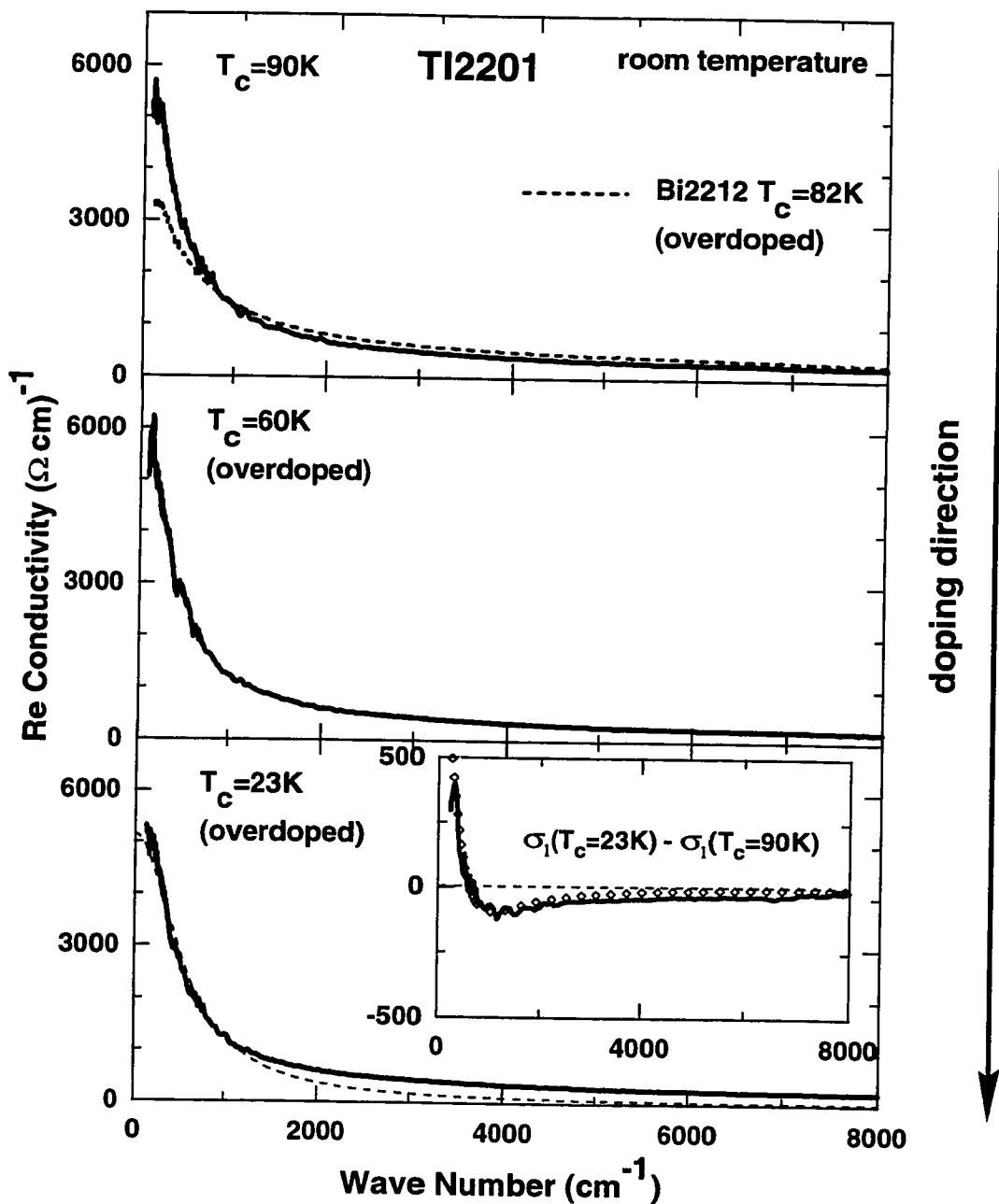


Figure 2.2: The optical conductivity of Tl2201 at several doping levels. On the upper panel $\sigma_1(\omega)$ for slightly overdoped Bi2212 is shown for comparison. On the lower panel a Drude curve with $\omega_p = 13,000 \text{ cm}^{-1}$ and $1/\tau = 560 \text{ cm}^{-1}$ is shown for illustration as described in text. The inset: solid line is a difference between $\sigma_1(\omega)$ for the $T_c=23 \text{ K}$ and $T_c=90 \text{ K}$ samples. The open symbols show a fit to a difference of two Drude curves with a same ω_p but different $1/\tau$ as described in text.

1 eV was chosen to isolate the energy region where the conductivity actually changes with doping in the doping range considered in this work. For reasons described below we will mainly be interested in relative *changes* in the SW as a function of doping as opposed to its absolute values. Therefore, we have normalized our results to those obtained for the optimal doping concentrations within each series. On the horizontal axis we plot T_c in the functional form $\pm(1 - T_c/T_c^{max})$, with minus sign for the underdoped materials and plus sign for the overdoped ones. Previously published results [Tamasaku94, Cooper93] for several other cuprate materials are plotted as well.³ We also include data obtained on 3D HTSC material BKBO [Puchkov96a] at doping levels with $T_c = 31\text{ K}, 28\text{ K}, 21\text{ K}$.⁴ All of the data points fall on the same curve which is highly asymmetrical with respect to the point of optimal doping (0,1). While in the underdoped regime increase in T_c is accompanied by an increase in the low-frequency conductivity SW, this behavior changes abruptly at the optimal doping: in the overdoped regime increase in the low-frequency SW is not observed. In fact, if it changes at all, it decreases with decreasing T_c .

2.4 Discussion

The results presented above suggest that the optimal doping level is not only the one with the highest T_c in a given series, but it also separates two distinctly different regimes of optical conductivity behavior as a function of doping. While in the underdoped regime the total low-frequency conductivity spectral weight increases with doping, which can be attributed to the increasing density of the mobile charge carriers, in the overdoped regime the total spectral weight below 1 eV does not increase and the changes in $\sigma_1(\omega)$ are more likely to be due to the changing scattering rate of the mobile carriers.

Before we use the finite-energy sum rule analysis to make a connection between the doping dependence of the conductivity SW and the mobile carrier density, we show how despite some of its shortcomings the essential information can be extracted. The

³While plotting the results by Tamasaku *et al.* [Tamasaku94] we have used the parabolic $T_c(x)$ relation, obtained for $\text{La}_{2-x}\text{Sr}_x\text{CuO}_4$ (Ref. [Presland91]), to calculate T_c 's from x .

⁴We plot BKBO data in the overdoped part of Fig. 2.3 as it becomes a better metal as T_c decreases. The integration has been done up to $\hbar\omega = 2\text{ eV}$.

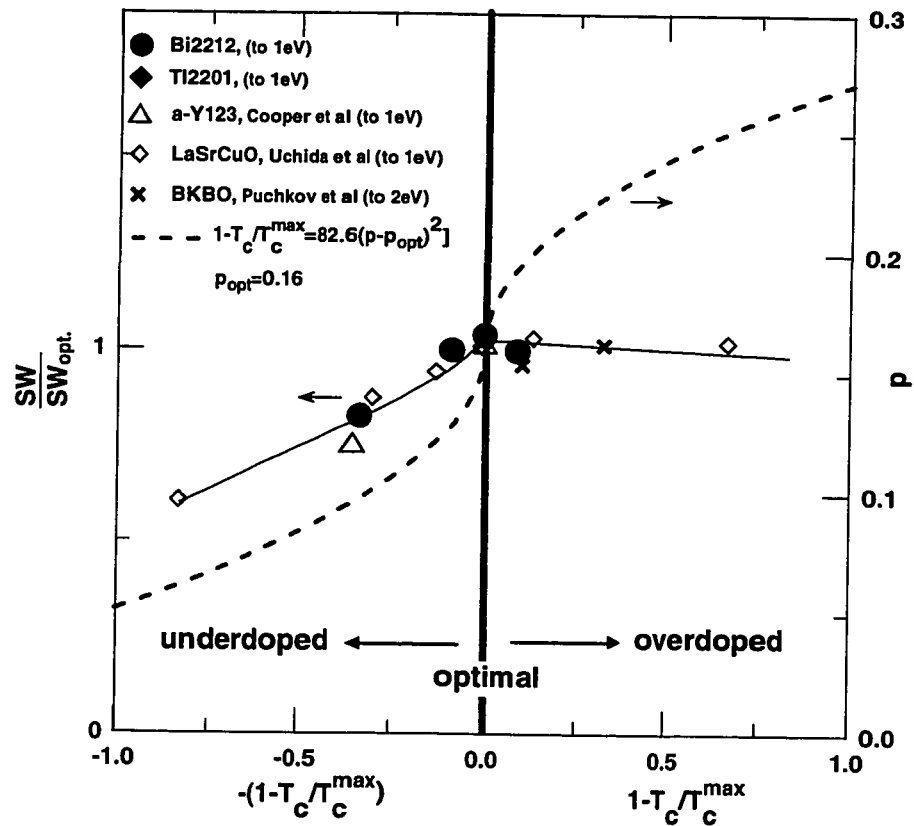


Figure 2.3: The relative changes in the low-frequency conductivity spectral weight for several HTSC material series as a function of T_c . The left-hand part corresponds to underdoped regime, the right-hand part corresponds to overdoped regime. The dashed line shows a low-frequency spectral weight expected on the basis of parabolic dependence $T_c(p)$ proposed for the HTSC cuprates.

HTSC materials demonstrate a complicated non-Drude shape of $\sigma_1(\omega)$ where the free-carrier absorption is not obviously defined. [Timusk89] This makes a choice of $\hbar\omega_0$ ambiguous. There are two approaches to describe the optical conductivity of the HTSC cuprates. The first one is a two-component approach in which the total conductivity is divided into a free-carrier Drude and bound-carrier mid-infrared (MIR) parts, independent of each other. The alternative approach is a one-component one, in which both parts are due to excitations of the same "kind" of charge carriers that have frequency-dependent effective mass and scattering rate. This may result in an intensive conductivity sideband at the MIR frequencies as in the case of metals with strong electron-phonon interaction. [Allen71, Shulga91] The SW of the MIR sideband is taken from the Drude absorption so that their *total* SW represents the actual free-carrier density.

It is outside the scope of this discussion to decide which description is the correct one but we can outline the consequences that each of them may have on the analysis of Eq. 2.1. (i) The two-component model: An integration of Eq. 2.1 will give an overestimated absolute value of the mobile carrier density as it will include the "parasitic" MIR absorption. However, as the SW of the MIR conductivity does not change very much with doping (see the insets of Figs. 2.1, 2.2), we can still conduct a *comparative* analysis of *changes* in the free carrier density with doping within a given series. (ii) The one-component model: An integration in the range from 0 to 1 eV, which essentially includes both the free-carrier part and the MIR sideband, may in fact give us the absolute value of the free carrier density close to the correct one. However, the MIR absorption may still include, for example, an interband transition. In this case while the absolute values of carrier density obtained using Eq. 2.1 may be misleading, the comparative analysis still can be conducted.

In the light of the above discussion we believe that the doping-induced *changes* in the low-frequency SW reflect changes in the mobile carrier density. This puts the results presented in Fig. 2.3 in contradiction with the scenario where the decrease of T_c in the overdoped regime is a consequence, or associated with, the increasing mobile carrier density. For comparison, in Fig. 2.3 we have plotted the SW expected from the relation $1 - T_c/T_c^{max} = 82.6(0.16 - p)^2$, proposed as a universal relation for HTSC cuprates. [Tallon95] While in the underdoped regime this relation is in qualitative

agreement with the experiment (the density of the mobile carriers increases with doping), there is a qualitative difference in the overdoped regime: the experimental free-carrier density is *not* increasing with overdoping.⁵

The optical conductivities of Bi2212 double-plane and Tl2201 single-plane are very similar, the only difference being the bias of the SW towards lower frequencies in TL2201 (see the upper panel of Fig. 2.2). This suggests that the 3D densities of mobile charge carriers are similar in both materials. Taking into account corrections for the volume per formula unit makes the carrier density *per plane* 50% smaller in Bi2212 than in Tl2201. One may argue that it is not clear if $T_c = 90$ K Tl2201 is optimally doped, as the peak in T_c as a function of doping has not been observed for this material. However, the Bi2212 sample is doped close to optimal. The 50% larger carrier density substituted into the parabolic relation of the previous paragraph would make the $T_c = 90$ K Tl2201 a strongly overdoped material with hypothetical $T_c^{max} \simeq 190$ K! On the other hand, if $T_c = 90$ K = T_c^{max} for Tl2201, the whole idea of T_c being determined by the normal-state free-carrier density *per planar Cu* is put in question. One can assume that TlO planes may also be conducting, and therefore contribute to the low-frequency ab-plane conductivity SW. However, while theoretical estimates support this possibility, they predict that TlO planes contribute only a small fraction of the total SW. [Pickett92]

In an attempt to understand why progressive p-type doping does not produce a monotonic increase of the free-carrier density we examine how the dc transport properties evolve with doping. It has been reported that the room-temperature thermoelectric power coefficient (TEP) of HTSC cuprates has a universal behavior as a function of doping: it is large and positive in underdoped samples, almost zero in optimally doped samples and becomes small and negative upon crossing into the overdoped regime. [Obertelli92] The Hall coefficient R_H is large and positive in the underdoped regime, decreases in magnitude with doping and crosses zero somewhere in the overdoped regime. It was suggested, in an attempt to explain the doping dependence of R_H in $\text{La}_{2-x}\text{Sr}_x\text{CuO}_4$, that the zero crossing may be a result of a change

⁵The results of previous transmission measurements on overdoped Bi2212 [Kendziora93] indicate an increase in the conductivity SW in the frequency region 200-600 cm^{-1} upon overdoping. Although the authors interpreted it as an increase in the *total* SW, it may be a result of the SW redistribution as in Tl2201.

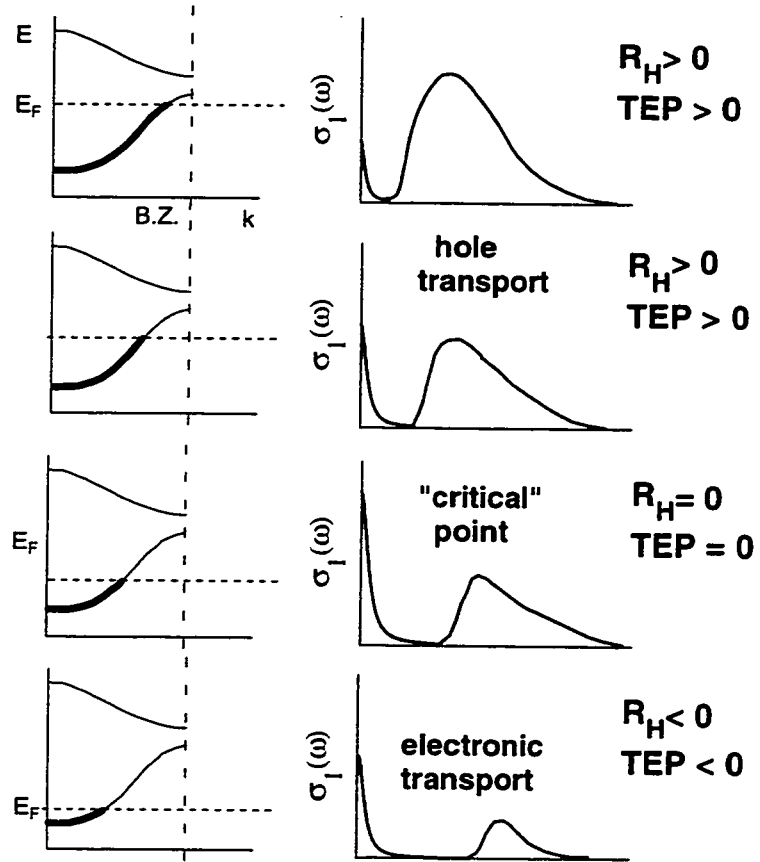


Figure 2.4: Evolution of optical conductivity as a function of a band filling in a simple two-band structure.

in the topology of the Fermi-surface from hole-like to electron-like. [Ong87, Allen87] Indeed, the doping dependence of TEP, which in a simple model is negative/positive for an electron/hole-like Fermi surface, [Ashcroft76] would support this scenario.

On the other hand $\sigma_1(\omega)$, unlike TEP and R_H , does not distinguish between the sign of the charge carriers and depends only on their density, that is on the volume of the (hole-like or electron-like) Fermi surface. In a simple rigid-band picture, illustrated in Fig. 2.4, the density of *mobile* charge carriers, and therefore the low-frequency conductivity SW, will attain its maximum as a function of doping at the band filling corresponding to an inflection point where the inverse effective mass goes to zero. This corresponds to a band filling at which the Fermi surface changes its topology from hole-like to electron-like as a function of p-type doping. As a result, Hall coefficient and TEP also change sign. Although these arguments are likely to be oversimplified and the rigid-band picture may not be applicable to the HTSC cuprates, the change of topology of the Fermi surface might provide a qualitative explanation for the observed turning point in the conductivity SW behavior as a function of doping. Another interesting implication of this result is that the highest T_c is achieved at the doping concentration corresponding to the highest density of states at the Fermi level. It remains unclear, however, why the scattering rate of the mobile carriers seems to decrease with overdoping.

In summary, our optical results show that, while in the underdoped regime, an increase in the low-frequency conductivity SW provides a clear indication of the increase in the free carriers density as T_c is increasing. Overdoping decreases T_c but does not lead to an increase in the conductivity SW. Therefore, *optical conductivity shows no signature of increasing mobile-carrier density with overdoping*. The doping-induced changes in $\sigma_1(\omega)$ in the overdoped regime are more consistent with a reduction in the scattering rate of the mobile carriers.

Note added in proof: Recently, Fukuzumi *et al.*, [Fukuzumi96] while using a completely different experimental approach, have arrived at a similar conclusion. In particular, their results suggest that the free-carrier density increases with doping in the underdoped regime, while it decreases with doping in the overdoped regime.

Chapter 3

The pseudogap state in the cuprate high- T_c superconductors

3.1 Introduction

There is mounting evidence that the normal state of underdoped high- T_c superconductors (HTSC) is dominated by a pseudogap. A number of physical probes show that below a characteristic temperature T^* , which can be well above the superconducting transition temperature T_c , the physical response of HTSC materials can be interpreted in terms of the formation of a partial gap or a pseudogap in the spectrum of low-energy excitations. This gap persists in the superconducting state. T^* decreases with increasing doping in the underdoped regime and since T_c rises with doping, the two curves meet at the optimal doping level, as shown in the schematic phase diagram in Fig. 3.1.

The earliest experiments to reveal gap-like behavior in the normal state were nuclear magnetic resonance (NMR) measurements of the Knight shift, [Warren89, Yoshinari90] which probes the uniform spin susceptibility. In conventional superconductors and the cuprates at optimal doping, the Knight shift is temperature independent in the normal state but drops rapidly below T_c due to pairing of electronic spins into (singlet) superconducting Cooper pairs. In underdoped cuprates, however, the Knight shift begins to drop well above the superconducting transition temperature. Warren *et al.* concluded that in these materials spin pairing takes place well above the bulk superconducting transition at T_c , thus producing a normal-state energy gap,

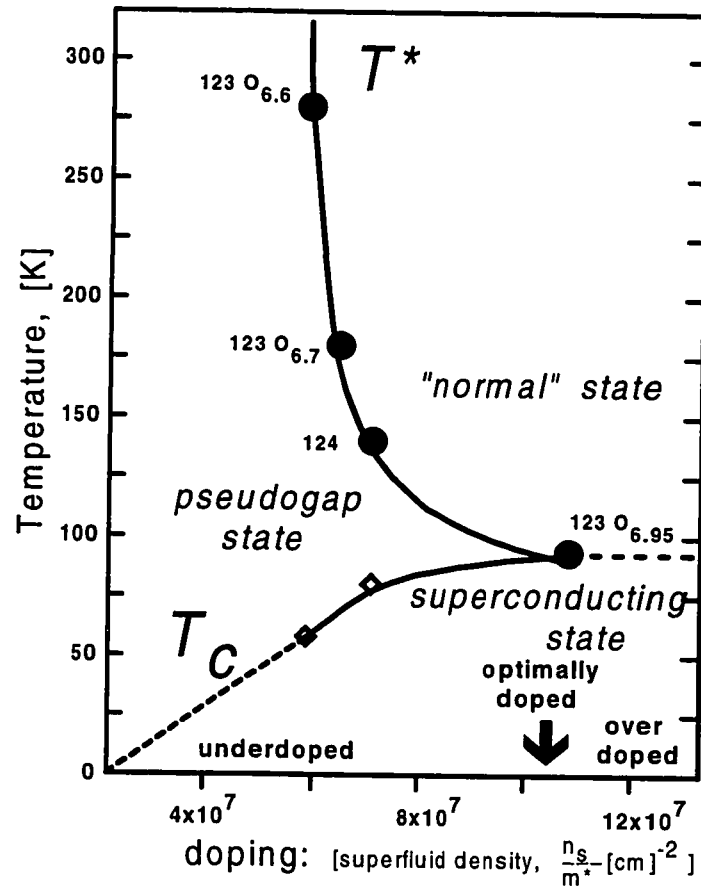


Figure 3.1: Schematic phase diagram of the cuprate superconductors. In the underdoped regime a pseudogap state forms below a temperature $T^* > T_C$. The curves for T^* and T_C cross at optimal doping where the pseudogap and the superconducting gap develop at the same temperature.

referred to as a "spin gap". [Warren89]

Deviations from the well known linear temperature dependence of the ab -plane resistivity, [Gurvitch87] $\rho_{ab}(T)$, were observed in underdoped cuprates as well, [Batlogg94, Bucher93, Ito93, Walkes93] with the slope of $\rho_{ab}(T)$ changing below a characteristic temperature T^* . As the doping is increased towards the optimal level, T^* decreases and the near-optimal doping $\rho_{ab}(T)$ is linear over the range of temperatures from T_c to above 800 K. [Batlogg94, Ito93]

The magnitude of T^* as well as its variation with doping suggest that the suppression of the spin susceptibility observed in NMR measurements and the change of slope of $\rho_{ab}(T)$ have a common physical origin. It has been suggested that if the scattering responsible for the linear temperature dependence of $\rho_{ab}(T)$ involves scattering on spin fluctuations, then the spin gap seen in NMR below T^* would naturally account for the depression of $\rho_{ab}(T)$ below T^* as well. Similar evidence for the suppression of the spin susceptibility has been extracted from neutron scattering experimental results. [Rossat-Mignod91, Tranquada92] Specific heat measurements on underdoped Y123, however, show that there is a large decrease in entropy below a temperature, closely related to T^* , which can not be accounted for by assuming that a gap in the spin degrees of freedom is solely responsible. [Loram94]

There is spectroscopic evidence of anomalies in the properties of HTSC that were originally associated with the formation of the superconducting gap, but were found to occur at $T > T_c$ in underdoped samples. The shift in the position and width of Raman frequencies of certain phonons, associated with the onset of superconductivity, [Friedl90] were shown to occur in the normal state of underdoped cuprates and it was suggested they were related to the spin gap. [Litvinchuk92] Similarly, broad peaks in the electronic Raman continuum, also interpreted as an evidence for the formation of a superconducting gap, [Cooper88] were found to occur well above T_c in underdoped samples. [Slakey90]

Indications of normal-state gap-like anomalies in underdoped cuprates were observed in the infrared optical measurements as well. The ab -plane reflectance results of most high temperature superconductors were found to have a structure in the form of a "knee" at approximately 500 cm^{-1} . This structure was sometimes interpreted as a manifestation of a conventional superconducting gap. It has been

found, however, that in underdoped materials the knee starts to develop in the normal state. [Kamarás90, Orenstein90, Reedyk88, Rotter91, Schlesinger90, Schlesinger94, Thomas88, Marel91] A comparison with other probes suggests that the knee structure and deviations observed in the dc transport and NMR experiments all occur at a characteristic temperature remarkably similar to T^* . The corresponding changes in the complex optical conductivity $\sigma(\omega) = \sigma_1(\omega) + i\sigma_2(\omega)$ involve a shift of part of the $\sigma_1(\omega)$ spectral weight from 300-700 cm^{-1} to *lower* frequencies, resulting in a formation of a highly coherent narrow low-frequency peak. This behavior is in accord with decreasing dc resistivity and was interpreted in terms of coupling of electrons to the longitudinal optical (LO) phonons [Reedyk92, Timusk91] or as a manifestation of the spin gap. [Orenstein90, Rotter91, Schlesinger94]

It should be emphasized that in the case of a *coherent* system, such as the underdoped cuprates in *ab*-plane direction, there is no direct mapping between the electronic density of states (DOS) and the shape of the real part of conductivity, $\sigma_1(\omega)$. For example, even if there is a gap in the electronic DOS and its magnitude is larger than the characteristic energy associated with the *elastic* scattering (clean limit [Kamarás90, Timusk88]), the gap will not manifest itself in the $\sigma_1(\omega)$ spectra. In the same way, a pseudogap in the electronic DOS of a coherent system, that may appear due to strong interactions in the system, does not manifest itself as an obvious gap in the conductivity.

The charge dynamics along the interplane *c*-direction is *incoherent*, at least in the underdoped materials. While both underdoped Y123 and Y124 compounds, collectively referred as YBCO, exhibit a gap-like depression in the *c*-axis conductivity as well, [Basov94, Homes93b, Tajima95] the *c*-axis conductivity shows no coherent peak at low frequencies, Fig. 3.2. Contrary to the *ab*-plane response, as the temperature decreases from 300 K to T_c the *c*-axis $\sigma_1(\omega)$ spectral weight is transferred from the gap region to *higher* frequencies. [Homes93b, Legget92] The magnitude of the low-frequency conductivity is in good agreement with the dc resistivity [Homes95] which shows a "semiconducting" behavior (i.e. resistivity increases at low T). A number of mechanisms have been proposed that would result in an incoherent conductivity spectrum. [Alexandrov, Clarke95, Graf93, Ioffe93, Kumar90, Kumar92, Nyhus95, Rojo93] The *c*-axis conductivity depression in both Y123 and Y124 occurs at a temperature

scale that matches the spin susceptibility determined from the NMR measurements. This is shown in the inset of Fig. 3.2 where the Knight shift [Takigawa91] is shown along with the experimental c -axis conductivity. The onset energy of the c -axis gap in YBCO is $\approx 200 \text{ cm}^{-1}$ and the half value point is $\approx 300 \text{ cm}^{-1}$. Above 500 cm^{-1} , the c -axis conductivity is both temperature and frequency independent. [Homes95]

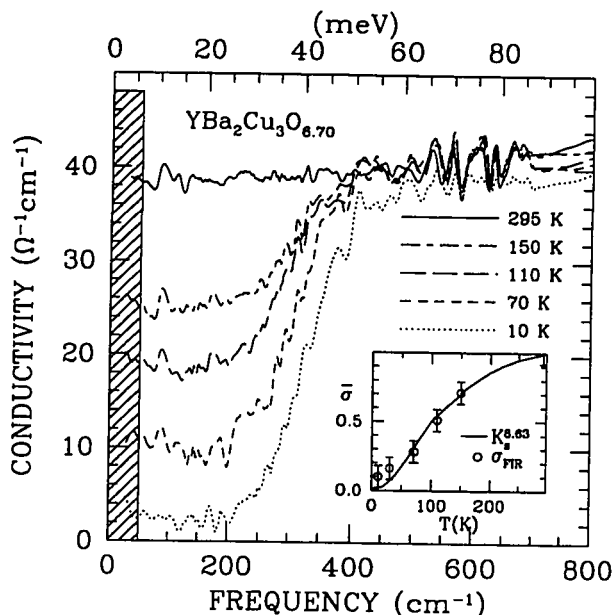


Figure 3.2: The c -axis conductivity of an underdoped Y123 crystal. After Homes *et al.* [Homes95]. As the temperature is lowered the pseudogap develops. The inset: The NMR Knight shift (normalized at 300 K) is plotted as a function of temperature for an underdoped Y123 crystal. The circles show the low frequency c -axis conductivity for samples of the same doping level.

A pseudogap has also been observed in the c -axis conductivity of La214 where for $x=0.14$ a very large gap has been reported [Basov95] and for $x=0.12$ a gap of the same magnitude as in YBCO can clearly be seen. [Uchida96] The $\text{Pb}_2\text{Sr}_2(\text{Y}/\text{Ca})\text{Cu}_2\text{O}_8$ material also shows a c -axis pseudogap. [Reedyk96]

Recent angular-resolved photoemission (ARPES) results for Bi2212 show evidence of a normal-state gap-like depression of the electronic density of states of underdoped cuprates as well. [Ding96, Loeser96, Marshall96] The momentum dependence of this gap resembles that of the $d_{x^2-y^2}$ gap observed in the superconducting state.

[Loeser96] This, and the fact that no significant changes are observed upon crossing into the superconducting regime, have led to the suggestion that the normal-state gap may be a precursor of the superconducting gap. As the doping level is increased to near- and above optimal the normal-state gap-like feature disappears.

In the following, we summarize the recent experimental optical results obtained from several series of HTSC materials at doping levels ranging from underdoped to strongly overdoped. We use experimental results obtained by the author of the thesis (Bi2212, (Bi/Pb)2212, Tl2201), as well as by D.N. Basov *et al.* (Y123, Y124). We find that in the pseudogap state the optical response of underdoped cuprates is marked by an abrupt increase in coherence of the electronic system. Since the coherence effects are seen more clearly through the frequency dependent charge-carrier scattering, or through memory function analysis, we have chosen to use this approach. The essential features of this very general formalism are described in Appendix A. We will briefly address the question of the correlation between the *ab*-plane and the *c*-axis pseudogap properties.

3.2 Experimental details

We have performed reflectivity measurements, at temperatures ranging from 10 K to 300 K, on two underdoped ($T_c=67$ K and $T_c=82$ K), one optimally doped ($T_c = 90$ K), and one overdoped ($T_c=82$ K) Bi2212 single crystal. All the Bi2212 crystals were prepared from the as-grown crystals by annealing in argon and/or oxygen.[Fournier96, Kolesnikov95] To achieve a higher degree of overdoping we have performed measurements on Pb-doped Bi2212 $\text{Bi}_{1.66}\text{Pb}_{0.34}\text{Sr}_2\text{CaCu}_2\text{O}_{8+l\delta}$ ((Bi/Pb)2212) with $T_c=70$ K (optimum $T_c=88$ K). The two T2201 single crystals used in the measurements had T_c 's of 90 K (highest T_c achievable) and 23 K (strongly overdoped). The superconducting transition temperatures for all samples were measured in a SQUID magnetometer.

The frequency ranges of the reflectivity measurements, as well as the low- and high-frequency reflectivity approximations for the KK analysis, for Bi2212 and Tl2201 materials are described in section 2.2. The (Bi/Pb)2212 material has been measured optically from 30-8000 cm^{-1} . Above 8000 cm^{-1} reflectivity results for Bi2212 material were used. The low-frequency approximation was done using the Hagen-Rubens

formula (section 1.1.6) while the high frequency approximation was the same as for Bi2212 materials.

Experimental details concerning the Y123 and Y124 material, measured by D.N. Basov, can be found in the original paper. [Puchkov96d]

3.3 Experimental results

This section is divided into three subsections: underdoped, optimally doped and overdoped materials. In each of the subsections we first present the raw experimental results in the form of absorption $A(\omega) = 1 - R(\omega)$ for a selected material at many different temperatures. Before we proceed to the memory function analysis, we will also present the results for the same material in terms of the more commonly used real optical conductivity $\sigma_1(\omega)$. However, we will focus the analysis on the real and imaginary parts of the memory function $M(\omega) = M'(\omega) + iM''(\omega)$, that will be presented for several materials on a second diagram in each subsection. While for a selected material in each subsection we will show many different temperatures, to simplify the diagrams for others, only three temperatures will be shown: $T=300$ K, $T \simeq T_c$ and the lowest (superconducting) temperature.

As described in Appendix A, we are fully aware that in most real situations, and especially in HTSC, the real and imaginary parts of $M(\omega)$ are not solely determined by the scattering effects and the corresponding enhancement of an effective mass. Nevertheless, mostly for historical reasons, we will refer to the effective scattering rate and to the effective mass defined as $1/\tau(\omega) = M'(\omega)$ and $m^* = 1 + \lambda(\omega) = 1 - M''(\omega)/\omega$ respectively. Keeping this in mind, we will now present the experimental results and indicate the common trends, leaving the interpretation for the discussion section. Since we will mainly be interested in the evolution of the optical response in the pseudogap energy region we will present the experimental data up to 2000 cm^{-1} only.

3.3.1 Underdoped cuprates.

A typical plot of the temperature dependence of raw absorption data $A(\omega, T)$ for an underdoped HTSC is shown in Fig. 3.3, this particular example being underdoped

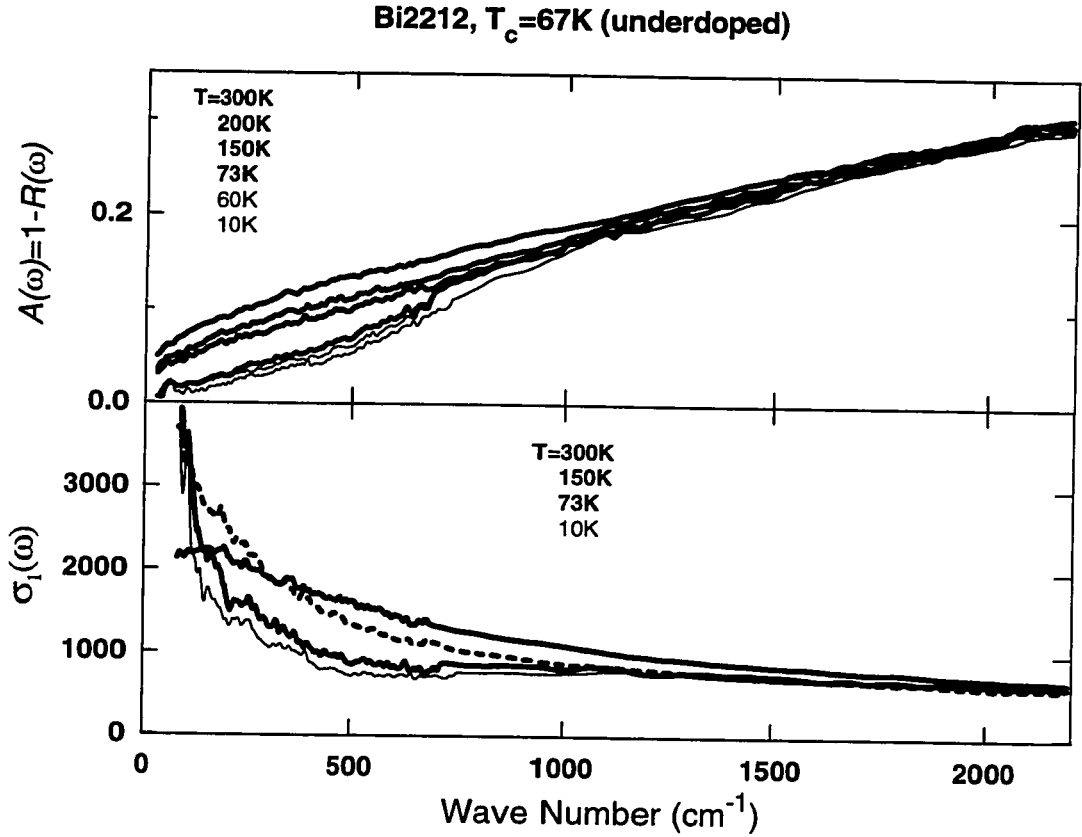


Figure 3.3: Absorption and optical conductivity for underdoped Bi2212. The absorption $A = 1 - R$, top panel, and the optical conductivity $\sigma_1(\omega)$ for underdoped B2212 ($T_c = 67$ K). The absorption rises linearly at high temperatures but develops a depression below 800 cm^{-1} due to the formation of the pseudogap. In the optical conductivity the pseudogap shows up as a narrowing of the coherent Drude peak at low frequency (the dashed curve corresponds to $T=150$ K).

Bi2212 material with $T_c = 67$ K. In the temperature range 300-150 K the absolute value of the low-frequency absorption decreases smoothly with decreasing temperature without any sharp features. However, at a temperature $T < T^* \simeq 150$ K, the absorption below $600\text{-}700\text{ cm}^{-1}$ starts to decrease faster than at higher frequencies, developing a threshold structure which is characteristic for an underdoped HTSC in the pseudogap state.

The corresponding changes in the real part of optical conductivity $\sigma_1(\omega)$ are also shown in Fig. 3.3 at selected temperatures. The in-plane response of all samples is metallic, *i.e.* the absolute value of $\sigma_1(\omega)$ decreases from its dc value with increasing ω . However, while the $\sigma_1(\omega)$ spectra are quite broad at temperatures above T^* , the rapid decrease of the low-frequency absorption below T^* results in an abrupt narrowing of the low-frequency conductivity with substantial spectral weight being transferred towards zero frequency. As the temperature is reduced below T_c , no dramatic changes are observed in the optical response of underdoped cuprates: the only change is just a *continued* narrowing of the intense low-frequency peak, that was already initiated in the normal state.

The scattering rate $1/\tau$ and the effective mass $m^*/m_e = 1 + \lambda$ for the Bi2212 crystal with $T_c = 67$ K, calculated from the optical conductivity using the formulae described in Appendix A, are shown in Fig. 3.4. We have used a plasma frequency value of $\omega_p = 14300\text{ cm}^{-1}$, obtained by using the conductivity sum-rule analysis [Puchkov96b, Timusk89] with integration of $\sigma_1(\omega)$ over all frequencies up to 1 eV. We note that the value of ω_p obtained in this way is somewhat ambiguous since there is no clear separation between the frequency regions of the free- and bound-carrier optical responses. However, a particular choice of ω_p only affects the absolute value or, in other words, sets up the units of measuring $1/\tau(\omega)$ and $m^*(\omega)$. Since in this section we are mostly interested in the *frequency dependence* of these quantities, the exact value of ω_p is not of primary importance. To keep the absolute values consistent, in the Bi2212 and Tl2201 series, we will use plasma frequency values obtained by integrating the real part of optical conductivity up to 1 eV, which seems to be an energy below which the conductivity is substantially changed by doping. [Orenstein90, Puchkov96b] In the YBCO series an energy of 1.5 eV was used as an upper integration limit since the reflectivity plasma minimum is higher for these materials. [Timusk89]

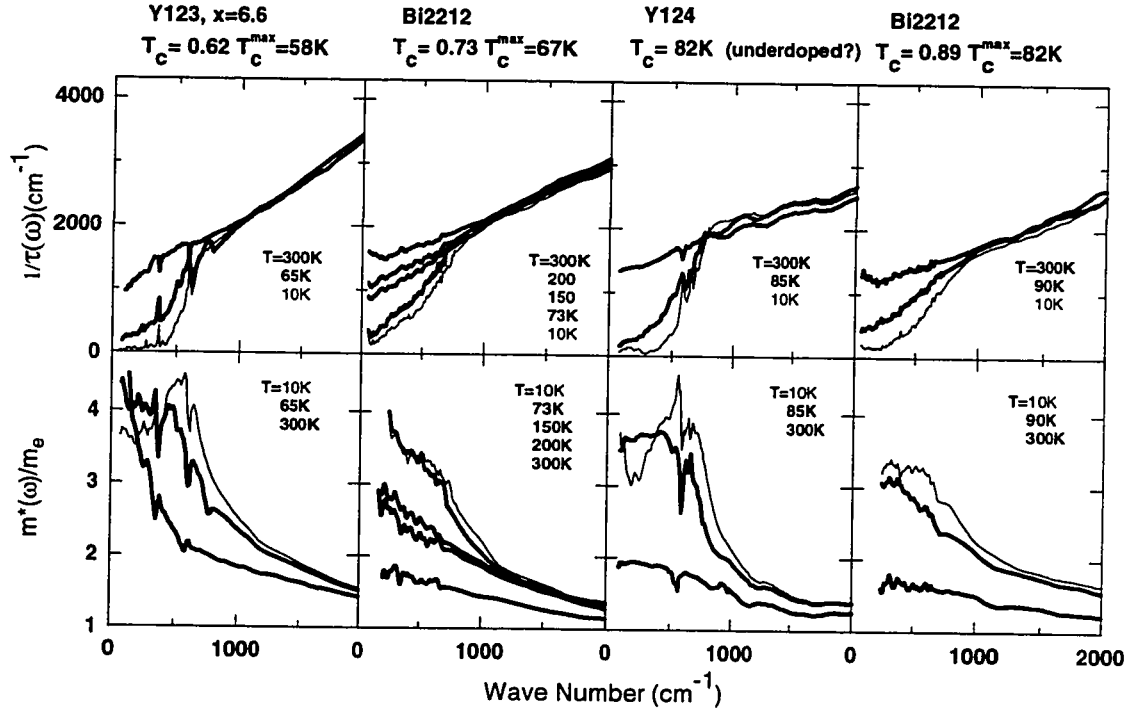


Figure 3.4: Memory function for underdoped cuprates. The frequency dependent scattering rate, top row, and the mass renormalization, bottom row, for a series of underdoped cuprate superconductors. The scattering rate curves are essentially temperature independent above 1000 cm^{-1} but develop a depression at low temperatures and low frequencies. The effective mass is enhanced at low temperatures and low frequencies. Results on Y124 and Y123 materials were obtained by D.N. Basov *et al.*

The scattering rate $1/\tau(\omega)$ of underdoped Bi2212 with $T_c = 67$ K is linear at frequencies from 800 cm^{-1} to at least 3000 cm^{-1} at all temperatures. While at room temperature the low-frequency $1/\tau(\omega)$ deviates upwards from the high-frequency linear law, at $T = 200\text{K}$ the spectrum is linear over the whole frequency range from $100\text{-}3000 \text{ cm}^{-1}$. However, as temperature is reduced below T^* , the scattering rate is suppressed more rapidly at low frequencies ($\omega < 700 \text{ cm}^{-1}$) while it remains nearly unaffected at higher energies. A result of this development is an appearance of a distinct threshold in the $1/\tau(\omega)$ spectra. Another interesting phenomenon, that we will return to later, is the remarkable temperature-independence of the high-frequency $1/\tau(\omega)$.

Similar to other quantities, the effective mass $m^*(\omega)$ displays a rapid change at frequencies below 700 cm^{-1} as the temperature is reduced below T^* . We note that the narrowing of the low-frequency optical conductivity is a result of *both* a decrease of $1/\tau(\omega)$ and an increase of $m^*(\omega)$ since heavy carriers are more difficult to scatter. The width of a conductivity peak is determined by a renormalized scattering rate $1/\tau^*(\omega) = m_e/(\tau(\omega)m^*(\omega))$. At low temperatures the effective mass saturates at $m^*(0) \simeq 3 - 4$.

The experimental results obtained for several other cuprate materials at different doping levels in the underdoped state are qualitatively similar. In the rest of Fig. 3.4. we show the effective scattering rate and the carrier mass obtained for Y123 with oxygen content $x = 6.6$ and $T_c = 58$ K, naturally underdoped Y124 with $T_c = 80$ K, and slightly underdoped Bi2212 with $T_c = 82$ K. The in-plane plasma frequency ω_p , related to the conductivity by $\omega_p^2/8 = \int_0^\infty \sigma_1(\omega)d\omega$, scales with T_c in accordance with earlier measurements. [Orenstein90, Puchkov96b] Integration of the conductivity up to 1.5 eV yields the following values of the plasma frequency: 15000 cm^{-1} in $\text{YBa}_2\text{Cu}_3\text{O}_{6.6}$, 16000 cm^{-1} in $\text{YBa}_2\text{Cu}_4\text{O}_8$ and 15600 cm^{-1} in Bi2212. For clarity, only three temperatures are shown for each material: room temperature, just above T_c and well below T_c .

All of the samples show the same characteristic suppression of the amplitude of the scattering rate at $T < T^*$, which seems to increase as doping level decreases. Despite the differences in the values of T^* in the different samples, the energy scale associated with the suppression of $1/\tau(\omega)$, does not change significantly with dop-

ing. In particular, a deviation from the linear behavior in all studied samples occurs at the same frequency $\omega < 700 \text{ cm}^{-1}$. As the doping level is increased towards the optimal, the normal state depression of $1/\tau(\omega)$ becomes progressively shallower, while in the superconducting state the depression remains almost unchanged. The net effect is that the difference between the low-temperature normal-state and the superconducting-state $1/\tau(\omega)$ becomes more prominent as doping level approaches the optimal. At the same time, qualitatively, the shape of the normal-state $1/\tau(\omega)$ at $T < T^*$ remains similar to that in the superconducting state. With the exception of the Y124 sample, the high-frequency $1/\tau(\omega)$ is linear up to at least 3000 cm^{-1} (2000 cm^{-1} for Y124) and for all samples it is nearly temperature-independent. The low-temperature effective mass $m^*(\omega)$ becomes enhanced at low frequencies when temperature is reduced below T^* . In all samples $m^*(\omega)$ saturates at about the same value of $\approx 3 - 4$.

To summarize, the optical response of underdoped cuprates is characterized by the following generic features: (i) the scattering rate is nearly linear with ω at $T > T^*$; (ii) At $T < T^*$ (the pseudogap state) the low-frequency scattering rate is suppressed corresponding to the rapid narrowing of the Drude-like feature in the conductivity spectra. The energy scale associated with the changes of $1/\tau(\omega)$ spectra was found to be the same in all samples. The magnitude of the depression becomes smaller as doping is increased towards the optimal level. (iii) The high-frequency $1/\tau(\omega)$ remains effectively temperature-independent and linear from 700 cm^{-1} up to at least 3000 cm^{-1} in most underdoped HTSC samples.

3.3.2 Optimally doped and lightly overdoped cuprates.

A similar threshold structure in the raw absorption spectra is observed in the optimally doped crystals as well. As an example, in Fig. 3.5 we show absorption and conductivity data obtained from optimally doped Y123 material. The important difference from the underdoped cuprates is that now a threshold in $A(\omega)$ develops only at temperatures below T_c . The corresponding $1/\tau(\omega)$ and $m^*(\omega)$ spectra are plotted in Fig. 3.6. We have used a plasma frequency $\omega_p = 18000 \text{ cm}^{-1}$, obtained from the sum-rule analysis with integration up to 1.5 eV . All of the optical constants show the same characteristic features as in underdoped cuprates but the onset tempera-

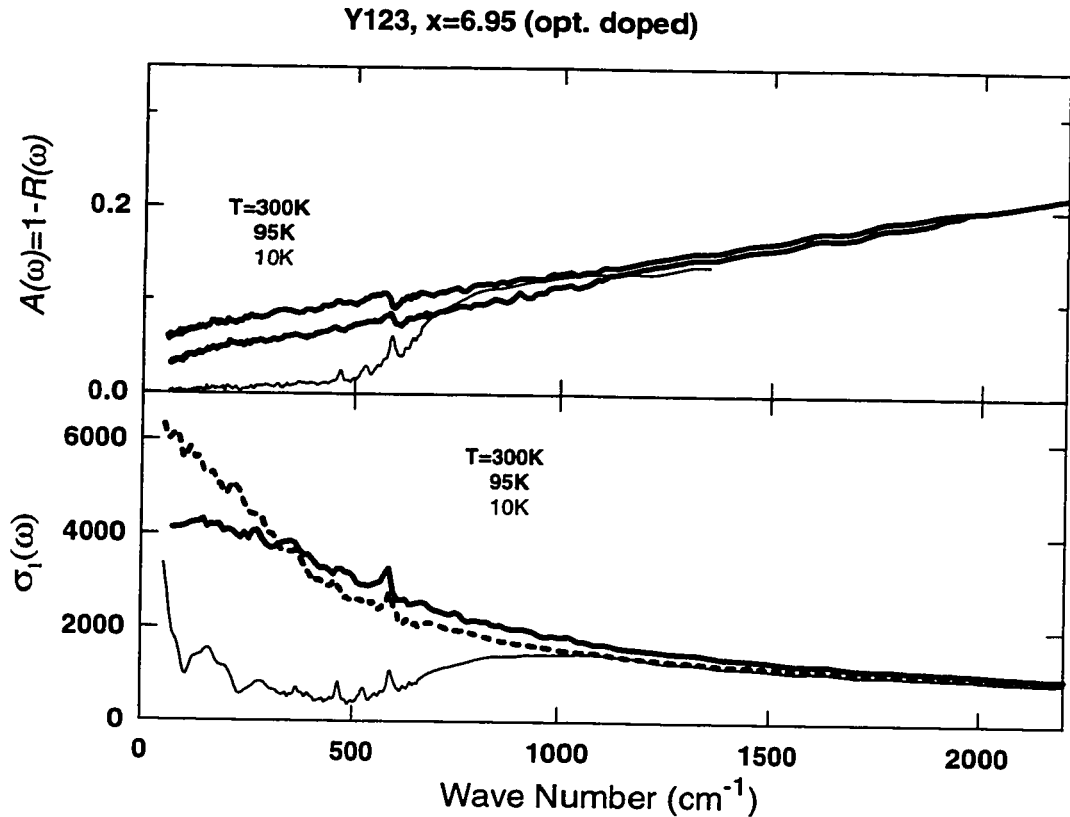


Figure 3.5: Absorption and optical conductivity for optimally doped Y123. The absorption $A = 1 - R$ and the optical conductivity for optimally doped Y123 with $x = 6.95$ ($T_c = 93.5$ K). Results are obtained by D.N. Basov. A depression of A is seen below 800 cm^{-1} but only below the superconducting transition temperature T_c . The same is true for the characteristic narrowing of the optical conductivity (the dashed line corresponds to $T=95$ K).

ture now is determined by T_c . A remarkable feature of the optimally doped samples is the similarity between the behavior of the superconducting-state optical response obtained in these crystals with the data obtained in the underdoped materials at $T_c < T < T^*$. This may suggest a similar nature in the physical processes that lead to the formation of the pseudogap state and superconducting state. This would be consistent with the notion that the T_c and T^* boundaries in Fig. 3.1 cross around the optimal doping. As a result, the difference between the normal-state and the superconducting state spectra becomes dramatic in optimally doped samples.

In the normal state, as the temperature is reduced from 300 K down to $T \simeq T_c$, both the scattering rate and the renormalized effective mass, in optimally doped samples, show relatively minor changes. These changes are mainly restricted to the decrease of the absolute value of $1/\tau(\omega)$ in the low frequency parts of the spectra. However, in contrast to the underdoped materials, the normal-state scattering rate in Y123 does not reveal any sharp changes in the frequency dependence as temperature is reduced.

In the rest of Fig. 3.6 we show data obtained on Bi2212 with $T_c = 90$ K and Tl2201 with $T_c = 90$ K. We should note that although we assigned the material Tl2201 to this section, the peak in T_c as a function of doping has not yet been observed for Tl2201 and some data suggest that this material may be somewhat overdoped. [Puchkov96b] The plasma frequency used for Bi2212 was $\omega_p = 16000 \text{ cm}^{-1}$ and for Tl2201 $\omega_p = 15300 \text{ cm}^{-1}$. The normal-state spectra of $1/\tau(\omega)$ are featureless. In case of Tl2201 the threshold structure appears only at $T < T_c$ but in Bi2212 a weak structure can still be seen at $T=90$ K. In fact, it persists even in the lightly overdoped samples. Thus it is possible that the pseudogap state in Fig. 3.1 can somewhat penetrate into the overdoped regime. Qualitatively, the depression in $1/\tau(\omega)$ at $T < T_c$ in the optimally doped cuprates is very similar to what is observed in the $1/\tau(\omega)$ spectra in the pseudogap state of the underdoped cuprates. However in contrast with the underdoped materials, the temperature dependence of the scattering rate now seems to extend over a broader frequency range. In particular, in the Bi2212 and Tl2201 samples the $1/\tau(\omega)$ spectra reveal some shift in the high-frequency part (above the 700 cm^{-1} threshold) whereas in the underdoped materials no temperature dependence was observed at these frequencies.

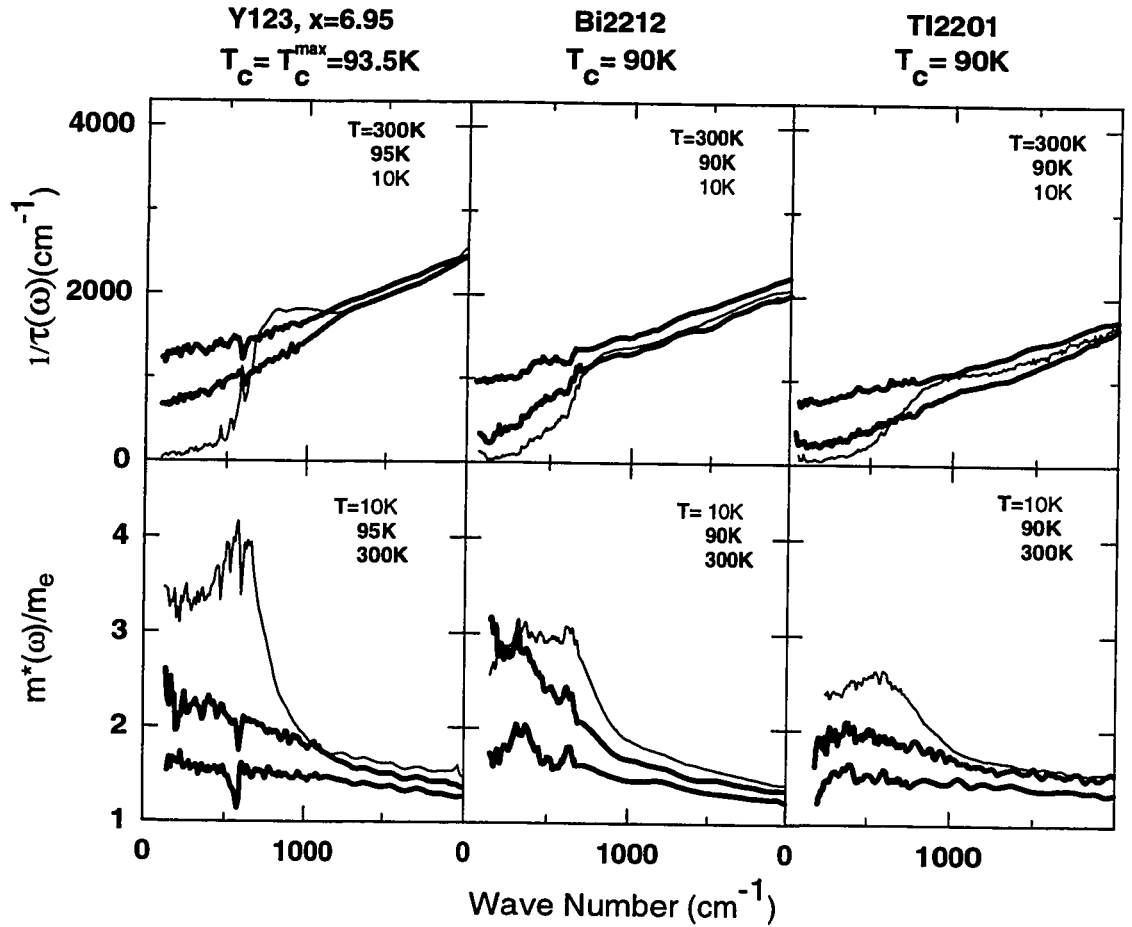


Figure 3.6: Memory function for optimally doped cuprates. The scattering rate and the effective mass for the cuprate superconductors doped close to optimal. The scattering rate now has a degree of temperature dependence at low frequencies. In the superconducting state the scattering rate is depressed at low frequencies.

Another weak feature that seems to be common for both the optimally doped Y123 and $T_c = 90$ K Tl2201 is an "overshoot" of the superconducting-state $1/\tau(\omega)$ above the spectrum of $1/\tau(\omega)$ for $T \simeq T_c$.

In summary, the response of the optimally doped high- T_c cuprates demonstrates the following features: (i) A threshold feature in $1/\tau(\omega)$ spectra is either strongly suppressed or disappears completely when the doping level approaches optimal; (ii) The high-frequency $1/\tau(\omega)$ remains linear but may acquire a weak temperature dependence in lightly overdoped cuprates.

3.3.3 Overdoped cuprates.

Since the strongly overdoped regime is not accessible in the Bi2212 or in the YBCO materials, we have chosen Tl2201, (Bi/Pb)2212 and slightly overdoped Bi2212 in order to study this doping regime. In Fig. 3.7 we show the data for a strongly overdoped high- T_c superconductor (Tl2201 with $T_c = 23$ K). The raw absorption spectra are qualitatively different from those obtained in optimally doped or underdoped regimes. $A(\omega)$ is temperature-dependent over a much broader frequency range. The spectra shift down uniformly as temperature decreases but no sharp features develop. Unfortunately, in this crystal absorption is already very small in the normal state at $T = 35$ K. It is difficult to determine the exact shape of $A(\omega)$ in the superconducting state. Thus it remains unclear if the absorption spectra of this crystal show the same threshold structure as the less heavily doped materials.

The $\sigma_1(\omega)$ spectra for the strongly overdoped Tl2201 are shown in the bottom panel of Fig. 3.7 while $1/\tau(\omega)$ and $m^*(\omega)$ spectra are shown in Fig. 3.8. The plasma frequency is $\omega_p = 15100$ cm^{-1} . Consistent with the behavior of the absorption spectra there is no sharp change in the frequency dependence in any of these response functions as the temperature is decreased in the normal state. Instead, the $1/\tau(\omega)$ spectra scale downwards almost parallel to each other. This is in sharp contrast with the $1/\tau(\omega)$ behavior in the underdoped regime, where the scattering rate was found to be temperature independent above 1000 cm^{-1} . We also note that the frequency dependence of $1/\tau(\omega)$ for this strongly overdoped material may become superlinear, flattening out at low frequencies. The effective mass $m^*(\omega)$ does not show any pronounced temperature dependence and remains largely flat in the whole frequency

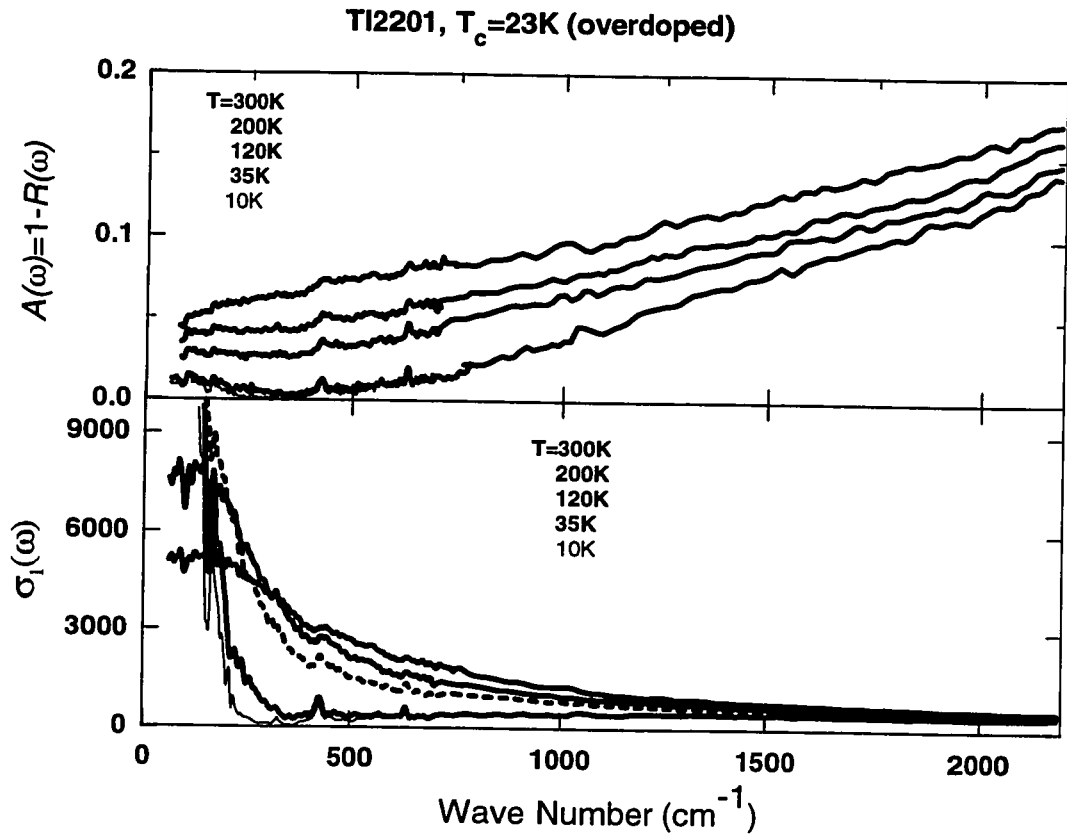


Figure 3.7: Absorption and optical conductivity for overdoped Tl2201. The absorption of strongly overdoped Tl2201 ($T_c = 23\text{ K}$), top panel, and the optical conductivity, lower panel. The absorption is strongly temperature dependent but no threshold develops at low temperatures. The optical conductivity becomes narrower as temperature decreases but does not show any sharp changes (the dashed line corresponds to $T=120\text{ K}$).

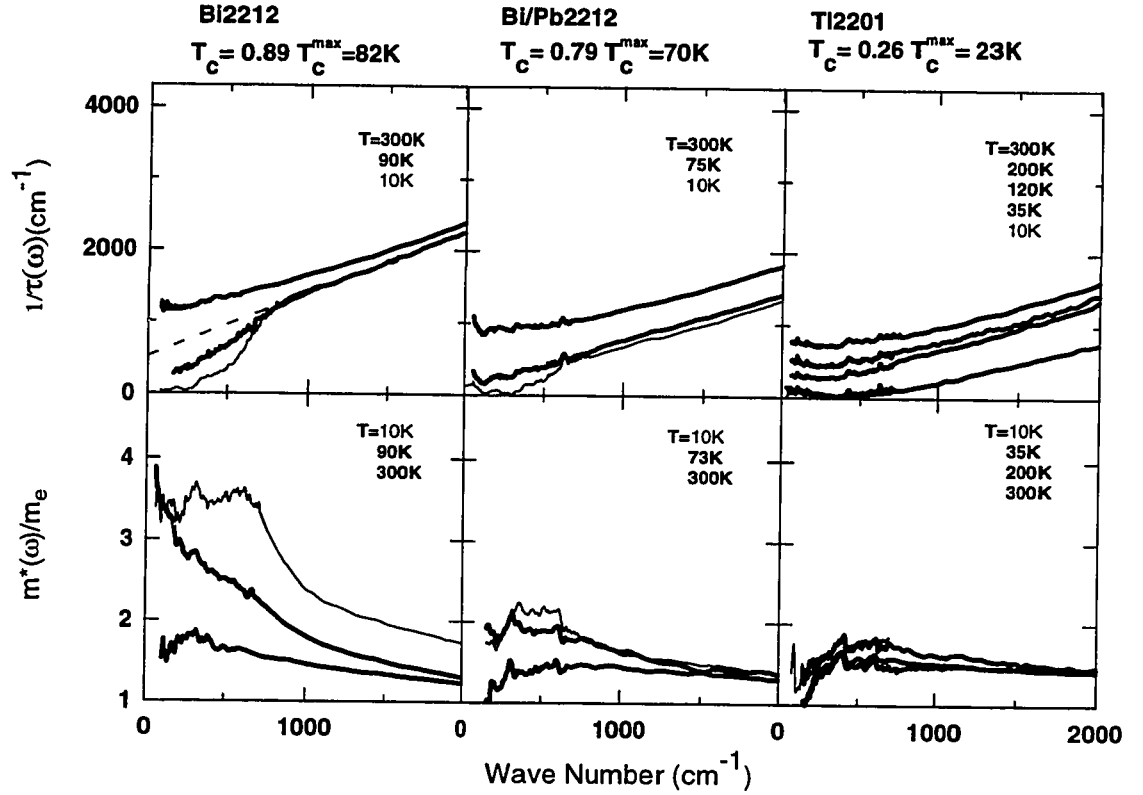


Figure 3.8: Memory function for overdoped cuprates. The scattering rate, top row, and the effective mass, bottom row, for the overdoped cuprates. In overdoped samples the high-frequency scattering rate shows an increasingly strong temperature dependence. As a part of the high-frequency scattering disappears at low temperatures, the low-frequency depression of $1/\tau(\omega)$ and the effective mass enhancement decrease in magnitude, even in the superconducting state.

region shown. To show the continuity in the evolution of the optical response of the cuprates from under- and optimally doped to the strongly overdoped case we plot $1/\tau(\omega)$ and $m^*(\omega)$ spectra for other overdoped samples in the rest of Fig. 3.8. These include Bi2212 ($T_c = 82$ K) and (Bi/Pb)2212 ($T_c = 70$ K) annealed in oxygen ($\omega_p = 15600$ cm^{-1} for Bi2212 and 16500 cm^{-1} for (Bi/Pb)2212). As we have noted in the previous section, the $1/\tau(\omega)$ spectrum for slightly overdoped Bi2212 still shows a weak normal-state pseudogap feature at $T=90$ K, defined as a downwards deviation from the linear high-frequency behavior. However, (Bi/Pb)2212 shows no sign of a threshold formation above T_c . While the scattering rate remains close to linear in ω at high frequencies, it seems to gradually pick up a temperature dependence as the doping level is increased from the optimal to overdoped. Also, the absolute value of the scattering rate is gradually suppressed with increased doping.

In the superconducting state the threshold structure seems to weaken as doping is increased towards strong overdoping. Correspondingly, the superconducting-state mass enhancement also becomes weaker. Unfortunately, as in the case of absorption, we can not unambiguously determine the exact nature of the changes that occur below T_c in either $1/\tau(\omega)$ or $m^*(\omega)$ for the Tl2201 sample with $T_c = 90$ K.

In summary, as the doping level is increased above optimal to overdoped and strongly overdoped levels: (i) No threshold is observed in $1/\tau(\omega)$ at $T > T_c$. (ii) The scattering rate $1/\tau(\omega)$ acquires temperature dependence over a much broader frequency range than in underdoped cuprates. (iii) The frequency dependence of $1/\tau(\omega)$ may become superlinear in the strongly overdoped cuprates.

3.4 Discussion

3.4.1 General trends in $1/\tau(\omega)$ data.

With regards to the underdoped cuprates, two distinct features in the $1/\tau(\omega)$ spectra deserve mentioning. First, it must be recognized that $1/\tau(\omega)$ is linear and almost temperature independent at high frequencies. Second, a threshold structure develops at low frequencies and temperatures below T^* . When the doping reaches the optimal level the threshold structure in the ab-plane scattering rate shows up only in the superconducting state. This is in accord with the phase diagram where the two

Table 3.1: The linear-fit parameters for the high-frequency $1/\tau(\omega)$.

The slopes and zero-frequency intercepts of the high-frequency linear part of $1/\tau(\omega) = \alpha\omega + \beta$, third and fourth columns. The linear coefficients normalized to the plasma frequency, $\alpha' = 4\pi\alpha/\omega_p^2$ and $\beta' = 4\pi\beta/\omega_p^2$, fifth and sixth columns. The fit was performed over a frequency range from 900-3000 cm^{-1} . The Y124 material is not shown since the high-frequency scattering rate significantly deviates from linear above 2000 cm^{-1} .

Material	T_c	α	$\beta(\text{cm}^{-1})$	$\alpha'(\mu\Omega\text{cm}^2)$	$\beta'(\mu\Omega\text{cm})$
Y123 (u.d)	58 K	1.26 (1.45)	790 (560)	0.34 (0.39)	210 (149)
Y123 (opt.d)	93.5 K	0.79 (0.93)	890 (590)	0.15 (0.17)	165 (108)
Bi2212 (u.d.)	67 K	0.84 (0.91)	1280 (1200)	0.25 (0.27)	377 (352)
Bi2212 (u.d)	82 K	0.76 (0.95)	990 (750)	0.19 (0.23)	243 (185)
Bi2212 (opt.d.)	90 K	0.71 (0.72)	850 (650)	0.17 (0.17)	200 (150)
Bi2212 (o.d.)	82 K	0.73 (0.77)	890 (550)	0.18 (0.19)	219 (135)
(Bi/Pb)2212 (o.d.)	70 K	0.63 (0.65)	551 (118)	0.13 (0.14)	117 (25)
Tl2212 (o.d.?)	90 K	0.64 (0.75)	473 (90)	0.16 (0.19)	121 (23)
Tl2212 (o.d.)	23 K	0.63 (0.54)	337 (-318)	0.17 (0.14)	89 (-84)

curves, the pseudogap boundary and the superconducting transition temperature T_c , cross at optimal doping ($T^* \leq T_c$). In the overdoped cuprates the threshold structure appears only below T_c and seems to become weaker even in the superconducting state as doping progresses. Unfortunately, the limitations of our experiment do not allow us to say with certainty if the structure persists in the strongly overdoped materials. The important difference between $1/\tau(\omega)$ for overdoped and underdoped materials is a strong temperature dependence of the high-frequency part of $1/\tau(\omega)$ in the overdoped case.

The common feature in all spectra is the linear in frequency dependence of the high-frequency scattering rate. The linear frequency dependence has been seen previously in the scattering rate of the a -axis Y123 both in the optimally doped and underdoped spectra. [Rotter91, Schlesinger90] In Table. 3.1 we present the slopes and zero-frequency intercepts of the high-frequency part of scattering rate obtained by fitting it to a straight line $1/\tau(\omega) = \alpha\omega + \beta$. The results are presented at two temperatures: $T=300$ K and at the lowest normal temperature (in parentheses).

We note here that the coefficients determined directly from $1/\tau(\omega)$ may be ambiguous since they involve the plasma frequencies that were obtained by integrating

the real part of conductivity up to a somewhat arbitrarily chosen frequency. However, the same cut-off integration frequency was used for each of the series at all doping levels (1.5 eV for YBCO and 1 eV for Bi2212 and Tl2201). While the absolute value of ω_p obtained in this manner may still be ambiguous, the *changes* in ω_p with doping reflect changes in the carrier density for each of the material series (see discussion in chapter 2). For these reasons the materials presented in Table. 3.1 are grouped by series. Another way to get around the problem of the unknown plasma frequency is to divide the scattering rate by ω_p^2 : $4\pi/(\omega_p^2\tau)$. This quantity may be called "optical resistivity", or ρ_{opt} , since it has the same functional form as a dc resistivity in a simple Drude model (Eq. 1.42 at $\omega = 0$). Since it is directly obtained from the measured complex optical conductivity: $\rho_{opt}(\omega) = Re(1/\sigma(\omega))$, it may be useful to examine variations of the slope and zero-frequency intercept of $\rho_{opt}(\omega)$ instead of $1/\tau(\omega)$. The corresponding results are listed in the last two columns of Table. 3.1.

The result of both approaches is that both α and β seem to decrease with doping for all of the series. However, while the decrease in the slope is insignificant (and may even be inside our error bar estimated to be about 20%), the drop in the intercept, especially its low-temperature value, is dramatic. We also note the large difference between the room-temperature and low-temperature (numbers in parenthesis) intercept values in the overdoped cuprates, which is a result of the strong temperature dependence of the high-frequency part of $1/\tau(\omega)$. The low-temperature intercept even becomes negative for strongly overdoped Tl2201.

The low intercept values in overdoped cuprates suggest that the temperature dependence and the low-frequency threshold in $1/\tau(\omega)$ are closely related. The strong temperature-induced suppression of $1/\tau(\omega)$ over a large frequency range makes the high-frequency background at $T \simeq T_c$ very small. Any further suppression of $1/\tau(\omega)$, similar to that observed in under- and optimally doped samples, could potentially produce only a weak feature that would be difficult to detect experimentally.

To conclude this sub-subsection, we make a comparison between our data on the temperature/frequency dependence of the scattering rate with earlier results. In the optimally doped Y123 and Bi2212 samples, microwave and infrared experiments demonstrated that $1/\tau(\omega \rightarrow 0)$ drops abruptly below the superconducting transition temperature. [Bonn92, Romero92] A suppression of the scattering rate in the super-

conducting state was confirmed through transport experiments. [Yu92] These results are consistent with the behavior of $1/\tau(\omega)$ plotted in Fig. 3.6.

In the underdoped regime, the suppression of the scattering rate occurs already in the normal state and thus a comparison can be made with dc resistivity data. In underdoped cuprates the resistivity is a linear function of T for $T > T^*$, but it shows a crossover to a steeper slope at $T < T^*$. [Ito93] Since dc resistivity is, within a constant factor, the zero frequency limit of $1/\tau(\omega)$, the crossover behavior could be completely accounted for by the low-frequency suppression of the scattering rate. We also note that the dc resistivity of underdoped cuprates, at least below 300 K, is determined by the charge dynamics in a relatively small energy range (below the threshold structure) while in the strongly overdoped cuprates, much larger energies are involved. It is not quite clear, however, how the $1/\tau(\omega)$ spectra in the underdoped cuprates will evolve above room temperatures where dc $\rho_{ab}(T)$ is still increasing with temperature. In particular, it is not clear whether the $1/\tau(\omega)$ will remain linear and temperature-independent at high frequencies.

3.4.2 Theoretical models for $1/\tau(\omega)$

There is yet to be a clearly superior theoretical explanation for the peculiar behavior of the infrared optical response presented in the previous section, but a few models deserve mentioning. We will start here with the models that rely on inelastic scattering processes as the mechanism that determines the frequency and temperature behavior of the real and imaginary parts of the memory function, and will continue with other models later.

As we have stressed previously, the modeling of the real part of $M(\omega)$ in terms of carrier-scattering only makes sense if there are reasons to believe that the optical response in the energy region under study is predominantly due to mobile carriers (no interband contribution) and that there is only one type of carrier participating in optical excitations (one-component model). It is not at all clear that these requirements are satisfied in the HTSC cuprates at all frequencies, particularly in the midinfrared range, where some of the interband transition processes may have energies comparable with those of the intraband excitations. The situation is complicated further by the fact that these contributions do not have characteristic sharp

features which would facilitate their separation. As an example, a typical frequency dependence of the room-temperature ab-plane complex memory function $M(\omega)$, in the functional form of $1/\tau(\omega)$ and $m^*(\omega)$, is shown in Fig. 3.9 on a large frequency scale for Y123 ($x = 6.95$) material ($E||a$). Evidence for the interband process comes from, for example, $m^*(\omega)$ being negative ¹ at $\omega > 8000 \text{ cm}^{-1}$.

Nevertheless, there are reasons to believe that the carrier-scattering approach can be used at frequencies below $2000\text{-}3000 \text{ cm}^{-1}$ where we have presented data in section 3.3. First, the conductivity is observed to be temperature dependent² at $\omega < 2000 - 3000 \text{ cm}^{-1}$, and it is natural to assign the temperature-dependent part to the "free" carrier contribution; Second, as it was noted earlier by Thomas *et al.*, [Thomas88] the number of carriers that one obtains using the sum rule analysis for the real part of optical conductivity is consistent with estimates from chemical valence arguments for the carrier density provided, the sum rule is taken up to about 8000 cm^{-1} .

Therefore the carrier-scattering mechanism is at least a plausible mechanism for the optical response in HTSC at frequencies less than $2000\text{-}3000 \text{ cm}^{-1}$. Below we will outline some approaches that are based on carrier-scattering mechanisms as well as some problems associated with them.

The first approach is electron-phonon scattering. [Shulga91] While this model qualitatively reproduces the gap-like depression in $1/\tau(\omega)$ at low temperatures (see, for example, calculations presented in Figs. A.1,A.2), it is not nearly as sharp as that seen in the experimental data. An even more severe problem is the absence of the predicted temperature dependence of $1/\tau(\omega)$ at high frequencies. A signature of the electron-phonon theories is their prediction of significant temperature-induced changes (proportional to $k_B T$ at high temperatures). Furthermore, as discussed in

¹Since an interband transition can be roughly modeled by an oscillator centered at ω_i , the imaginary part of the conductivity is negative below ω_i .

²Romero *et al.* proposed a somewhat similar way of differentiating the two contributions. [Romero92] They suggest that the response of conducting carriers completely collapses into a δ -function at $T \ll T_c$. Therefore, the spectrum of $\sigma_1(\omega)$ at $T \ll T_c$ represents the "midinfrared component" in the conductivity. While this approach appears to be useful under the circumstances and allows one to extract the temperature dependence of the scattering rate below T_c , it also has serious deficiencies. The most significant one stems from the fact that the conductivity in the superconducting state remains finite down to the lowest available frequencies and even increases in a Drude-like fashion at $\omega < 50 \text{ cm}^{-1}$ (Fig. 3.5).

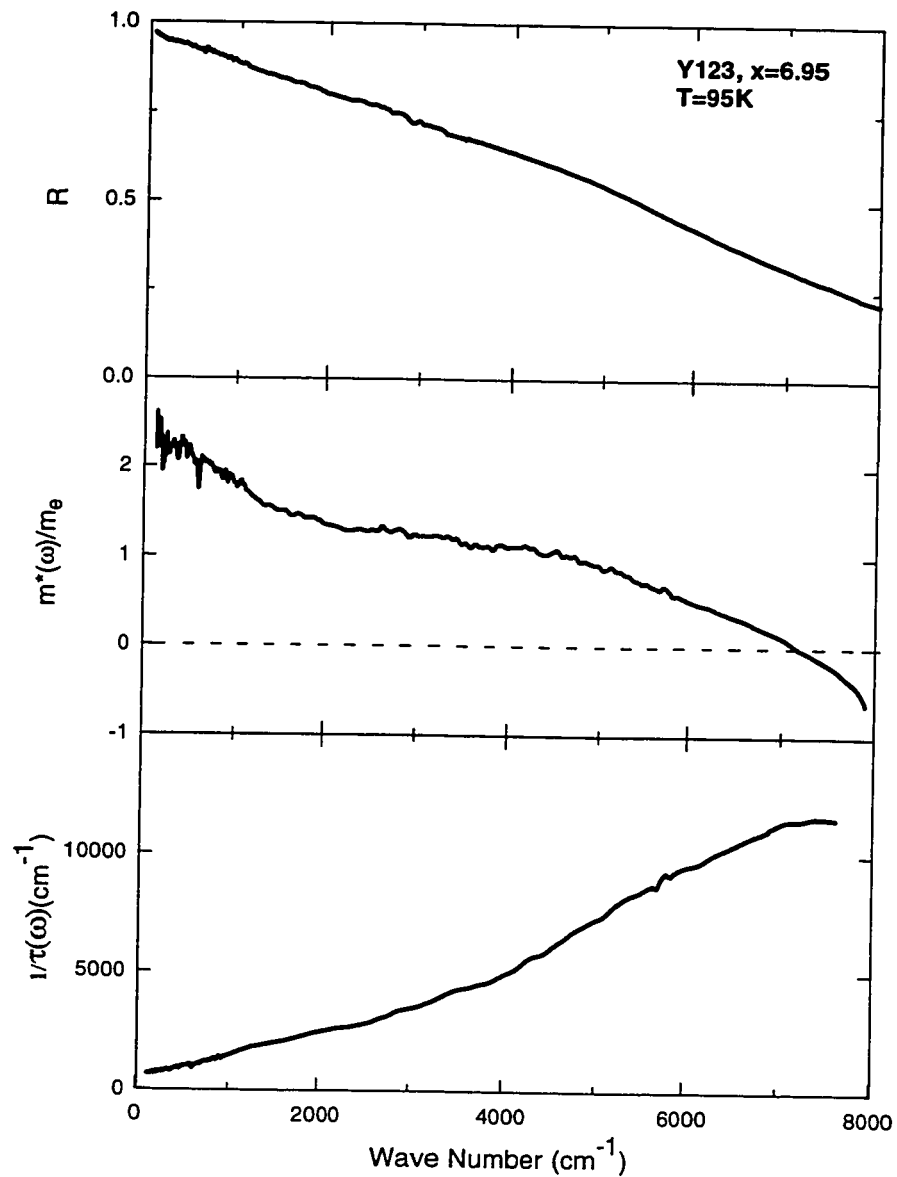


Figure 3.9: Optical response functions for optimally doped Y123, broad frequency range.

Results were obtained by D.N. Basov. The reflectivity R (top panel), the effective mass (middle panel), and the frequency dependent scattering rate (lower panel) for an optimally doped Y123 crystal are shown over a wide frequency range. Temperature is 90 K. The effective mass becomes negative for $\omega > 6000 \text{ cm}^{-1}$ suggesting a breakdown of the validity of the single-component approach due to onset of an interband transition.

Appendix A, within the electron-boson scattering scenario, the characteristic temperature below which a low-frequency depression in $1/\tau(\omega)$ occurs is determined by the high-energy cut-off of the bosonic spectrum $\mathcal{A}_{tr}(\Omega)$. The experimental fact is that the characteristic temperature in the cuprates, T^* , depends on the doping level. This is inconsistent with the electron-phonon scenario, since the phonon cut-off is doping-independent. Thus we believe that the electron-phonon scattering model fails to reproduce the essential features of the experimental data for underdoped cuprates.

It is still possible, however, that phonons play some role in the mechanism responsible for the experimentally observed behavior of $1/\tau(\omega)$, but in a more unconventional way. We note in this respect that the frequency scale in the spectra of $1/\tau(\omega)$ associated with the pseudogap state, which does not significantly change with doping, remarkably coincides with the high-frequency cut-off energy of the phonon density of states in HTSC. [Renker88]

More generally, a serious defect of all models that employ scattering of electrons by bosonic excitations to describe the optical response of underdoped HTSC is their failure to account for the observed behavior in the high-frequency part of $1/\tau(\omega)$ spectra. As discussed in section 3.3, underdoped cuprates do not show any temperature dependence in $1/\tau(\omega)$ at $\omega > 700 - 800 \text{ cm}^{-1}$. On the other hand, in Appendix A it was shown that scattering of electrons by any temperature-independent bosonic spectrum leads to a strong temperature dependence of $1/\tau(\omega)$ at high frequencies. The only way to get around this contradiction is to assume that the boson spectral function $\mathcal{A}_{tr}(\omega)$ is also a function of *temperature*: $\mathcal{A}_{tr}(\omega, T)$. In this case, if the absolute value of $\mathcal{A}_{tr}(\omega, T)$ scales properly with temperature, it may account for the observed temperature-independent scattering rate at high frequencies. The phonon density of states does not show any such changes. [Renker88]

One of the mechanisms that may yield a temperature-dependent $\mathcal{A}(\omega)$ function is the scattering of charge carriers on local fluctuations towards an antiferromagnetic order. The energy scale associated with spin fluctuations is measured [Bourges95] to be of the order of 50 meV. The features in the scattering rate spectra that we observe in the pseudogap state are on the same energy scale, supporting such models. This mechanism would also provide a qualitative explanation for the doping dependence of the pseudogap.

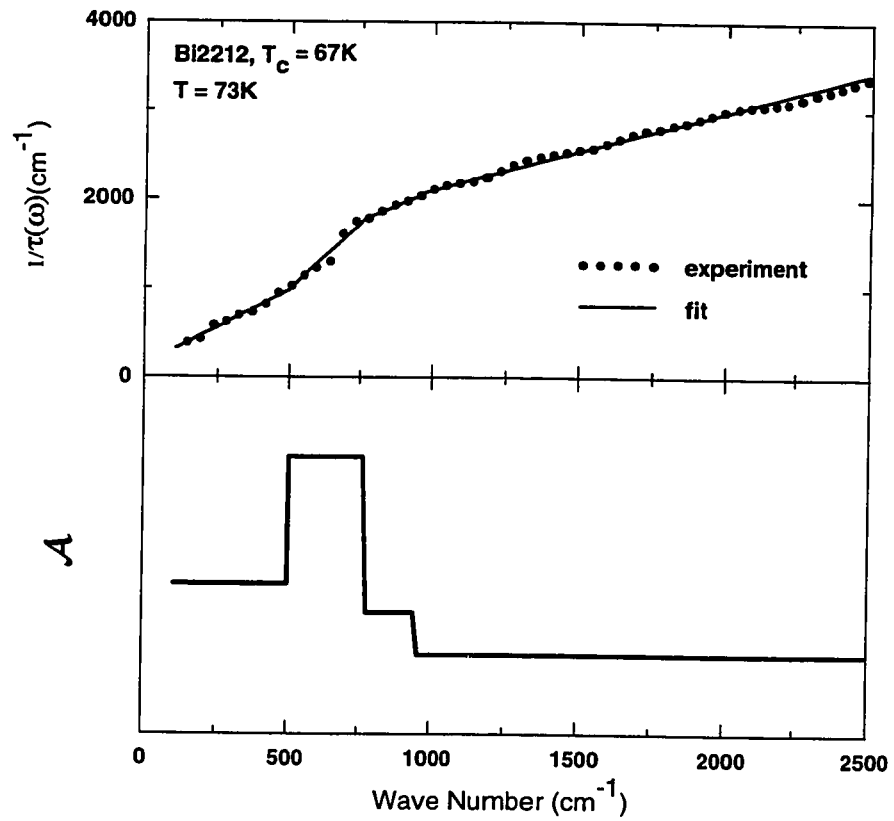


Figure 3.10: An estimated boson spectral density in the pseudogap state. Top panel: scattering rate above T_c in the pseudogap state is approximated by straight line segments. Bottom panel: slopes of the straight segments are plotted as a function of frequency.

Finally, we can roughly estimate the boson spectral function that is needed to obtain the threshold structure in $1/\tau(\omega)$ in the pseudogap state at $T < T^*$. This estimate can be obtained by inverting the lowest temperature normal-state experimental results for $1/\tau(\omega)$ using Allen's expression (Eq. A.14). The complete inversion formula can be written as $\mathcal{A}(\omega) = 1/\omega d/d\omega[\omega^2 d/d\omega(1/\tau(\omega))]$. [Marsiglio96] Since the process of numerical differentiating greatly amplifies the noise level of our spectra, we have chosen the following approach to minimize the added noise: The experimentally obtained $1/\tau(\omega)$ for underdoped Bi2212 was fitted with four straight lines, as shown in Fig. 3.10 and then the inversion formula was applied to the resulting artificial spectrum composed of the straight pieces. In this scheme, the exact inversion formula reduces to the first derivative, that is the slope of the straight lines. The resulting $\mathcal{A}_{tr}(\omega)$ spectrum is shown in the bottom panel of Fig. 3.10. Obviously the rather crude approximation of the experimental curve prevents us from observing any fine details of the spectrum. The significant result is, however, that an intense peak in $\mathcal{A}_{tr}(\omega)$ at 500-700 cm^{-1} , superimposed on a broad background, is needed to account for the behavior of the scattering rate in the pseudogap state if one adopts an electron-boson scattering model.

We note that at least some of the current electron-electron scattering models suffer from the same problems as the electron-boson ones. In particular, they cannot account for the weak or completely absent temperature dependence of $1/\tau(\omega)$ spectra in underdoped cuprates at high frequencies. In the conventional Fermi liquid theory, for example, the electron-electron scattering rate is proportional to $(\hbar\omega)^2 + (\pi k_B T)^2$, that is the frequency and temperature dependence of the scattering rate "mirror" one another. [Pines96] Another example of this type of mirroring is provided by the heavy fermion compound URu₂Si₂ [Bonn88] or the perovskite Sr₂RuO₄. [Katsufuji96] In both cases a scaling of $\hbar\omega = 2k_B T$ collapses the dc resistivity curve on the frequency dependent scattering rate curve. This is in contrast to the experimental observations in underdoped cuprates where a significant frequency dependence, but no temperature dependence, were observed at frequencies above 1000 cm^{-1} . Other Fermi-liquid type models, such as the nested Fermi-liquid (NFL) model or the marginal Fermi-liquid (MFL) model, also predict a significant temperature dependence at high frequencies. [Rieck95, Schmitt-Rink88] For example, the main assumption of the phenomenologi-

cal MFL model is that the scattering rate varies as $1/\tau(\omega, T) = \alpha\omega + \beta T$ where α and β are constants of the order of unity. It is clear that in the underdoped materials $1/\tau$ does not follow this behavior since $\beta = 0$, *i.e.* there is no temperature dependence associated with the linear in frequency scattering rate. As we have seen, a temperature dependence of the scattering rate does develop, except in optimally doped and overdoped materials.

We note that from a completely different point of view, the two component model of optical conductivity [Tanner92] in which the infrared conductivity is divided into a free-carrier and a midinfrared component, these observations imply that the mid infrared component is temperature independent in underdoped materials.

Some hints regarding the microscopic origin of the scattering mechanism in HTSC can be obtained from the analysis of impurity effects. For example, substituting 1.275% of the Cu atoms with Zn in Y124 completely destroys the pseudogap structure in $1/\tau(\omega)$ spectra, not only in the normal state but in the superconducting state as well. [Puchkov96d] The *c*-axis results obtained for a Y124 sample with 0.425 % Zn also reveal a *complete suppression* of the pseudogap. [Basov96] The effect of Zn on the *c*-axis pseudogap is similar to the one observed in the spin-lattice relaxation time $1/TT_1$. [Ishida93, Zheng93]

There are several other theoretical models that attempt to explain the pseudogap phenomenon from different assumptions.

The model due to Emery and Kivelson [Emery95b] predicts that the low carrier density in the underdoped regime may result in quasiparticle pairing without pair-pair coherence at temperatures well above the actual T_c , thus producing a pseudogap. As the temperature is lowered the phase coherence is established, leading to bulk superconductivity. This model would provide an explanation for the lack of dramatic changes upon crossing into the superconducting state, which is consistent with our optical experiments as well as ARPES measurements. However, it is not quite clear why the high-frequency onset energy of the optical pseudogap does not change as a function of doping while T^* and T_c do.

In the spin-charge separation picture, [Anderson87] spin singlets form at T^* , giving rise to a spin gap while the charge carriers (holons, which are bosons) Bose condense at the superconducting transition. [Fukuyama92, Kotliar88, Lee92, Rice92]

Other models invoke a spin density wave [Kampf90, Barzykin95] in the context of a normal Fermi liquid to form a gap in the spin excitations which are the predominant scatterers of the charge carriers.

3.4.3 The relation between *ab*-plane and *c*-axis pseudogap.

A comparison of *a*-axis results for Y123 materials with earlier *c*-axis data [Homes93b, Basov94] suggests that the pseudogap directly observed in the *c*-axis conductivity at $T < T^*$ is necessarily accompanied by a suppression of the in-plane $1/\tau(\omega)$ at low frequencies. Indeed, the threshold feature in $1/\tau_a(\omega)$ is found in underdoped crystals at $T < T^*$ *only* when the spectrum of $\sigma_c(\omega)$ exhibits a pseudogap. The suppression of the pseudogap in $\sigma_c(\omega)$, either by an increase of temperature above T^* , or by an increase of the carrier density from $x=6.6$ to $x=6.95$ in Y123, or by the substitution of Cu with Zn in underdoped Y124, [Basov96] restores the nearly-linear frequency dependence of the in-plane scattering rate. Therefore, we conclude that the same microscopic mechanism leads to the opening of the pseudogap in the interplane response *and* the low-frequency anomalies in the lifetime effects within the CuO_2 planes.

3.4.4 The superconducting state

One of the most striking features is how closely the $1/\tau$ curves for the underdoped cuprates in the superconducting state resemble those in the pseudogap state. It is useful to compare the energy scales for the various experiments that reveal the presence of a pseudogap.

The maximum gap seen in ARPES experiment is about $2\Delta = 360 \text{ cm}^{-1}$ (45 meV) whereas the *c*-axis conductivity (in YBCO) shows an onset at $\sim 200 \text{ cm}^{-1}$ (25 meV) rising to a plateau at 360 cm^{-1} (45 meV). The *ab* plane $1/\tau$ scale is considerably higher with the steepest part of the curve at $\sim 500 \text{ cm}^{-1}$ (62 meV) merging with the high frequency linear curve around 750 cm^{-1} (93 meV) in all of the materials studied. Another high energy scale is the depression of the *c*-axis conductivity at the superconducting transition — of the order of or larger than 600 cm^{-1} .

Thus it appears to us that the energy scales associated with the pseudogap and

with the superconducting state are distinct: the pseudogap has a smaller magnitude and is gradually destroyed by doping. In Y124 crystals with Zn substitution, superconductivity persists while the pseudogap is suppressed. [Puchkov96d] We also note that in all samples we find finite absorption extending down to the lowest frequencies. In an *s*-wave superconductivity scenario, this absorption implies a very anisotropic superconducting gap. As for the *d*-wave gap models, our data may be consistent with the theoretical predictions [Carbotte95, Jiang96, Quinlan96] only if one assumes a significant amount of impurities present in the crystals. This assumption is, however, inconsistent with the linear penetration depth observed in the high quality YBCO crystals used in this work. [Hardy93, Zhang94]

Although changes in $1/\tau(\omega)$ upon crossing into the superconducting regime in the optimally doped cuprates are apparently dramatic, it may simply be due to the simultaneous formation of the pseudogap and superconducting condensate. Also, as noted above, it is only in the *c*-axis conductivity where we see evidence of a larger energy scale associated with the superconducting state. [Basov94]

In the superconducting state, the spectra of the effective mass are remarkably similar in all crystals we have studied. As noted in Appendix A, the zero frequency extrapolation of the effective mass gives a square of a ratio of the total plasma frequency, ω_p , to the plasma frequency of the superconducting condensate, ω_{ps} . This value is in good agreement with the results obtained directly from the use of the sum rule analysis of $\sigma_1(\omega)$ or from an analysis of the imaginary part of the conductivity. The fact that the zero-frequency extrapolations of the effective mass are roughly the same, $m^*(\omega \rightarrow 0) \simeq 3.5 - 4$, for all underdoped materials suggests that the superfluid condensate density scales with the total carrier density in the underdoped cuprates. Therefore, we conclude that there are no pair-breaking effects in the pseudogap state. However, as doping is increased above optimal, the mass enhancement becomes weaker, which indicates a decrease in the superfluid density. This behavior is in agreement with the earlier μ SR results. [Uemura89, Uemura91, Niedermayer93]

3.4.5 Open questions

At the time of writing this thesis, there remain many open questions. The first question that must be addressed is whether or not the pseudogap state is generic

among all high- T_c materials.

It has been suggested that the pseudogap is a manifestation of interlayer coupling and is specific to the double layer materials such as YBCO and Bi2212. [Millis90] Support for this view comes from NMR measurements, which show a rather weak depression of magnetic susceptibility in La214 in the temperature range where the transport data show evidence of a strong suppression of scattering. As we have seen from our presentation of the data for overdoped single-plane Tl2201 samples, the ab -plane $1/\tau(\omega)$ curves look similar to those of the two-plane materials *in the superconducting state*.

Experimental optical data exists for the one plane La214 material [Gao93, Uchida96, Startseva] which, in the underdoped regime, shows a very strong depression in $1/\tau(\omega)$ at low temperatures which is consistent with the pseudogap picture. However, one must be cautious at this stage since the data from various laboratories show considerable variation in the magnitude of the effect. In some cases, the structure in reflectivity is so strong that it produces an unphysical singularity in the $1/\tau(\omega)$ curves. [Uchida96] More work on a range of samples must be done for this system. Similar strong features are seen in the electron-doped $\text{Nd}_{2-x}\text{Ce}_x\text{CuO}_4$ material. [Startseva]

It has been suggested that the one-component model of charge transport in the cuprates is particularly unsuited for the La214 system where, at least at low doping levels, $\sigma(\omega)$ shows a separate midinfrared band [Cooper94] rather than a smooth free-carrier band with excess conductivity at high frequencies. It is also known that at very low doping levels, in the insulating state, there is a separate band or several bands [Perkins93, Thomas91] and a one component picture is clearly inappropriate.

Another important effect that needs to be examined is the role of impurities. It was shown, [Puchkov96d] that Zn has the effect of destroying the pseudogap in Y124, both in the c -axis $\sigma_1(\omega)$ and in the ab -plane $1/\tau(\omega)$. Since Zn is an impurity that has a strong effect on T_c , a systematic study of the influence of Zn may help us to isolate its effect on T^* , the onset of the pseudogap phase, and T_c , the onset of superconductivity.

Phonons play an important, if perhaps subsidiary, role in high temperature superconductivity. As is shown in Appendix A, the standard electron-phonon mecha-

nism predicts a temperature dependent $1/\tau(\omega)$ at all frequencies whereas the observations in the pseudogap state show a temperature independent high-frequency $1/\tau(\omega)$. On the other hand, the frequency range of the steepest rise of $1/\tau(\omega)$ falls in the oxygen mode region of the phonon spectrum and seems to vary little with temperature, chemical composition or doping. This inertness of the pseudogap frequency suggests that phonons may be involved in some indirect way.

One process that affects the *ab*-plane conductivity in all high- T_c materials is the coupling of the *ab*-plane electrodynamic response to *c*-axis LO phonons. [Reedyk92, Timusk91, Kostur96] To separate this process from other processes, it is necessary to measure the in-plane optical response on the *ac* face of an underdoped crystal where the LO_c coupled structure vanishes. [Reedyk92]

The signature of the pseudogap state of YBCO materials is that the in-plane conductivity is enhanced whereas the interplane conductivity is suppressed. It is important to find out whether this is manifested by other cuprates.

3.5 Conclusions

We see that there is a universal depression of the real part of the memory function $M'(\omega)$, or $1/\tau(\omega)$, below an energy of the order of 700-800 cm^{-1} in all underdoped materials below a characteristic temperature T^* . At the optimal doping level $T_c \simeq T^*$ and in the strongly overdoped regime the gap-like depression is not seen. While the high-frequency $1/\tau(\omega)$ was found to be temperature-independent in the underdoped cuprates, an obvious temperature dependence is seen in the strongly overdoped cuprates. We believe that these optical results add to the growing evidence for the existence of a normal state pseudogap in the physical response function of the underdoped HTSC.

While intense theoretical work has been done to explain the observed phenomenon, none of it has been completely successful. It is necessary for any theoretical model to explain not only the formation of the gap in the *ab*-plane response, but also a wealth of phenomena, such as the *c*-axis transport and the remarkable temperature dependencies that are observed, both for the *c*-axis pseudogap as well as the *ab*-plane response.

Chapter 4

The non-cuprate high- T_c superconductor $\text{Ba}_{1-x}\text{K}_x\text{BiO}_3$

4.1 Introduction

$\text{Ba}_{1-x}\text{K}_x\text{BiO}_3$ or BKBO (as well as $\text{BaPb}_x\text{Bi}_{1-x}\text{O}_3$ or BPBO) is a family of superconductors based on the perovskite BaBiO_3 . Superconductivity in this compound was discovered by Mattheiss, Gyorgy, and Johnson in 1988 [Mattheiss88] and since then BKBO has attracted a great deal of attention because of a combination of high T_c values with a relatively simple isotropic structure (cubic perovskite in the metallic phase [Pei90], see Fig. 4.1), and lack of Cu. Nevertheless, just as in the copper based HTSC materials, normal state properties, their doping dependence, and the mechanism of superconductivity in BKBO are far from being understood.

Despite its relatively low — 31 K — superconducting transition temperature, there are several reasons to place BKBO in the same group of high-temperature superconductors as the cuprates: 1) As was first pointed out by Batlogg [Batlogg89], the value of T_c is exceptionally high in relation to an extremely low density of states $N(0)$ at the Fermi level (see Fig. 1.6). This is an extremely unfavorable situation for the phonon-mediated BCS mechanism and yet BKBO has a higher T_c than any other known copper-free material, except for C_{60} . This puts into question the application of the BCS model with electron-phonon mediated coupling for BKBO but is in agreement with the general trend in all high- T_c superconductors: large T_c despite of low $N(0)$. 2) The maximum T_c was observed near the insulator-metal (IM)

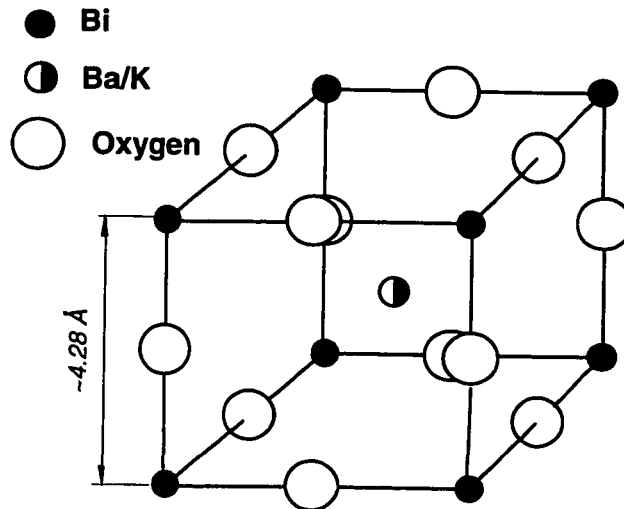


Figure 4.1: The crystal structure of BKBO in the metallic doping regime.

transition followed by a decrease in T_c with overdoping — another signature of high temperature superconductivity. 3) The normal-state optical conductivity of metallic BKBO shows similar MIR absorption features as in the cuprate superconductors. 4) Other similarities have been observed in tunneling, μ SR, and optical experiments. [Sharifi91, Uemura91, Bosovic92]

There are some differences as well. We will list only the main ones: 1) The undoped component BaBiO_3 is diamagnetic. [Cava89] 2) The charge carriers are electrons [Sato89, Affronte93] while in all copper oxide superconductors (except for $(\text{Nd,Ce})_2\text{CuO}_4$) they are holes. 3) There is a well defined onset of a superconducting gap in BKBO [Schlesinger89, Dunmore95, Sato90, Sharifi91, Zasadzinski89, Sato93], while in the cuprates this issue is still an open one. [Timusk89, Tanner92, Orenstein90] 4) The isotope shift was reported to be 0.2-0.4 [Batlogg88, Hinks88, Loong91] in contrast with much smaller values for the cuprates.

It is still not understood why undoped BaBiO_3 , which has one electron per Bi atom and therefore should be a metal with a half-filled conduction band, is in fact an insulator. The nature of the insulator-metal (IM) transition at the doping level $x_c \simeq 0.35$ is also a mystery and the focus of intensive experimental work. Recently,

we have performed reflectivity measurements on non-metallic BKBO single crystals at a doping level just below the IM boundary. A peculiar temperature dependence observed was interpreted as evidence for bipolaron formation in non-metallic BKBO. The results were published in the Physical Review B. [Puchkov95c] In a subsequent paper, [Puchkov96b] we used the large amount of the experimental data on BKBO, accumulated to date, to extend these arguments to the whole doping range of BKBO.

Previous optical studies of superconductivity in BKBO have been done mainly on thin films. [Schlesinger89, Blanton93, Sato93] Although ratios of reflectivities in the superconducting and normal states have been obtained for the thin films [Schlesinger89, Sato93], in none of the above experiments were absolute low-temperature reflectivity measurements performed. Recently, absolute reflectance results in the normal and the superconducting states were obtained on single crystals of BKBO, but only at one doping level. [Puchkov95a] As a result, the detailed behavior of the optical conductivity as a function of doping still needs to be clarified. We contributed to the this effort by performing reflectivity and ellipsometric measurements in a combined range of 30-50000 cm^{-1} on three superconducting BKBO single crystals (T_c 's=21 K,28 K,31 K) at temperatures ranging from $T = T_c/3$ to $T = 300$ K.

Both papers are reproduced in this thesis in a complete form with the permission of the American Physical Society.

4.2 Optical conductivity of non-metallic $\text{Ba}_{0.69}\text{K}_{0.31}\text{BiO}_3$ single crystals: Evidence for bipolaron formation.

In this paper we present the experimental optical data obtained on non-metallic single crystals of $\text{Ba}_{0.69}\text{K}_{0.31}\text{BiO}_3$. We interpret the results as evidence for bipolaron formation in this material.

Optical conductivity of nonmetallic $\text{Ba}_{0.69}\text{K}_{0.31}\text{BiO}_3$ single crystals: Evidence for bipolaron formation

A.V. Puchkov and T. Timusk

Department of Physics and Astronomy, McMaster University, Hamilton, Ontario, Canada L8S 4M1

M.A. Karlow and S.L. Cooper

*Department of Physics and Material Research Laboratory, University of Illinois at Urbana-Champaign,
104 South Goodwin Avenue, Urbana, Illinois 61801*

P.D. Han and D.A. Payne

*Department of Material Science and Engineering and Material Research Laboratory, University of Illinois at Urbana-Champaign,
104 South Goodwin Avenue, Urbana, Illinois 61801*

(Received 16 June 1995)

We report the far-infrared to near-ultraviolet reflectivity and ellipsometric measurements on an insulating $\text{Ba}_{1-x}\text{K}_x\text{BiO}_3$ single crystal, with a doping level $x=0.31$ just below the insulator-metal transition boundary. The optical conductivity was calculated using Kramers-Kronig analysis. We examine the experimental data in terms of a small bipolaron model. This model, with no free parameters, allows us to obtain a satisfactory agreement with our experimental results, including the overall shape and the peculiar temperature dependence of the optical conductivity. The same model provides a qualitative explanation for some aspects of the transport-measurement results reported previously.

During the last few years much work has been done, including optical studies,^{1,2} on the nature of the insulating state and insulator to metal (IM) transition in the $\text{Ba}_{1-x}\text{K}_x\text{BiO}_3$ (BKBO) system. The most popular point of view is that the undoped BaBiO_3 , which has one electron per Bi atom, is made insulating by frozen breathing mode distortions. These distortions effectively double the unit cell and may open a gap in the middle of the initially half-filled conduction band of BaBiO_3 . Results of band structure calculations indicate that the experimentally measured values of the breathing mode distortion can indeed induce a direct gap at the Brillouin zone (BZ) boundary. However, these distortions are not large enough to produce a real gap in the density of states,³ which has led to the conclusion that the strong correlation effects of the Bi 6^s electrons should be taken into account.

We have performed reflectivity measurements on insulating $\text{Ba}_{0.69}\text{K}_{0.31}\text{BiO}_3$ which is just below the IM transition. Unlike previous optical measurements on the insulating members of the BKBO family we have performed reflectivity measurements in a frequency range down to 25 cm^{-1} and at temperatures ranging from $T=35$ to 300 K . This and the combination of the reflectivity and ellipsometric measurements used in our study allowed us to obtain accurate data that may be helpful in understanding the peculiar properties of BKBO in the insulating state and at the IM transition boundary.

The $\text{Ba}_{0.69}\text{K}_{0.31}\text{BiO}_3$ single crystal was grown by an electrochemical method.⁴ The lattice parameters were measured by x-ray diffraction using a Rigaku D-max diffractometer (Cu $K\alpha$, $\lambda = 1.5405\text{ \AA}$). After the optical measurements, the crystal was ground into powder and x-ray diffraction measurements were carried out on the powdered sample intermixed with high-purity Ge powder which acted as an internal

x-ray standard. The lattice parameters were refined by a least-square fit routine with calibration against Ge. The potassium concentration x was estimated from the linear relationship between pseudocubic lattice parameter a and potassium concentration x .⁵

For the optical measurements, one of the sample's faces was mechanically polished with a $1\text{-}\mu$ abrasive. Reflectivity measurements were performed in the frequency range $25\text{--}40\,000\text{ cm}^{-1}$ using the procedure described previously.⁶ The optical conductivity was calculated by Kramers-Kronig analysis of the reflectivity spectra, approximating the reflectivity below 25 cm^{-1} by a Hagen-Rubens formula at $T=300$ and 200 K and by a constant at the lower temperatures. Ellipsometric measurements were performed on the same crystal at frequencies from $10\,000$ to $50\,000\text{ cm}^{-1}$, and the high-frequency reflectivity approximation was chosen in such a way that the calculated optical conductivity was in agreement with the direct ellipsometric results.

The reflectivity results presented on the upper panel of Fig. 1(a) are unusual. As temperature is reduced from 300 to 120 K the reflectivity spectrum changes dramatically from one typical of a (poor) conductor to that of a typical insulator. Reflectivity changes with temperature at frequencies up to at least 8000 cm^{-1} ($=11\,600\text{ K}$) and perhaps even higher. While reflectivity changes rapidly at temperatures from 300 down to 120 K , below 120 K no temperature dependence was observed. As a result, reflectivity spectra at $T=120\text{ K}$ and $T=35\text{ K}$ almost coincide except for some phonon sharpening. This resembles the temperature dependence at mid-infrared frequencies seen in our previous study on a $T_c=31\text{ K}$ sample.⁶

The real part of the optical conductivity is shown in Fig. 1(b) and in Fig. 2. The inset of Fig. 2 shows that the high-

⁰Reprinted from Phys. Rev. B, p. R9855 (1995). ©1995 The American Physical Society.

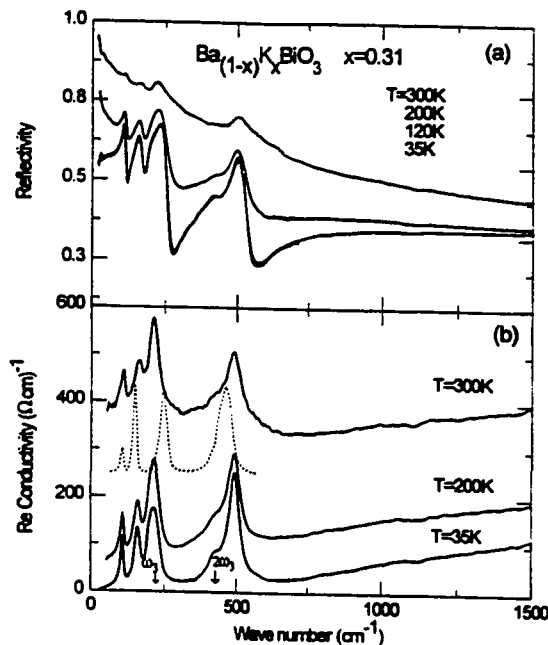


FIG. 1. (a) The experimentally obtained reflectivity spectra at different temperatures. Note that $T=120$ and $T=35$ K spectra almost coincide. (b) The $\sigma_1(\omega, T)$ spectra calculated from the reflectivity results using the Kramers-Kronig analysis. Phonon spectrum in BaBiO_3 [offset by $240 (\Omega \text{ cm})^{-1}$] is presented by the thin dashed line.

frequency optical conductivity, obtained from Kramers-Kronig analysis of the reflectivity, is in excellent agreement with the ellipsometric results. Reliable results for the low-temperature $\sigma_1(\omega)$ were obtained up to about 0.8 eV, limited by the high-frequency limit of our low-temperature measurements.

First we will concentrate on room-temperature results. The optical conductivity clearly does *not* show the narrow Drude-like free-carrier part that was observed in the metallic superconducting samples.⁶ This indicates that the IM transition is directly associated with the appearance of this free-carrier Drude component. The fact that the material becomes a superconductor with $T_c = T_c^{\text{max}} = 31$ K as soon as the K doping is high enough for the Drude component to appear strongly supports the suggestion made previously⁶ that the charge carriers responsible for the midinfrared component do not directly participate in the superconductivity. Only the itinerant metallic carriers responsible for the Drude component contribute to the superconducting current at $T < T_c$. The incoherent [mean-free path $l \approx 6-7 \text{ \AA}$ (Ref. 6)] compared with the cubic lattice parameter $a = 4.3 \text{ \AA}$] midinfrared carriers remain normal, thus accounting for the finite absorption below the superconducting gap frequency observed in the optical experiments.^{6,7}

To compare the phonon spectra of $\text{Ba}_{0.69}\text{K}_{0.31}\text{BiO}_3$ with that of the undoped BaBiO_3 we have plotted the phonon spectrum of BaBiO_3 (Ref. 8) using a thin-dashed line in Fig. 1(b). The same four modes are present in both materials but

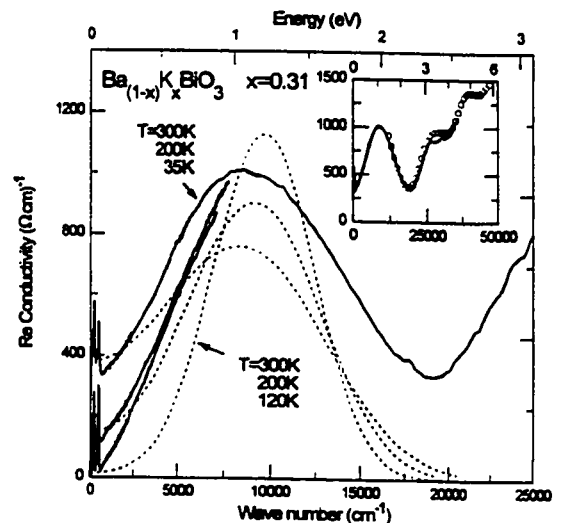


FIG. 2. The experimental optical conductivity spectra at several temperatures (solid lines). The $\sigma_1(\omega, T)$ spectra calculated using Eqs. (1) and (2) and parameters in text (dashed lines). The inset: the optical conductivity at $T=300$ K calculated using the KK analysis which includes high- and low-frequency reflectivity approximations (solid line) and obtained from the direct ellipsometric measurements (open circles).

at somewhat different frequencies. The frequency of the lowest mode does not change significantly with increasing x and the frequencies of the second and fourth modes move up indicating an increase in their stiffness. Only the third mode shows some softening with frequency reducing from about 245 cm^{-1} at $x=0$ down to 214 cm^{-1} at $x=0.31$ which may be an indication of stronger electron-phonon coupling for this mode.

We now focus on the temperature dependence of the reflectivity and the optical conductivity. This dependence cannot be understood in terms of a simple rigid band model with a temperature-independent electronic band structure. First, as we mentioned before, the temperature dependence occurs in the energy range $\hbar\omega \geq 1 \text{ eV} = 11604 \text{ K}$ which is much higher than the experimental temperatures. Second, the rapid temperature dependence above $T^* = 120-150 \text{ K}$ changes to almost no temperature dependence below T^* .

It should be noted that features at the characteristic temperature T^* can be seen in other transport experiments as well. The dc resistivity $\rho_{\text{dc}}(T)$ changes behavior at about this temperature in both the highly doped (near the IM transition) insulating samples and some of the metallic samples.^{9,10} Variable-range hopping (VRH) behavior with $\rho_{\text{dc}}(T) \sim \exp[-(T_0/T)^{1/4}]$ where $T_0 = 3-5 \times 10^8 \text{ K}$ has been reported for the low-doped insulating samples.⁹ The Hall coefficient^{9,11} and the V-shaped linear background in the tunneling measurements on the metallic samples also show changes in temperature dependence at $T = T^*$,¹² being temperature independent below T^* .

In the rest of the paper we will show that the results of our experiment, as well as the features at T^* in the transport

experiments pointed out above, can be understood at least qualitatively in the framework of a polaronic model. A polaron is a quasiparticle composed of a carrier self-trapped by its own interaction with a lattice taken together with the pattern of atomic displacements that produces the self-trapping. There are two types of polarons: large polarons (LP) where the carrier is spread over several lattice sites and small polarons (SP) involving a single site.¹³ It was found in Ref. 13 that LP and SP systems have qualitatively different absorption spectra. Comparing these results with the observed $\sigma_1(\omega)$ we conclude that if a polaronic model is to be used for BKBO it should involve *small* polarons. Because no isolated spins have been observed at doping levels close to $x=0.3$,¹⁴ a bipolaronic model with two electrons self-trapped in a singlet at the Bi sites must be utilized. As a result of the bipolaron formation, charge disproportionation should occur giving, in the extreme case, alternating $\text{Bi}^{+3}=(\text{Bi}^{+5}+2e^-)$ and Bi^{+5} configurations. Unfortunately, although the optical conductivity of a polaronic system has been described in detail,^{15,16} bipolaronic models have attracted much less attention. As a result, although the bipolaron absorption has been described qualitatively,¹³ detailed formulas for $\sigma_1(\omega)$ are not available at this time.

The absorption process of a small polaron is one in which a self-trapped carrier is excited from its localized state to a localized state at a site adjacent to the original site. The small polaron optical conductivity can be described by the equation:¹⁵

$$\sigma_1(\omega, T) = \sigma_1(0, T) \frac{\sinh(4E_b \hbar \omega / \Delta^2)}{4E_b \hbar \omega / \Delta^2} \exp[-(\hbar \omega)^2 / \Delta^2], \quad (1)$$

$$\Delta = 2\sqrt{2E_b E_{\text{vib}}}$$

where E_b is the small polaron binding energy, $\sigma_1(0, T) = 1/\rho_{\text{dc}}(T)$ is the dc conductivity, and Δ is a broadening factor indicating by how much the localized levels, between which the transition occurs, are broadened by the atomic vibration with the characteristic energy E_{vib} . At low temperature E_{vib} is just the zero-point vibrational energy $\hbar \omega_{\text{ph}}/2$. At temperatures high enough for the vibrational motion to be treated classically, $E_{\text{vib}} = k_B T$. For sufficiently strong electron-lattice coupling the small polaron absorption is peaked at $\hbar \omega = 2E_b$.

The dc conductivity $\sigma_1(0, T)$ is given by:¹⁵

$$\sigma_1(0, T) = J^2 n_c \frac{e^2}{\hbar} a^2 \sqrt{\pi} \frac{16E_b}{\Delta^3} \exp\left(-\frac{4E_b^2}{\Delta^2}\right)$$

$$= 1.08 \times 10^5 J^2 \frac{E_b}{\Delta^3} \exp\left(-\frac{4E_b^2}{\Delta^2}\right) [\Omega \text{ cm}]^{-1}, \quad (2)$$

where J is the electronic transfer energy, $n_c = 8.5 \times 10^{21} \text{ cm}^{-3}$ is the carrier concentration (assuming one electron per Bi atom) and $a = 4.3 \times 10^{-8} \text{ cm}$ is the lattice constant.

The absorption process for a small bipolaron is one where the two electrons of the bipolaron are separated from one another; one remains on the initial site while the second is transferred to an undeformed neighboring site. The absorption spectra of small bipolarons are similar to those of small polarons with the following modifications.^{13,17} The peak energy of the absorption is $2E_b' = 4E_b - U$, where $U \leq 2E_b$ is a

Coulomb energy associated with two carriers being on the same site. In addition, having two carriers on the same site doubles the uncertainty of the electronic energy, arising from the atomic vibrations about the equilibrium positions. That is, the broadening of the corresponding absorption peak doubles. If one takes these semiempirical modifications into account, Eqs. (1) and (2) can be used to describe, at least qualitatively, the small bipolaron absorption process provided that the substitutions $2E_b \rightarrow 2E_b' = 4E_b - U$ and $\Delta \rightarrow \Delta' = 4\sqrt{2E_{\text{vib}}E_b'}$ are made.

In the low-temperature limit, the optical conductivity of a (bi)polaronic system does not show temperature dependence ($E_{\text{vib}} = \hbar \omega_{\text{ph}}/2$ is temperature independent) while extra peaks may appear at frequencies equal to multiples of the phonon energies.^{15,16} This is a consequence of the fact that if the photon energy $\hbar \omega$ is not a multiple of a phonon energy $\hbar \omega_{\text{ph}}$, especially in the weak-dispersion phonon limit, processes involving both the absorption and emission of a large number of phonons may be required in order to conserve energy in a hop between sites. In the low-temperature limit such processes will have much smaller jump rates compared to the rates when $\hbar \omega / \hbar \omega_{\text{ph}}$ is an integer. Indeed, as can be seen in Fig. 1(b), as temperature is lowered, an additional feature appears in the optical conductivity spectrum with a frequency double that of the third phonon mode, $\hbar \omega = 2\hbar \omega_3 = 428 \text{ cm}^{-1}$. We note that this phonon mode is the one that demonstrates softening with increasing K-doping level. No other additional features have been observed to appear with decreasing temperature which may be due to either stronger dispersion of the other phonons or their relative unimportance for the bipolaronic excitations. If one considers the mode at $\hbar \omega_3 = 214 \text{ cm}^{-1}$ to be the main contributor to the bipolaron formation then the characteristic temperature of the crossover into the low-temperature regime T^* can be estimated as $T^* = \hbar \omega_3 / 2k_B \approx 150 \text{ K}$ in good agreement with $T^* \approx 120 \text{ K}$ found in our experiment.

We start by using Eq. (1) to describe the optical conductivity at $T=300 \text{ K}$. From Fig. 1(b) we obtain $\sigma_1(0, 300 \text{ K}) \approx 380 (\Omega \text{ cm})^{-1}$. Taking the high-temperature limit $E_{\text{vib}} = k_B T$ we have only one parameter E_b' left and it is completely determined by the position of the absorption maximum to be $E_b' \approx 5200 \text{ cm}^{-1}$. The calculated $\sigma_1(\omega, 300 \text{ K})$ is shown in Fig. 2 by the dashed line. Having determined E_b' we can estimate $J = 1775 \text{ cm}^{-1} = 220 \text{ meV}$. Using this J value we can determine $\sigma_1(0, 200 \text{ K}) \approx 147 (\Omega \text{ cm})^{-1}$ and calculate $\sigma_1(\omega, 200 \text{ K})$ for this temperature using Eq. (1). The $\sigma_1(\omega, 200 \text{ K})$ thus calculated is presented in Fig. 2. The optical conductivity at temperatures $T = 35$ and 120 K should be considered to be in the low-temperature limit. In this case we substitute for E_{vib} the zero-point motion energy $\hbar \omega_{\text{ph}}/2 = k_B T^* = 83 \text{ cm}^{-1}$. Using $\sigma_1(0, 120 \text{ K}) \approx 14 (\Omega \text{ cm})^{-1}$ we calculate $\sigma_1(\omega, 120 \text{ K})$ which is shown in Fig. 2.

One can see that even this oversimplified analysis with no free parameters gives a reasonable description of the overall shape and the temperature dependence of the optical conductivity observed experimentally. On the high-frequency side, agreement with the experimental results can be improved by including in our analysis the high-frequency interband transition seen in Fig. 2. On the low-frequency side the main

difference is that while the calculated $\sigma_1(\omega)$ has an exponential frequency dependence, the experimental $\sigma_1(\omega)$ is almost linear in frequency. Disorder is an additional system complication which may be included. A distribution of local fields generally replaces a single absorption band by a distribution of absorption bands whose centroids are displaced from one another. In this manner, disorder due to the mixture of K and Ba ions will broaden small bipolaron absorption. Different disorder models would yield different distributions of the peak's centroids.¹⁷

Small (bi)polarons are generally hard to form in the presence of only short-range interaction. A fair amount of a "stabilizing" long-range (Fröhlich) electron-phonon interaction makes the small (bi)polaron formation much easier. The long-range electron-phonon interaction with $\lambda \leq 0.35$ (Refs. 6, 14, 18) reported for the superconducting phase of BKBO may serve this purpose. It is interesting that some models of high-temperature superconductivity in the cuprate materials involve short-range next-neighbor interactions as well, for example, the *d*-wave model¹⁹ where the interaction is taken to be mediated by the local magnetic moments. One can speculate that a short-range electron-mediator-electron interaction might be the common feature for the mechanism of high-temperature superconductivity in the cuprates and BKBO system.

Recently, an explanation of the temperature and voltage dependence of the V-shaped tunneling background in terms of bipolaron (negative-*U* two-particle state) formation has been suggested.¹² Bipolaronic models have been discussed for this material based on the results of Raman-scattering measurements²⁰ and room-temperature optical absorption measurements performed on powdered samples.²¹ The temperature dependence of the dc resistivity in a disordered polaronic system can be easily mistaken for variable range hopping behavior. The exceptionally high values of $T_0 \sim 10^8$ K obtained in Ref. 9 supports this hypothesis. Namely, an estimate of the localization length *d* from the equation $k_b T_0 \approx 16[N(E_F)d^3]^{-1}$ using density of states $N(E_F)$

$\sim 10^{21} \text{ (cm eV)}^{-1}$ and $T_0 = 10^8$ K gives $d \approx 1.2 \text{ \AA}$, smaller than the interatomic distance. The polaronic model allows explanation for the large values of T_0 .²²

Finally we note that although the bipolaronic model used in this study allowed us to explain both the shape and temperature dependence of $\sigma_1(\omega, T)$ for $\text{Ba}_{0.69}\text{K}_{0.31}\text{BiO}_3$, the absorption peak in the undoped BaBiO_3 is too narrow by a factor of two to be described by Eqs. (1) and (2). There are several possible reasons for this discrepancy: (i) The real CDW order accompanied by the frozen breathing-mode distortions, which were observed experimentally at low *x*,⁵ may modify the simple model presented in this work; (ii) Our choice of the bipolaronic model was based on the experimental fact that no isolated spin is present at doping level $x = 0.31$. However, it was reported at least for $\text{BaPb}_{1-x}\text{Bi}_x\text{O}_3$ that with decreasing *x*, the paramagnetic part χ_{para} of the total magnetic susceptibility χ_{tot} is rising, making BaBiO_3 more paramagnetic than the metallic material.²³ Therefore, our choice of the bipolaronic model may be inappropriate for BaBiO_3 .

Summarizing, we have performed reflectivity and ellipsometric measurements on the nonmetallic member of the BKBO family $\text{Ba}_{0.69}\text{K}_{0.31}\text{BiO}_3$ in a frequency range from the far infrared to the near ultraviolet. The optical conductivity has been calculated using a combination of Kramers-Kronig analysis of the reflectivity spectra and direct ellipsometric results. Analysis of the experimental results in terms of a small bipolaron model allowed us to explain both the shape and peculiar temperature dependence of the optical conductivity as well as qualitative behavior of some other transport properties.

We would like to thank David Emin for many helpful discussions. This research was supported in part by the National Science and Engineering Research Council of Canada and by the Canadian Institute of Advanced Research. Research in the University of Illinois at Urbana-Champaign was sponsored by Contract No. NSF DMR 91-20000.

-
- ¹S. N. Blanton *et al.*, Phys. Rev. B **47**, 996 (1993).
²M. A. Karlow, S. L. Cooper, A. L. Kotz, M. V. Klein, P. D. Han, and D. A. Payne, Phys. Rev. B **48**, 6499 (1993).
³Katsuhiko Takegahara, J. Electron Spectrosc. Relat. Phenom. **66**, 303 (1994).
⁴P. D. Han, L. Chang, and D. A. Payne, J. Cryst. Growth **128**, 798 (1993).
⁵S. Pei *et al.*, Phys. Rev. B **41**, 4126 (1990).
⁶A. V. Puchkov, T. Timusk, W. D. Mosley, and R. N. Shelton, Phys. Rev. B **50**, 4144 (1995).
⁷D. Miller *et al.*, J. Phys. Chem. Solids **54**, 1323 (1994).
⁸S. Tajima *et al.*, Phys. Rev. B **35**, 696 (1987).
⁹E. S. Hellman and E. H. Hartford, Jr., Phys. Rev. B **47**, 11 346 (1993).
¹⁰B. Dabrowski *et al.*, Physica C **156**, 24 (1988).
¹¹M. Affronte, J. Marcus, and C. Escribè-Filippini, Solid State Commun. **85**, 501 (1993).
¹²E. S. Hellman and E. H. Hartford, Jr. (unpublished).
¹³David Emin, Phys. Rev. B **48**, 13 691 (1993).
¹⁴B. Batlogg *et al.*, Phys. Rev. Lett. **61**, 1670 (1988).
¹⁵David Emin, Adv. Phys. **24**, 305 (1975).
¹⁶H. G. Reik and D. Heese, J. Phys. Chem. Solids **28**, 581 (1967).
¹⁷David Emin (private communication).
¹⁸I. E. Graebner, L. F. Schneemeyer, and J. K. Thomas, Phys. Rev. B **39**, 9682 (1989).
¹⁹P. Monthoux and D. Pines, Phys. Rev. Lett. **69**, 961 (1992).
²⁰S. Sugai, Y. Enomoto, and T. Murakami, Solid State Commun. **72**, 1193 (1989).
²¹C. H. Rüscher, A. Heinrich, and W. Urland, Physica C **219**, 471 (1994).
²²L. Zuppiroli and L. Forro, Phys. Lett. A **141**, 181 (1989); David Emin, Phys. Rev. Lett. **32**, 303 (1974).
²³S. Uchida, H. Hasegawa, K. Kitazawa, and S. Tanaka, Physica C **156**, 157 (1988).

4.3 The doping dependence of the optical properties of $\text{Ba}_{1-x}\text{K}_x\text{BiO}_3$

This paper is an extension of the results and discussion presented in the preceding article. Since we believe that we have obtained a good evidence for formation of the space-localized electronic pairs, or bipolarons, in BKBO with $x = 0.31$, it is logical now to examine if bipolaron formation can be responsible for the other unusual properties of BKBO, in particular the doping dependence of the optical conductivity and the IM transition.

In this paper we analyze the doping dependence of the optical conductivity of $\text{Ba}_{1-x}\text{K}_x\text{BiO}_3$ in the whole accessible doping range using the partial sum rule analysis of the conductivity. We argue that the bipolaronic model presented in the previous section is at least a plausible possibility for explaining the nature of the doping-induced changes in the physical properties of BKBO. However, only more research, in particular theoretical, can provide a final answer on the validity of this model.

We also present the experimental data on three metallic and superconducting single crystals at different doping levels. We examine the doping dependence of the normal-state optical conductivity, the superconducting gap energy, and the density of the superconducting charge carriers.

The doping dependence of the optical properties of $\text{Ba}_{1-x}\text{K}_x\text{BiO}_3$.

A.V. Puchkov and T. Timusk

Department of Physics and Astronomy, McMaster University, Hamilton, Ontario, Canada L8S4M1

M.A. Karlow†, S.L. Cooper†, P.D. Han‡ and D.A. Payne‡

†Department of Physics, ‡Department of Material Science and Engineering, ††Material Research Laboratory, University of Illinois at Urbana-Champaign, 104 South Goodwin Avenue, Urbana, Illinois 61801

We analyze the doping dependence of the optical conductivity of the $\text{Ba}_{1-x}\text{K}_x\text{BiO}_3$ (BKBO) system in the full doping range from $x = 0$ to $x = 0.46$. We have used the results of our reflectivity and ellipsometric measurements at $x = 0.31, 0.38, 0.4, 0.46$, as well as the results obtained by other experimental groups at different doping levels, to analyze the doping dependence of the spectral weight distribution. At the insulator-metal transition boundary we observe the appearance of a Drude-like free-carrier peak in the optical conductivity. In the metallic phase, we have performed measurements in the normal as well as the superconducting states. The data show that BKBO becomes a better metal with increasing x in the metallic regime due to a decrease in the scattering rate of the metallic charge carriers, while the density of the mobile (Drude) charge carriers does not significantly change with doping. The London penetration depth λ_L is also found to be almost doping (and T_c) independent while the superconducting gap scales with T_c as $2\Delta_s/k_b T_c = 4.2 \pm 0.3$.

PACS numbers: 71.30.+h, 71.38.+i, 74.25.Gz

In the last two years several experimental reports regarding the insulator-metal (IM) transition and the evolution of optical properties as a function of doping level x in $\text{Ba}_{1-x}\text{K}_x\text{BiO}_3$ (BKBO) have been published.^{1,2} In this paper we use the large amount of experimental material accumulated to date to discuss the properties of the BKBO system in the non-metallic phase using sum-rule analysis. In the metallic phase, optical studies of the doping dependence have previously been done, to our knowledge, only at room temperature and at relatively high photon energies. We fill this gap by performing reflectivity and ellipsometric measurements in a combined range of $30\text{-}50000\text{ cm}^{-1}$ on three superconducting BKBO single crystals ($T_c = 21, 28, 31\text{K}$).

The BKBO single crystals used in this study were grown by an electrochemical method.³ The lattice parameters were measured by x-ray diffraction using a Rigaku D-max diffractometer (Cu $K\alpha$, $\lambda = 1.5405\text{ \AA}$). After the optical measurements, the crystals were ground into powder and x-ray diffraction measurements were carried out on the powdered sample intermixed with high-purity Ge powder which acted as an internal x-ray standard. The lattice parameters were refined by a least-square fit routine with calibration against Ge. The potassium concentration x was estimated from the linear relationship between pseudo-cubic lattice parameter a and potassium concentration x .⁴

The optical experiments were performed at temperatures ranging from $T_c/3$ to room temperature. We have used Kramers-Kronig (KK) analysis of reflectivity, supplemented by results of ellipsometric measurements, to obtain the complex optical conductivity $\sigma(\omega)$ in the normal and the superconducting states.

The undoped material BaBiO_3 has one electron per unit cell and therefore should be a metal with a half-

filled conduction band. However, it is in fact an insulator. Experimentally observed frozen breathing-type lattice distortions^{4,5} led to a suggestion that BaBiO_3 is made insulating by a charge-density wave (CDW) instability that opens a gap on the Fermi level, splitting the conduction band into two sub-bands: a filled lower CDW sub-band and an empty upper CDW sub-band.⁶ However, this model leaves some questions unanswered. In particular, there is no clear understanding of the nature of the mid-infrared, called hereafter "MIR", absorption peak at non-zero doping levels. Also, results of band structure calculations indicate that the observed lattice distortions are not sufficient to produce a gap in the electronic density of states.⁷ Another model, advanced to explain the insulating nature of BKBO at low doping levels, involves real-space pairing of electrons in pairs strongly localized on the Bi sites: small bipolarons.⁸ There is a number of experimental results that favor the bipolaronic model, including those of Raman scattering,⁹ infrared reflectivity,¹⁰ and high-resolution electron energy loss spectroscopy.¹¹ Several recent reports on the doping dependence of optical properties of the BKBO system^{1,2,10} allow us to examine this problem once again on a more quantitative level.

We will first concentrate on the properties of the BKBO system in the non-metallic phase and at the IM transition boundary. The optical conductivity of insulating BKBO shows a well resolved MIR peak with a maximum at $\hbar\omega_{max}$, equal to 2 eV in the undoped BaBiO_3 .^{1,2,12} As the doping level x increases, the position of the maximum of the MIR absorption shifts gradually to lower energies. However, this contribution to the optical conductivity can be observed at all doping levels. The IM transition occurs at $x_c \approx 0.33 - 0.35$ and is illustrated in Fig. 1, where optical conductivity is shown

⁰Reprinted from Phys. Rev. B, p. 6686 (1996). ©1996 The American Physical Society.

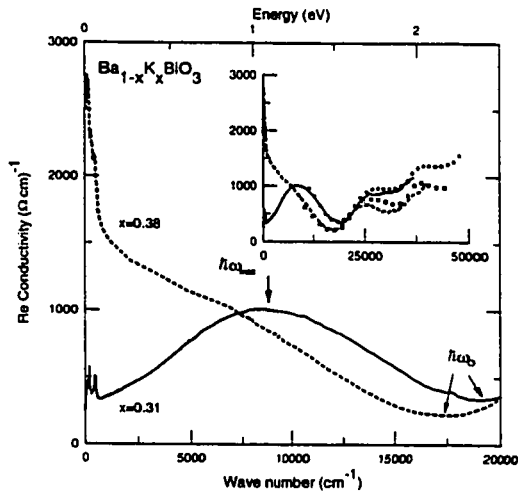


FIG. 1. The optical conductivity of $\text{Ba}_{1-x}\text{K}_x\text{BiO}_3$ just below and just above the insulator-metal transition. The characteristic energies $\hbar\omega_{\max}$ and $\hbar\omega_0$, used in the text, are shown. The inset: The lines represent the real part of the optical conductivity obtained from the KK analysis of reflectivity spectra. The symbols show results of ellipsometric measurements.

for the non-metallic sample with $x = 0.31$ and for the metallic sample with $x = 0.38$. The difference between the two curves is qualitative: while in the metallic sample $\hbar\omega_{\max}$ has collapsed to zero so that no clear maximum can be seen in the MIR absorption band, an additional free-carrier like narrow ($1/\tau \leq 300 \text{ cm}^{-1}$) absorption band has appeared at low frequency.¹³ This latter absorption component, called hereafter "Drude" absorption band, is responsible for the metallic properties of this material at doping levels $x > x_c$.

The MIR absorption band in BKBO is well separated from the rest of the interband absorption allowing us to employ a finite-energy f sum rule analysis to obtain the plasma frequency associated with the MIR absorption, ω_{pMIR} . The key requirement that must be satisfied in order for the finite-energy f sum rule to hold is that the absorption in question be sufficiently isolated. In this case the plasma frequency associated with the isolated absorption is calculated as an integral of the real part of the optical conductivity over energies from zero to a cut-off energy $\hbar\omega_0$,¹⁴ that must be chosen to exhaust the oscillator strength of the absorption in question but lie below the rest of the absorption bands. If $\hbar\omega_0$ is extended to infinity one obtains conductivity f sum rule where the plasma frequency w_p is given by the total density of electrons in the material (including inner-shell electrons), $w_p^2 = 4\pi n e^2 / m_b$, where n is the density of electrons and m_b is a bare electron mass.

In analogy with the f sum rule we can define an effective density of electrons contributing to the optical transitions represented by the MIR band, n_{eff} , by

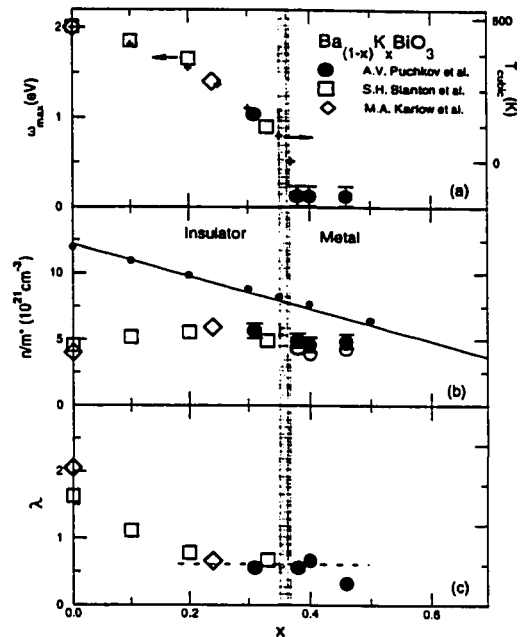


FIG. 2. (a) Large symbols: the doping dependence of the peak energy of the MIR absorption band. Crosses: the doping dependence of temperature of structural transition into the high-temperature cubic phase, T_{cubic} , plotted as described in the text. (b) Large symbols: the doping dependence of the spectral weight of the MIR absorption band obtained as described in the text. The straight line shows the doping dependence of the spectral weight as expected from the chemical composition. The small dots near the straight line were obtained using the actual lattice parameters. (c) The doping dependence of the factor $\lambda(x)$, obtained using results shown in panel (b).

$\omega_{pMIR}^2 = 4\pi n_{eff} e^2 / m_b$. On the other hand, the density of electrons n can also be determined from the chemical composition using the concentration of Bi ions x : $n(x) = (1-x)/v_c$, where v_c is a volume per Bi ion. The $n(x)$, calculated this way, is plotted as the straight line in Fig. 2b. To calculate the straight line, average lattice parameters of the BKBO system were used to obtain v_c . Taking into account the actual changes in the lattice parameters with doping does not change the result significantly: we have used experimentally obtained⁴ lattice parameters to calculate $n(x)$ at several x and the results, shown by the small dots, are very close to the straight line. In an analogy with the case of metals with strong electron-phonon interaction,¹⁵ we define the optical effective mass $m^* = n/n_{eff}$, or mass enhancement factor $\lambda = m^* - 1$, as a quantity that measures the amount of the conductivity spectral weight moved to energies $\hbar\omega > \hbar\omega_0$ through the optical transitions other than those represented by the MIR absorption band. If

$\hbar\omega_0$ is large enough so that *all* possible optical transition processes are taken into account the optical effective mass is equal to the bare electron mass $m^* = 1$ and the oscillator strength is determined only by the density of electrons n . Filled core electron bands may give their own correction to the effective mass value due to the Pauli principle. This correction is, however, estimated to increase valence/conduction electron oscillator strength by only about 10–20%¹⁴ and will therefore be neglected in further discussions.

We have used $\sigma_1(\omega)$ obtained by different groups on $\text{Ba}_{1-x}\text{K}_x\text{BiO}_3$ at different doping levels to obtain the doping dependence of the oscillator strength of the MIR absorption peak, performing integration of $\sigma_1(\omega)$ as described above. The typical choice of the cut-off frequency is shown in Fig. 1 while the results of our integration are presented in Fig. 2b. We note that the Drude mobile electrons at $x > x_c$ have a relatively small oscillator strength (about 6% of the MIR) so that the results presented in Fig. 2b effectively represent oscillator strength of the MIR electrons even for the metallic samples. For the metallic samples we have used the loss-function method¹⁶ (with the high-frequency dielectric constant taken from our ellipsometric results) as an alternative to the sum-rule method. The results obtained from the loss function analysis are plotted by the open circles.

In this kind of calculation a high degree of accuracy in measuring the absolute value of optical conductivity is obviously very important. Therefore for the heavily doped insulating as well as the metallic samples, where both low- and high-frequency parts of the optical conductivity spectrum contain significant spectral weight, a combination of ellipsometric (above 1 eV) and reflectivity (from $25 \text{ cm}^{-1} = 3.1 \text{ meV}$) results have been used. The nearly perfect agreement between the ellipsometric results, which give dielectric constants above 1 eV directly, and $\sigma_1(\omega)$ obtained from KK analysis of reflectivity data, is shown in the inset of Fig. 1. Spectral weight values obtained from results of different experimental groups at different doping levels are consistent with each other giving a smooth doping dependence. A measure of inconsistency is given by the mismatch of the two oscillator strength values at $x = 0$ obtained from the results of two different groups that used different optical methods on thin films and single crystals. The inconsistency is about 25% and can possibly be due to an error in choosing a high-frequency reflectivity approximation in Ref. 2, where $\sigma_1(\omega)$ was obtained by KK analysis of reflectivity. Ellipsometric measurements give dielectric constants directly in the energy range of the MIR absorption at $x = 0$ and therefore we consider the value obtained by Karlow *et al.* to be more reliable. Still, 25% can be considered to be our experimental error in evaluating the oscillator strength.

Results for the doping dependence of the oscillator strength $n(x)/m^*(x)$ obtained using sum-rule analysis (large symbols in Fig. 2b) are remarkably different from those expected from the chemical composition (straight

line in Fig. 2b), leading to high values of m^* at low doping levels, with the highest value being that for the undoped BaBiO_3 $m^*(0) \simeq 3$. These high values of m^* mean that there is a high-energy ($\hbar\omega > \hbar\omega_0$) absorption, not included in our integration, that contains a significant part of the spectral weight. Put differently, not all possible optical transitions involving $n(x)$ chemically doped electrons have been included in our integration. The doping dependence of the mass enhancement factor $\lambda(x) = m^*(x) - 1$, obtained from the ratio of $n(x)$ to $n(x)/m^*(x)$, is plotted in Fig. 2c. The value of $\lambda(x)/(\lambda(x) + 1)$ gives a fraction of the spectral weight contained at high frequencies so that $\lambda(0) \simeq 2$ means that in BaBiO_3 about 2/3 of the total spectral weight due to $n(x)$ chemically doped electrons is contained in the high energy region above $\hbar\omega_0$. The region of fastest change in $\lambda(x)$ with doping is below $x = 0.2$. At $x > 0.2$ $\lambda(x)$ is almost doping-independent and is approximately equal to 0.5, that is the spectral weight contained in the higher energy region is only half of that contained in the MIR absorption band. Estimating our error range somewhat pessimistically, we can not say with certainty whether or not λ is zero at $x = 0.46$.

Let us see if the CDW model where a single gap opens in the spectrum of electronic excitations, can provide an explanation for the observed doping behavior of the spectral weight. The opening of a *single* gap in the middle of an initially half filled conduction band redistributes electronic density in the energy region covered by the conduction band creating filled lower sub-band and an empty upper sub-band. As a result a *single* peak appears in the absorption spectrum positioned at the gap energy corresponding to electronic excitations from the lower sub-band to the empty upper sub-band. Assuming that no other optical transitions became possible with the opening of the gap, that is, for example, electronic states in both sub-bands are still well defined so that no incoherent processes such as those involving emission or absorption of a phonon occur, the optical effective mass of the resulting interband absorption peak must still be equal to unity. In other words opening of a single gap piles up the spectral weight at energies above the gap value, preserving its total integrated value. Therefore, we conclude that the distribution of the spectral weight discussed above can not be explained by a single gap in a density of states *only*. Optical excitation processes other than direct excitations across the gap are required.

One such possibility to account for the "missing" spectral weight is to assume that it is contained in the absorption bands corresponding to high-order interband excitations (that is transitions from lower CDW sub-band to bands higher than upper CDW sub-band in the CDW model, for example). However, high-order interband transitions usually have matrix elements smaller than that for the first interband transition and therefore do not contain a significant part of the spectral weight. Even if for some reason matrix elements of such transitions are unusually large in BKBO so that they account

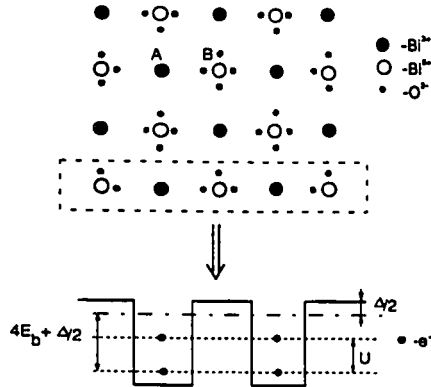


FIG. 3. The antiferromagnetic-type (bi)polaronic lattice. The (bi)polaronic sub-lattice is the sub-lattice A, the empty sub-lattice is the sub-lattice B. The lower part of the diagram shows schematically the energy configuration for one $\text{Bi}^{+5}-\text{Bi}^{+3}$ row with parameters discussed in the text. Polaronic lattice, at doping $x = 0.5$, will look similar but each site in the sub-lattice A will contain only one electron

for a considerable amount of the spectral weight (twice that for the lower-to-upper sub-band transitions!) it is unclear why the *fastest* change in the amount of this spectral weight occur in the doping region from $x = 0$ to $x = 0.2$, the region of *slowest* change in the position of the MIR absorption peak $\hbar\omega_{\max}$, associated with the electronic gap energy, and, therefore, with the band structure itself. Also, the first interband absorption peak above 2 eV can be observed at all doping concentrations,^{1,2} including those where $\lambda \approx 0$ and therefore all of the chemically doped electrons are accounted for by the MIR absorption. We consider this behavior an indicator that it is unlikely that the missing spectral weight is associated with high-order interband transitions.

Another way to account for the spectral weight distribution is through incoherent processes. As we have noted before, a number of publications appear to support the real-space electron-pairing (small bipolaron or local CDW) model for BKBO. This model is different from the conventional CDW model in that bipolaron motion is incoherent due to severe localization of the electron pairs. We will examine the small bipolaron model next.

A small bipolaron (SBP) consists of two charge carriers strongly localized on a single site by their own short-range interaction with the lattice, taken together with the lattice displacement pattern caused by the interaction. Although a small bipolaron can be formed with a pair of holes as well as a pair of electrons, in the following by a small bipolaron we will mean the one that includes a pair of electrons. As a result of the electron-lattice interaction a potential well of depth $-4E_b$ is formed, where E_b is the small-polaron binding energy.¹⁷ The ground-state energy of a SBP is, however, increased by the on-site Coulomb interaction energy U , a result of two electrons

being on the same site. A small polaron is similar to a small bipolaron but contains only one electron.¹⁷ A single SBP is stable with respect to decay into two small polarons if the Coulomb energy U satisfies the condition $U < 2E_b$.¹⁷

We note that the bipolaronic model implies a doubling of the unit cell by a lattice modulation similar to what is observed experimentally in the undoped BaBiO_3 .^{4,5} In analogy with small polarons,¹⁸ there is a strong repulsive interaction between two neighboring SBP's in BKBO as they disturb each other's pattern of oxygen ion displacements, thus raising the total energy. The interaction becomes weaker as the average distance between SBP's is increased. BaBiO_3 has one electron per formula unit and therefore the number of SBP's is half the number of Bi ions. As a result, individual SBP's are situated close to each other and the energy of interaction between SBP's is an important part of the total energy. Using a magnetic analog of this system it can be shown⁸ that, taking the interaction into account, the lowest energy is given by an antiferromagnetic-type configuration such as the one shown in Fig. 3. There are two interleaving fcc sub-lattices in this configuration: bipolaronic ($\text{Bi}^{+3} = \text{Bi}^{+5} + 2e^-$) sub-lattice A and empty (Bi^{+5}) sub-lattice B. The Bi^{+5} sites are strongly screened by overlap from the oxygens so that no site is strongly charged.¹⁹

A bipolaron can be excited in two ways. In the first scenario the pair of electrons associated with a bipolaron is excited to a neighboring Bi^{+5} site as a whole (two-particle excitation). This gives a peak in the corresponding absorption spectrum at $\hbar\omega_2 = 8E_b + 2\Delta$,²⁰ where by Δ we denote the difference in energy between the two sub-lattices due to bipolaron-bipolaron interaction. The second scenario involves pair-breaking with excitation of a single electron (single-particle excitation). This gives an absorption peak at $\hbar\omega_1 = 4E_b - U + \Delta$.²⁰ The condition for formation of a single small bipolaron, $U < 2E_b$, is relaxed to a condition of stability of a bipolaron with respect to decay into one small polaron on sub-lattice A and one on sub-lattice B, $U < 2E_b + \Delta$. In fact, if $2E_b < U < 2E_b + \Delta$ a lattice of small bipolarons may form although formation of *individual* small bipolarons is not energetically favorable. The peak frequency of the absorption band corresponding to the one-particle excitations, $\hbar\omega_1$, is always smaller than that corresponding to the two-particle excitations, $\hbar\omega_2$. The two processes can in general coexist, giving two peaks in the corresponding optical conductivity. The spectral weight under both peaks must correspond to the total number of chemically doped carriers (or double the number of bipolarons) in a system. Therefore, the bipolaronic model can in principle provide an explanation for the fact that the spectral weight under the low-energy peak in the non-metallic BKBO is too small — the rest of spectral weight may be contained in the absorption peak corresponding to the two-particle excitation process.

One difficulty arise here. It has been shown²¹ that the exponential terms in the expressions describing intensi-

ties (and spectral weights) of the absorption peaks corresponding to the two- and single-particle excitations are comparable. However, the SBP absorption intensity involves a pre-exponential factor, proportional to t_2^2 for the two-particle excitations and to t_1^2 for the single-particle excitations, where t_2 is a two-electron transfer energy (of order of an exchange energy) and t_1 is a one-electron transfer energy. The value of t_2 is usually smaller than t_1 and, therefore, at least for a dc motion of a single bipolaron by temperature-assisted hops in a periodic crystal potential, the single-particle excitation mechanism is thought to be more favorable¹⁸ so that the lower-energy (single-particle) absorption peak is supposed to be more intense. The experimental situation, at least for the undoped BaBiO₃, is just the reverse: the low-frequency absorption peak contains just about 1/3 of the total spectral weight. However, the transfer energies for the thermal bipolaronic dc motion and the bipolaronic optical absorption may be different as they strongly depend on the atomic displacements.²⁰ In case of dc motion one is interested in the transfer energy of thermally equilibrated carriers. In case of optical absorption one is concerned with the transfer energy of a carrier at the coincidence event between energies of initial and final electronic states. Also, imperfections in the bipolaronic lattice, such as singly occupied sites, can give their own contribution to the optical conductivity through such processes as, for example, hop of an electron from a doubly occupied site to the singly occupied site. The energy required by such processes may be smaller or larger than the energy of the main single-particle excitation process, $\hbar\omega_1 = 4E_b - U + \Delta$, depending on the relation between E_b and Δ . Detailed perturbation theory calculations (including terms up to t_1^4) for a lattice of bipolarons would be helpful to the understanding of the optical transition probabilities and, therefore, the exact conductivity spectral weight distribution expected for this system.

Doping with potassium destroys bipolarons. When x is small, substituting K⁺ for Ba²⁺ has an effect of taking one electron from a pair on an adjacent Bi³⁺ site. The electron that is left is, however, still localized on the Bi site in a potential well created by the surrounding bipolaronic lattice. At the same time, destroying a pair decreases the local energy difference Δ between B and A sub-lattices, making the surrounding electron pairs less stable and decreasing the bipolaronic hopping energy. Therefore, the frequency of the one-particle excitation peak in the optical conductivity will be reduced. Also, the spectral weight will shift to lower frequencies as there are fewer possibilities to excite a pair as a whole — there are fewer pairs. When doping is large enough so that a bipolaron coordination number z is smaller than a certain critical value z_c and $U > 2E_b + \Delta$, a first-order phase transition with discontinuous reduction of electron pairs will occur. However, the remaining electrons still strongly interact with the lattice so that in the hypothetical case where the transition occurs at $x_c = 0.5$ (and there are no remaining bipolaronic islands) they would

arrange themselves in a *polaronic* lattice similar to that shown in Fig. 3 for *bipolarons*. However, if the transition occurs at $x_c < 0.5$, there are too many electrons left to form the antiferromagnetic-type lattice of Fig. 3. The extra $(0.5 - x_c)$ electrons have no place in the (now polaronic) sub-lattice A since the Coulomb repulsion U is too large to form a bipolaron. On the other hand, if they try to form polarons on the sub-lattice B they disturb the atomic displacement patterns of neighboring polarons on sub-lattice A, reducing their stability and possibly releasing some of the localized carries. Therefore, if $x_c < 0.5$ the electronic system may consist of dynamically occupied extended and localized states. This may explain the two optical absorption components: the MIR band represents electrons in the localized (experimental mean-free path about 6 Å) states and the Drude absorption is due to charge carriers in the extended states (mean-free path of several hundred Å's). Experimentally, the spectral weight of the Drude electrons is about 6% of that of the MIR electrons at all metallic doping levels. However it is difficult to assess if it is consistent with the model described above without detailed self-consistent calculations, in part because some fraction of the electrons may still be contained in the remaining bipolaronic islands. We note that our results do not exclude a possibility that the itinerant charge carriers are *large* bipolarons, which are bosons and may condense into a superfluid-like state at low temperatures.

It is interesting to compare the electronic gap in the BKBO system with the transition temperature from the "deformed" lattice configuration shown in Fig. 3 into the simple-cubic lattice phase, T_{cubic} . We have plotted T_{cubic} , adopted from Ref. 7, by the crosses in Fig. 2a as a function of doping together with the peak energy of the MIR absorption. The temperature scale has been chosen to normalize T_{cubic} to $\hbar\omega_{max}$ values. Also, we have put the zero of T_{cubic} near the lowest $\hbar\omega_{max}$ value corresponding to the lowest excitation energy of *paired* electrons, at x just below the IM transition boundary x_c . This minimal value of $\hbar\omega_{max}$ is equal to the excitation energy of a small polaron. Therefore, we effectively compare T_{cubic} with the reduction of electronic energy due to formation of *pairs*. The result is that the two quantities have surprisingly similar doping dependence suggesting an intimate relationship between the lattice vibrations and the dielectric properties of in BKBO. However, the large difference in absolute values (about 20 times) still needs an explanation. Also, high-temperature dc transport measurements would be useful to determine the properties of the high-temperature phase of undoped BaBiO₃, in particular to determine if it is actually metallic.

Although it has been shown a number of times^{22,23} that the superconducting properties of metallic BKBO are closely related to those of the BCS model, results of a number of experiments indicate that the usual Fröhlich electron-phonon interaction is not strong enough to obtain $T_c \simeq 31$ K.²²⁻²⁶ It was concluded therefore that,

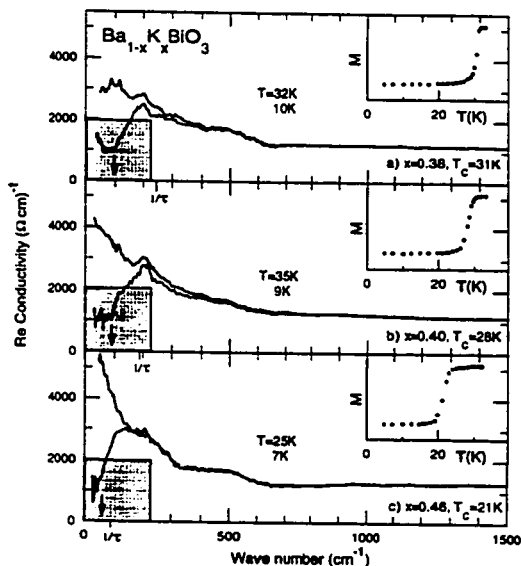


FIG. 4. The optical conductivity of the three metallic samples BKBO in the superconducting and the normal states. The results of magnetization measurements are shown on the inserts. The scattering rate values $1/\tau$ in the normal state are shown on the frequency axis for all three samples. The shaded squares represent the spectral weight of the superconducting carriers. The London penetration depth λ_L is inversely proportional to the side of the square. The position of the superconducting gap energy $2\Delta_s$ is shown by the arrows

although the mechanism of superconductivity in BKBO is probably BCS, electron-electron interaction is not mediated by phonons in the usual way.²² We note in this respect that electrons, occupying the extended states in the system described above, may be prone to a relatively strong electron-electron interaction due to polarizability of the localized states. It has been shown that high values of T_c can be achieved in a BCS model with such interaction.²⁷

The optical conductivity for the metallic samples just above T_c and at $T=T_c/3$ is plotted in Fig. 4 at three different doping levels. The MIR absorption component is an almost flat background in this frequency range and has about the same value for all doping levels presented. The metallic BKBO is frequently thought to be an "overdoped" system,²⁵ that is both decrease of T_c and improvement of the metallic properties are thought to be connected to an increase of the total density of metallic carriers. However, we did not observe a significant increase in the density of normal-state metallic (Drude) electrons with increasing x from $x = 0.38$ to $x = 0.46$, while low-temperature dc conductivity increased more than twice and T_c fell by 30%. The increase in the dc conductivity value with doping is mainly due to the decrease in the scattering rate $1/\tau$. The normal-state $1/\tau$

values of the Drude absorption at different x were determined from a fit to a two-component model similar to that used by us before²⁶ and are shown on the horizontal axis for the three doping levels. The simultaneous reduction of T_c and scattering rate with increasing x in the metallic regime suggests that $1/\tau$ may include scattering of free carriers on bosonic excitations that mediate the superconducting pairing at low temperatures and are responsible for transport scattering.

The low-frequency depression of $\sigma_1(\omega)$ at $T < T_c$ is due to formation of the superfluid. We can roughly estimate the position of the superconducting gap $2\Delta_s$, as shown in Fig. 4 by arrows on all three panels. The gap energy decreases with decreasing T_c , keeping the ratio $2\Delta_s/k_B T_c = 4.2 \pm 0.3$ constant. The spectral weight that disappears in the superconducting state is contained in a δ -peak at zero frequency and represents carriers that have condensed into the superfluid. Therefore the "missing" spectral weight is the spectral weight of the superconducting carriers and we can use it to estimate the London penetration depth value λ_L . We have performed the necessary calculations and the result is that within our error range λ_L has the same value $3750 \pm 100 \text{ \AA}$ at all doping levels, despite different T_c 's.²⁸ To make it more graphic we have drawn squares of areas equal to the spectral weight "missing" in the superconducting state for all three doping levels. The sides of the squares are inversely proportional to λ_L and one can see that they are equal for all three samples. The areas themselves are proportional to the density of the superconducting carriers. Although the physical reasons for insensitivity of λ_L to the doping level are not clear, one can see that there are two factors contributing to it: decreasing superconducting gap value and a decreasing scattering rate. While decrease in the scattering rate tends to pile up more conductivity below the superconducting gap energy in the normal state, increasing the number of carriers that condense into a superfluid at $T < T_c$, decrease of the superconducting gap value tends to compensate for this.

In conclusion we have shown that the anomalous doping dependence of distribution of the optical conductivity spectral weight in the BKBO system can not be explained within the framework of a coherent-transport model with well-defined energy bands. This naturally leads to local a CDW, or bipolaronic, model. We have shown that this model can, at least qualitatively, explain some of the physical properties of the BKBO system, including the IM transition. However, we strongly emphasize that only more rigorous calculations than those presented in this work can provide the final answer. Experimentally, the IM transition at $x = x_c$ is associated with the appearance of the narrow free-carrier like Drude absorption peak in the optical conductivity spectra. As the doping level increases in the metallic phase the width of the Drude peak decreases, increasing the dc conductivity value. At the same time the density of free carriers represented by the Drude absorption, as well as the London penetration depth value λ_L at $T=T_c/3$, do not change much with

doping. The superconducting gap value Δ , scales with T_c in a rough proportion $2\Delta/k_B T_c = 4.2 \pm 0.3$.

We would like to thank David Emin for many helpful discussions. This research was supported in part by the National Science and Engineering Research Council of Canada and by the Canadian Institute for Advanced Research. Research at the University of Illinois at Urbana-Champaign was sponsored by Contract No. NSF DMR 91-20000.

-
- ¹ M.A. Karlow, S.L. Cooper, A.L. Kotz, M.V. Klein, P.D. Han and D.A. Payne, *Phys. Rev. B* **48**, 6499 (1993).
- ² S.N. Blanton, R.T. Collins, K.H. Kelleher, L.D. Rotter, Z. Schlesinger, D.G. Hinks and Z. Zheng, *Phys. Rev. B* **47**, 996 (1993).
- ³ P.D. Han, L. Chang and D.A. Payne, *J. Crystal Growth*, **128**, 798 (1993).
- ⁴ Shiyou Pei, J.D. Jorgensen, B. Dabrowski, D.G. Hinks, D.R. Richards, A.W. Mitchell, J.M. Newsam, S.K. Sinha, D. Vaknin and A.J. Jacobson, *Phys. Rev. B* **41**, 4126 (1990).
- ⁵ D.E. Cox and A.W. Sleight, *Acta Crystallogr. Sect. B* **35**, 1 (1979).
- ⁶ L.F. Mattheiss and D.R. Hamann, *Phys. Rev. B* **28**, 4227 (1983).
- ⁷ K. Takegahara, *J. Electron Spectrosc. Relat. Phenom.* **66**, 303 (1994).
- ⁸ T.M. Rice and L. Sneddon, *Phys. Rev. Lett.* **47**, 689 (1981).
- ⁹ S. Sugai, Y. Enomoto and T. Murakami, *Solid State Comm.* **72**, 1193 (1989).
- ¹⁰ A.V. Puchkov, T. Timusk, M.A. Karlow, S.L. Cooper, P.D. Han and D.A. Payne, *Phys. Rev. B* **52**, R9855 (1995).
- ¹¹ Y.Y. Wang, V.P. Dravid, N. Bulut, P.D. Han, M.V. Klein, S.E. Schnatterly and F.C. Zhang, *Phys. Rev. Lett.* **75**, 2546 (1995).
- ¹² S. Tajima, S. Ucida, A. Masaki, H. Takagi, K. Kitazawa, S. Tanaka and A. Katsui, *Phys. Rev. B* **35**, 696 (1987).
- ¹³ The total optical conductivity in the metallic phase of BKBO can be fitted equally well by a sum of the MIR absorption band, modelled by an oscillator centered anywhere from 0 to 2000 cm^{-1} , and a Drude absorption band.
- ¹⁴ D.Y. Smith, *Dispersion Theory, Sum Rules, and Their Application to the Analysis of Optical Data*, in *Handbook of Optical Constants of Solids*, Edward D. Palik, editor, (Academic Press, London, 1985), pp. 35-64.
- ¹⁵ P.B. Allen, *Phys. Rev. B* **3**, 305 (1971).
- ¹⁶ Ivan Bosovic, J.H. Kim, J.S. Harris, Jr., E.S. Hellman, E.H. Hartford, P.K. Chan, *Phys. Rev. B* **46**, 1182 (1992).
- ¹⁷ David Emin, *Phys. Rev. B* **48**, 13691 (1993).
- ¹⁸ David Emin, *Physics Today* **35**, 34 (1982).
- ¹⁹ Nevill Mott, *Supercond. Sci. Technol.* **4**, S59 (1991).
- ²⁰ David Emin, *Phys. Rev. B* **53**, January 15 (1996); also David Emin, private communication.
- ²¹ V.V. Bryksin and V.S. Voloshin *Sov. Phys. Solid State* **26**, 1429 (1984).
- ²² F. Marsiglio, J.P. Carbotte, A.V. Puchkov and T. Timusk, (unpublished).
- ²³ F. Sharifi, A. Pargellis, R.C. Dynes, B. Miller, E.S. Hellman, I. Bosamilia and E.H. Hartford, Jr., *Phys. Rev. B* **44**, 1191 (1991).
- ²⁴ F. Marsiglio and J.P. Carbotte, *Phys. Rev. B* in press; J.E. Graebner, L.F. Schneemeyer, and J. Thomas, *Phys. Rev. B*, **39**, 9682 (1989).
- ²⁵ B. Batlogg, R.J. Cava, L.W. Rupp, Jr., A.M. Muzsca, J.J. Krajewski, J.P. Remeika, W.F. Peck, Jr., A.S. Cooper and G.P. Espinosa, *Phys. Rev. Lett.* **61**, 1670 (1988);
- ²⁶ A.V. Puchkov, T. Timusk, W.D. Mosley and R.N. Shelton, *Phys. Rev. B* **50**, 4144 (1995).
- ²⁷ See, for example, Vladimir Z. Kresin and Stuart A. Wolf, *Fundamentals of Superconductivity*, (Plenum Press, New York, 1990). Also A.J. Heeger and G. Yu, *Phys. Rev. B* **48**, 6492 (1993).
- ²⁸ The value of λ_L obtained by us previously (Ref. 26) was somewhat overestimated due to lack of reliable high-frequency reflectivity data. Using ellipsometric results in combination with the reflectivity data makes λ_L more reliable.

Appendix A

The extended Drude formalism

A.1 The Complex Memory Function.

The classical Drude formula for the dynamical conductivity $\sigma(\omega) = \sigma_1(\omega) + i\sigma_2(\omega)$ [Timusk89, Ashcroft76] can be obtained by using a standard Boltzmann equation and approximating the collision integral with a single collision frequency $1/\tau$. The Drude formula describes the free-carrier contribution to $\sigma_1(\omega)$ as a Lorentzian peak centered at zero frequency with an oscillator strength $\omega_p^2/8$, where $\omega_p^2 = e^2/(3\pi^2\hbar)\int\mathbf{v}\cdot d\mathbf{S}_F$ and \mathbf{v} is the electron velocity and \mathbf{S}_F is the element of Fermi surface. For a spherical Fermi surface $\omega_p^2 = 4\pi ne^2/m_e$, where n is the free-carrier density and m_e is the electronic band mass. The Lorentzian width is determined by a constant scattering rate $1/\tau$. The imaginary part of $\sigma(\omega)$ is just the real part multiplied by $\omega\tau$:

$$\sigma(\omega) = \frac{1}{4\pi} \frac{\omega_p^2}{1/\tau - i\omega} = \frac{\omega_p^2}{4\pi} \left[\frac{\tau}{1 + (\omega\tau)^2} + i \frac{\tau^2\omega}{1 + (\omega\tau)^2} \right] \quad (\text{A.1})$$

A derivation of Eq. A.1 by using the standard kinetic Boltzmann equation assumes that the system of elementary excitations are well-defined. However, a description of a system by using elementary excitations is possible, strictly speaking, only if the (energy) width of the wave packet representing the electronic excitation is small compared to the energy of the packet. In more formal language, for the approximations leading to Eq. A.1 to be valid, a spectral function of electronic excitations, defined as:

$$A(\mathbf{k}, \omega) = -\frac{1}{\pi} |ImG(\mathbf{k}, \omega)| = \frac{1}{\pi} \frac{Im\Sigma(\omega)}{(\omega - \epsilon_{\mathbf{k}} - Re\Sigma(\omega))^2 + (Im\Sigma(\omega))^2}, \quad (\text{A.2})$$

must be a narrow peak centered at $\omega = \epsilon_{\mathbf{k}} + Re\Sigma(\omega)$. Here $G(\mathbf{k}, \omega)$ is a Green function of electronic excitation and $\Sigma(\omega)$ is the self-energy part. The narrowness of the peak means that the excitation energy must be much larger than the damping term $\gamma(\omega) = -2Im\Sigma(\omega)$. This is certainly true in case of standard Fermi-liquid theory, where $Re\Sigma(\omega) \sim \omega$ and $Im\Sigma(\omega) \sim \omega^2$ so that the electronic excitations (quasiparticles) are well-defined at zero temperature and energies close to the Fermi energy E_F . [Abrikosov75] It can also be shown [Shulga91] that a weak electron-phonon coupling, although it violates the quasiparticle description at energies very close to E_F , does not drastically change the transport properties at low temperatures, since in this case the number of electronic states where the quasiparticle description is violated is small. Therefore, the Drude formula is applicable only for simple metals at low frequencies and low temperatures where elastic scattering from impurities and weak quasielastic scattering from thermally excited excitations such as phonons dominate. [Timusk89, Shulga91]

On the other hand, following the original ideas of Anderson, [Anderson87] it is now widely accepted that the electronic system of HTSC materials represent a new kind of quantum liquid and the simple Fermi-liquid quasiparticle description is not applicable to the normal-state properties of these materials. For example, the key ingredient of the phenomenological "marginal" Fermi-liquid theory, [Schmitt-Rink88] advanced to explain these properties, is the assumption that the $Im\Sigma(\omega) \sim \omega$ and, consequently, $Re\Sigma(\omega)$ diverges logarithmically at the Fermi energy, thus making $G(\mathbf{k}, \omega)$ entirely incoherent at E_F . On a more microscopic level, a similar result is expected for the quasi-one dimensional Hubbard model, which was identified by Anderson as an appropriate paradigm for the resonant valence bond (RVB) description. [Anderson87] Even in more Fermi-liquid-like scenarios, sufficiently strong coupling of an electronic system to a bosonic energy spectrum may result in a violation of the quasiparticle description. [Shulga91] In addition, the Fermi energy is estimated to be only $E_F = 1 - 2$ eV, which is not much larger than the energies probed in infrared experiments (4-300 meV). Such a low E_F may be another reason for violation of a

quasiparticle description. Since this implies the absence of well-defined elementary excitations, the approximations used to obtain Eq. A.1 are not justified. The breakdown of the quasiparticle description has also been discussed by Emery and Kivelson in the context of abnormally short values of the mean free path that lead to the violation of the Ioffe-Rigel criterion. [Emery95a]

However, the optical conductivity can be described in a much more general way by making the damping term in the Drude formula complex and frequency-dependent: $1/\tau = M(\omega) = M'(\omega) + iM''(\omega)$, where $M(\omega)$ is called a memory function. [Allen76, Mori65, Götze72] The $M(\omega)$ satisfies $M'(\omega) = M'(-\omega)$ and $M''(\omega) = -M''(-\omega)$. The consequences of this formalism, usually referred to as the extended Drude model, have been derived for the infrared conductivity of metals with a strong electron-phonon interaction by Allen [Allen71] and Allen and Mikkelsen [Allen76] for the case of zero temperature. The analysis was later extended for the case of finite temperatures by Shulga *et al.* [Shulga91] It is also believed that the resulting theory is valid in the case of coupling of a Fermi liquid to any bosonic energy spectrum. Some aspects of the extended Drude model were also examined in detail by Götze and Wölfe. [Götze72] We are not aware of any quantitative predictions regarding the extended Drude model in the completely non-Fermi-liquid scenario, such as the Luttinger-liquid theory. Therefore, in the following we will employ the Fermi-liquid terminology. The formalism has been previously applied to transition-metal compounds, [Allen76] heavy-fermion materials, [Webb86, Dolgov95] and the HTSC cuprates. [Thomas88, Collins90, Rieck95, Basov96, Puchkov96c]

Rewriting the complex conductivity $\sigma(\omega)$ in terms of a complex memory function, $M(\omega, T) = 1/\tau(\omega, T) - i\omega\lambda(\omega, T)$, we obtain [Timusk89, Mori65]:

$$\sigma(\omega, T) = \frac{1}{4\pi} \frac{\omega_p^2}{M(\omega, T) - i\omega} = \frac{1}{4\pi} \frac{\omega_p^2}{1/\tau(\omega, T) - i\omega[1 + \lambda(\omega, T)]} \quad (\text{A.3})$$

Although, in the case of a metal, Eq. A.3 can be obtained using Boltzmann-equation formalism with a frequency dependent scattering rate, [Allen76] this form has in fact a range of validity more general than the Boltzmann-equation approach. [Allen76, Mori65] Adopting the Boltzmann-type terminology, the quantities $1/\tau(\omega, T)$ and $\lambda(\omega, T)$ describe the frequency-dependent scattering rate and mass enhancement of electronic excitations due to many-body interactions.

Using the more general form of Eq. A.3, we can check the range of validity of the classical Drude formula of Eq. A.1 by expanding the memory function into Taylor series for small frequencies:

$$\lim_{\omega \rightarrow 0} M(\omega) = \frac{1}{\tau(0)} - i\lambda(0)\omega + O(\omega^2) \quad (\text{A.4})$$

Substituting this into Eq. A.3 we find:

$$\sigma(\omega, T) = \frac{1}{4\pi} \frac{\omega_p^2}{1/\tau(0) - i\omega(1 + \lambda(0))}, \quad (\text{A.5})$$

recovering Eq. A.1. The classical Drude result is thus valid whenever expansion of Eq. A.4 makes sense and $\lambda(0)$ is small compared to unity.

Eq. A.3 can be reduced to the familiar Drude form of Eq. A.1 by introducing the so called renormalized scattering rate $1/\tau^*(\omega, T) = 1/[\tau(\omega, T)(1 + \lambda(\omega, T))]$ and the effective plasma frequency $\omega_p^{*2}(\omega, T) = \omega_p^2/(1 + \lambda(\omega, T))$:

$$\sigma(\omega, T) = \frac{1}{4\pi} \frac{\omega_p^{*2}(\omega, T)}{1/\tau^*(\omega, T) - i\omega} \quad (\text{A.6})$$

As it can be seen from this equation, the optical conductivity is now composed of an infinite set of Drude peaks, each describing $\sigma(\omega)$ in the vicinity of a particular frequency ω with a set of parameters $1/\tau^*(\omega)$ and $\lambda(\omega)$ (for simplicity in the following we will drop the temperature parameter when it is not relevant to the discussion). The $1/\tau^*(\omega)$ has the phenomenological meaning of a width of the Drude peak local to a frequency ω while $\lambda(\omega)$ represents the interaction-induced velocity renormalization. The renormalized scattering rate $1/\tau^*(\omega)$ is not causal and, other than the local Drude width, does not have a real physical meaning as it includes both the velocity renormalization and the lifetime effects.

On the other hand, $1/\tau(\omega)$ is, up to a constant, the real part of $1/\sigma(\omega)$

$$1/\tau(\omega) = \frac{\omega_p^2}{4\pi} \text{Re}\left(\frac{1}{\sigma(\omega)}\right), \quad (\text{A.7})$$

that is, the real part of a physical response function. In the limit of zero frequency the normal-state optical conductivity is completely real and Eq. A.4 becomes $1/\sigma_{dc}(T) = \rho_{dc}(T) = m_e/(\tau(T)ne^2)$, where $\rho_{dc}(T)$ is the dc resistivity. This is the same form as

the relaxation-time expression for the dc resistivity of a free electron gas and therefore $\tau(\omega, T)|_{\omega=0}$ may be viewed as an electronic lifetime.

The mass enhancement factor $\lambda(\omega)$ is given as the imaginary part of $1/\sigma(\omega)$:

$$1 + \lambda(\omega) = -\frac{\omega_p^2}{4\pi} \frac{1}{\omega} \text{Im}\left(\frac{1}{\sigma(\omega)}\right). \quad (\text{A.8})$$

The total plasma frequency ω_p^2 in Eqs. A.7, A.8 can be found from the sum rule $\int_0^\infty \sigma_1(\omega) d\omega = \omega_p^2/8$. Since $\sigma(\omega)$ is causal, $\lambda(\omega)$ and $1/\tau(\omega)$ are not independent and are related by the Kramers-Kronig relation. [Timusk89] Using the relations $1/\tau(\omega) = 1/\tau(-\omega)$ and $\lambda(\omega) = \lambda(-\omega)$ we obtain:

$$\lambda(\omega) = \frac{2}{\pi} \mathcal{P} \int_0^\infty \frac{1/\tau(\Omega)}{\Omega^2 - \omega^2} d\Omega \quad (\text{A.9})$$

$$1/\tau(\infty) - 1/\tau(\omega) = \frac{2}{\pi} \mathcal{P} \int_0^\infty \frac{\Omega^2 \lambda(\Omega)}{\Omega^2 - \omega^2} d\Omega \quad (\text{A.10})$$

If $1/\tau(\omega)$ and $\lambda(\omega)$ have no poles at $\omega = 0$ we immediately obtain the following useful relation:

$$1/\tau(\infty) - 1/\tau(0) = \frac{2}{\pi} \int_0^\infty \lambda(\Omega) d\Omega \quad (\text{A.11})$$

We see that the complex memory function $M(\omega)$ is a physical response function and experimental data can be presented in terms of $M(\omega, T)$ or the complex optical conductivity $\sigma(\omega, T)$ equally well. The particular choice should be made judging from the situation at hand. For example, the memory function analysis may be useful if one is interested in the relaxation processes that determine a system response to electromagnetic radiation. Also, in certain cases the memory function is easier to calculate analytically, thus making it easier to analyze the physics behind the system behavior using experimental results for $M(\omega)$. For example, simple analytical formulae for $M(\omega)$ have been derived for electron-phonon scattering while the optical conductivity has to be calculated numerically. [Shulga91]

Finally, we would like to stress that, although Eq. A.3 is very general, obviously the *interpretation* of experimental results for $M(\omega, T)$ in terms of scattering rate and mass enhancement only makes sense when a (generalized) Boltzmann equation can

be used. For example, if the optical response is determined by two distinct charge carrier systems (two-component), so that the optical conductivity takes form:

$$\sigma(\omega) = \sigma^I(\omega) + \sigma^{II}(\omega), \quad (\text{A.12})$$

the interpretation of $M'(\omega)$ and $M''(\omega)$ as a scattering rate and a mass enhancement is meaningless, as can be seen from Eq.'s A.7, A.8. This is the case if an interband transition is present in the same frequency region where there is an intraband response. We note however, that the form (A.12) can arise from a double-relaxation process (two different scattering mechanisms) as well. [Allen76]

Another example is the superconducting state at $T = 0$, when for a conventional superconductor $\sigma_1(\omega)$ is zero at all non-zero energies below 2Δ , where Δ is the superconducting gap. According to the Eq. A.7, $M'(\omega)$ is zero in the same energy range. However, this effect can not be meaningfully interpreted as a result of an infinite quasiparticle lifetime since there are no quasiparticles in this energy range. This is purely a density of states effect that has its origin in the redistribution of the one-particle density of states, with creation of a superconducting gap upon entering the superconducting state. This example shows that density of states may greatly influence the memory function and serves as another reminder that the *interpretation of $M(\omega)$ results purely in terms of the scattering rate and effective mass enhancement should be approached with extreme care.*

Since in the superconducting state $\sigma_1(\omega)$ is suppressed, the low-frequency optical conductivity is dominated by the imaginary term $\sigma_2(\omega) = \omega_{ps}^2/(4\pi\omega)$. In this case the low-frequency mass enhancement factor gives a ratio of the total plasma frequency, ω_p^2 , to the plasma frequency of the superconducting carriers, ω_{ps}^2 : $1 + \lambda(\omega) = \omega_p^2/\omega_{ps}^2$.

A.2 Electron-boson scattering.

Memory-function analysis has been most extensively developed for the case of electron-phonon scattering. [Allen76, Allen71, Shulga91] It can be shown in the limit of frequencies comparable to the Debye frequency and/or high enough temperature, the quasiparticle description breaks down. [Shulga91] Using more general many-body calculations Shulga *et al.* obtained the following expression for $1/\tau(\omega, T)$:

$$\frac{1}{\tau}(\omega, T) = \frac{\pi}{\omega} \int_0^\infty d\Omega \alpha_{tr}^2(\Omega) F(\Omega) [2\omega \coth\left(\frac{\Omega}{2T}\right) - (\omega + \Omega) \coth\left(\frac{\omega + \Omega}{2T}\right) + (\omega - \Omega) \coth\left(\frac{\omega - \Omega}{2T}\right)] + \frac{1}{\tau_{imp}}. \quad (\text{A.13})$$

Here $\alpha_{tr}^2(\Omega)F(\Omega)$ is a phonon density of states weighted by the amplitude for large-angle scattering on the Fermi surface and T is measured in frequency units. The last term in (13) represents impurity scattering. In the limit of zero temperature this reduces to Allen's result: [Allen71]

$$\frac{1}{\tau}(\omega) = \frac{2\pi}{\omega} \int_0^\omega d\Omega (\omega - \Omega) \alpha_{tr}^2(\Omega) F(\Omega) + \frac{1}{\tau_{imp}}. \quad (\text{A.14})$$

The dc scattering rate is obtained in the limit of $\omega = 0$ in Eq. A.13:

$$\frac{1}{\tau}(0, T) = \pi \int_0^\infty d\Omega \alpha_{tr}^2(\Omega) F(\Omega) \frac{\Omega}{T} \sinh^{-2}\left(\frac{\Omega}{2T}\right) + \frac{1}{\tau_{imp}}. \quad (\text{A.15})$$

At temperatures much higher than the phonon spectrum upper-energy cut-off, $T \gg \Omega_c$, the above expression reduces to:

$$\lim_{T/\Omega_c \rightarrow \infty} \frac{1}{\tau}(0, T) = 4\pi T \int_0^\infty d\Omega \frac{\alpha_{tr}^2(\Omega) F(\Omega)}{\Omega} + \frac{1}{\tau_{imp}}, \quad (\text{A.16})$$

which is just the familiar result that the high-temperature electron-phonon contribution to a dc resistivity is linear in temperature.

In the limit of high ω , $\omega \gg \Omega_c$,

$$\lim_{\omega/\Omega_c \rightarrow \infty} \frac{1}{\tau}(\omega, T) = 2\pi \int_0^\infty d\Omega \alpha_{tr}^2(\Omega) F(\Omega) \coth\left(\frac{\Omega}{2T}\right) + \frac{1}{\tau_{imp}}, \quad (\text{A.17})$$

which at high temperatures, $T \gg \Omega_c$, assumes the same value as the zero-frequency limit (A.16). Therefore, at very high temperatures the scattering rate becomes frequency-independent and the Eq. A.6 reduces to the classical Drude expression (A.1).

We note that the effective scattering rate $1/\tau(\omega)$ is different from the quasiparticle attenuation $\gamma(\omega)$. For example, at zero temperature $\gamma(\omega)$ is given by: [Allen71, Millis88]

$$\gamma(\omega) = -2\text{Im}\Sigma(\omega) = 2\pi \int_0^\omega d\Omega \alpha^2(\Omega) F(\Omega) + \frac{1}{\tau_{imp}}. \quad (\text{A.18})$$

Here $\alpha^2(\Omega)F(\Omega)$ is the isotropically weighted phonon density of states. One can see from Eq's A.14, A.18 that at $T = 0$ the effective scattering rate $1/\tau(\omega)$ is, if the difference between α_{tr}^2 and α^2 is neglected, an *average* of $\gamma(\omega)$ over frequencies from 0 to ω and therefore $\gamma(\omega)$ enters into the effective scattering rate in a way non-local in frequency. [Shulga91, Mori65, Allen71] As a consequence, $1/\tau(\omega)$ is actually equal to the quasiparticle attenuation $\gamma(\omega)$ only at $\omega = 0$, where $1/\tau(0) = \gamma(0) = 1/\tau_{imp}$. The two quantities also asymptotically approach each other in the limit of high frequencies, $\omega \gg \Omega_c$, where both $\gamma(\omega)$ and $1/\tau(\omega)$ become frequency-independent. As the temperature is increased, the difference between $\gamma(\omega)$ and $1/\tau(\omega)$ is smeared out, and in the limit of $T \gg \Omega_c$ they are asymptotically equal. Generally, however, $\tau(\omega, T)$ deviates from the quasi-particle lifetime $\gamma^{-1}(\omega, T)$.

Eq's. A.13, A.14, which have been derived for an electron-phonon scattering, are believed to be valid in the case of coupling of an electronic spectrum to any bosonic excitations. [Webb86, Dolgov95] In this case the Eliashberg function $\alpha_{tr}^2(\Omega)F(\Omega)$ in Eqs. A.13, A.14 is replaced by the corresponding, suitably weighted, bosonic spectral density $\mathcal{A}_{tr}(\Omega)$. To give a flavor of the results expected on the basis of Eq's A.13, A.14 we will perform calculations for several model shapes of $\mathcal{A}_{tr}(\omega)$: a δ -peak, a "square"-like spectrum and $\mathcal{A}_{tr}(\omega) = \Gamma\omega/(\Gamma^2 + \omega^2)$. The last spectrum is believed to be appropriate for scattering of electrons on spin fluctuations. [Millis90]

In the case of $\mathcal{A}_{tr}(\omega) = \omega_0\delta(\omega - \omega_0)$ the integration of Eq. A.13 can easily be done. The effective mass enhancement $\lambda(\omega)$ can be calculated using the Kramers-Kronig relation (9). As soon as both $1/\tau(\omega, T)$ and $\lambda(\omega, T)$ are known, the optical conductivity can be calculated using Eq. A.3. The impurity scattering has been set to $1/(2\pi\omega_0\tau_{imp}) = 0.01$. The results obtained are presented in Fig. A.1 at five different temperatures: $T = 0, 0.125\omega_0, 0.25\omega_0, 0.5\omega_0, \omega_0$.

For the two other choices of $\mathcal{A}_{tr}(\omega)$, the integration of Eq. A.13 was done numerically. We then used the Kramers-Kronig relation to obtain $\lambda(\omega, T)$. The same impurity scattering rate as in the case of δ -function was used to calculate $\sigma_1(\omega)$. The results are presented in Fig. A.2 and Fig. A.3 at different temperatures, measured in units of the characteristic frequency of bosonic spectrum $\mathcal{A}_{tr}(\omega)$.

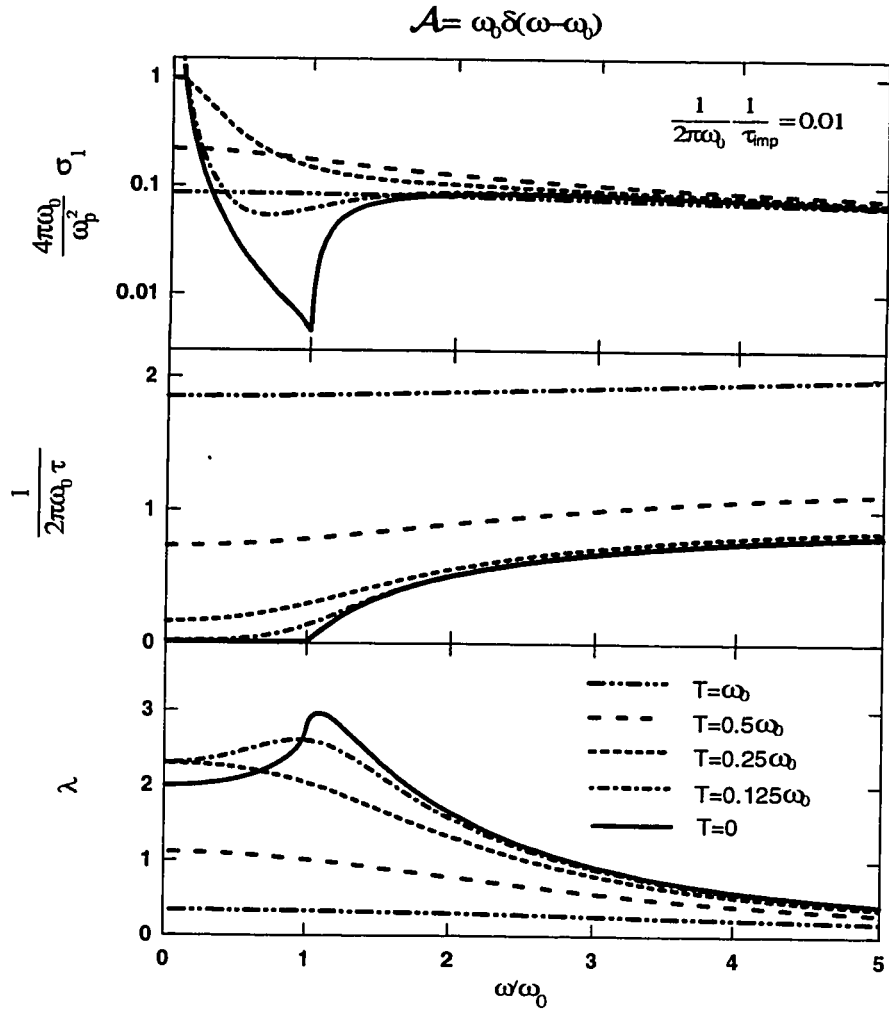


Figure A.1: Electron-boson model calculations with boson spectral density $\mathcal{A}_{tr}(\omega) = \omega_b \delta(\omega - \omega_b)$.

Top panel is the optical conductivity, middle panel is the scattering rate and bottom panel is the mass renormalization. The coupling constant is equal to 1.

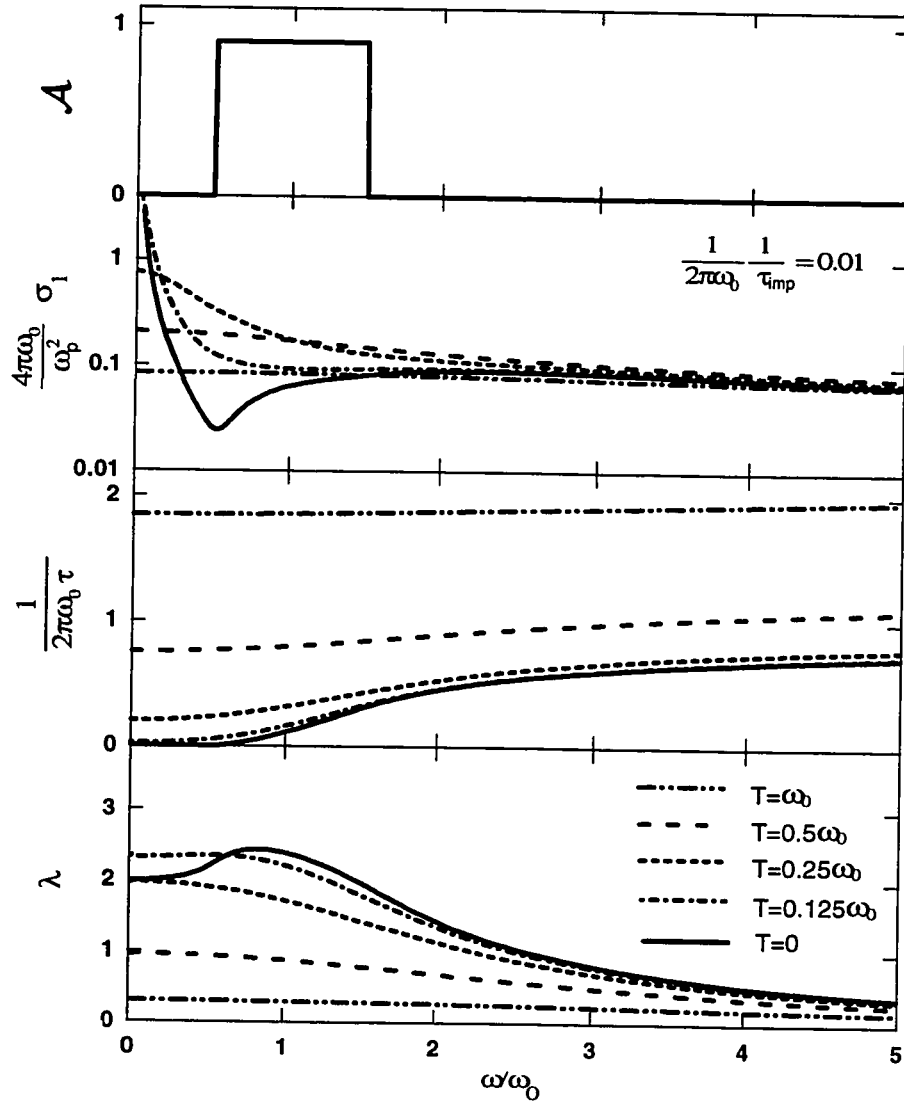


Figure A.2: Electron-boson model calculations with a "square" spectrum for the boson spectral density.

Top panel shows the bosonic spectral density, next panel is the real part of the optical conductivity, next panel is the scattering rate and bottom panel is the mass renormalization. The coupling constant is equal to 1.

As was discussed above, if the $\mathcal{A}_{tr}(\omega)$ spectrum has a high-energy cut-off, $1/\tau(\omega, T)$ saturates at frequencies that are much higher than the cut-off. The value of $1/\tau(\omega, T)$ in the saturation regime is strongly temperature-dependent, and linear in T at high enough temperatures according to (17). However, if there is no cut-off in $\mathcal{A}_{tr}(\omega)$, as in the case of magnetic spectrum in Fig. A.3, there is no high-frequency saturation of $1/\tau(\omega, T)$, rather it continues to increase. The temperature dependence of the absolute value of the scattering rate is, however, still strong.

In Fig. A.1, the effective mass enhancement $\lambda(\omega, T)$ is larger at low frequencies and decreases to zero at high frequencies. This has a simple physical interpretation that at high frequencies the boson "cloud" is not capable of following the charge carriers. The sharp increase in the low-temperature λ around the frequency of bosonic excitation ω_0 corresponds to the onset of boson-emission process, since only carriers with energy greater than $\hbar\omega_0$ can emit a boson. A similar onset can be seen in Fig. A.2. In the case of the magnetic $\mathcal{A}_{tr}(\omega)$, this feature is not observed since bosons can be emitted by a carrier with arbitrarily small energy. At high temperatures λ asymptotically approaches zero, in agreement with the frequency-independent scattering rate $1/\tau$.

The low-temperature conductivity in Fig. A.1 shows a pronounced absorption band, called a Holstein band, with a sharp onset at ω_0 . The band corresponds to an additional absorption channel associated with boson emission processes. Similar absorption onset can be seen in Fig. A.2 but not in Fig. A.3. The reason for this, as in the case of λ , is the large boson spectral density at all non-zero frequencies for the magnetic $\mathcal{A}_{tr}(\omega)$. As the temperature is increased, all sharp features in σ_1 are smeared out and at very high temperatures the conductivity can be described by a single Lorentzian of Eq. A.1.

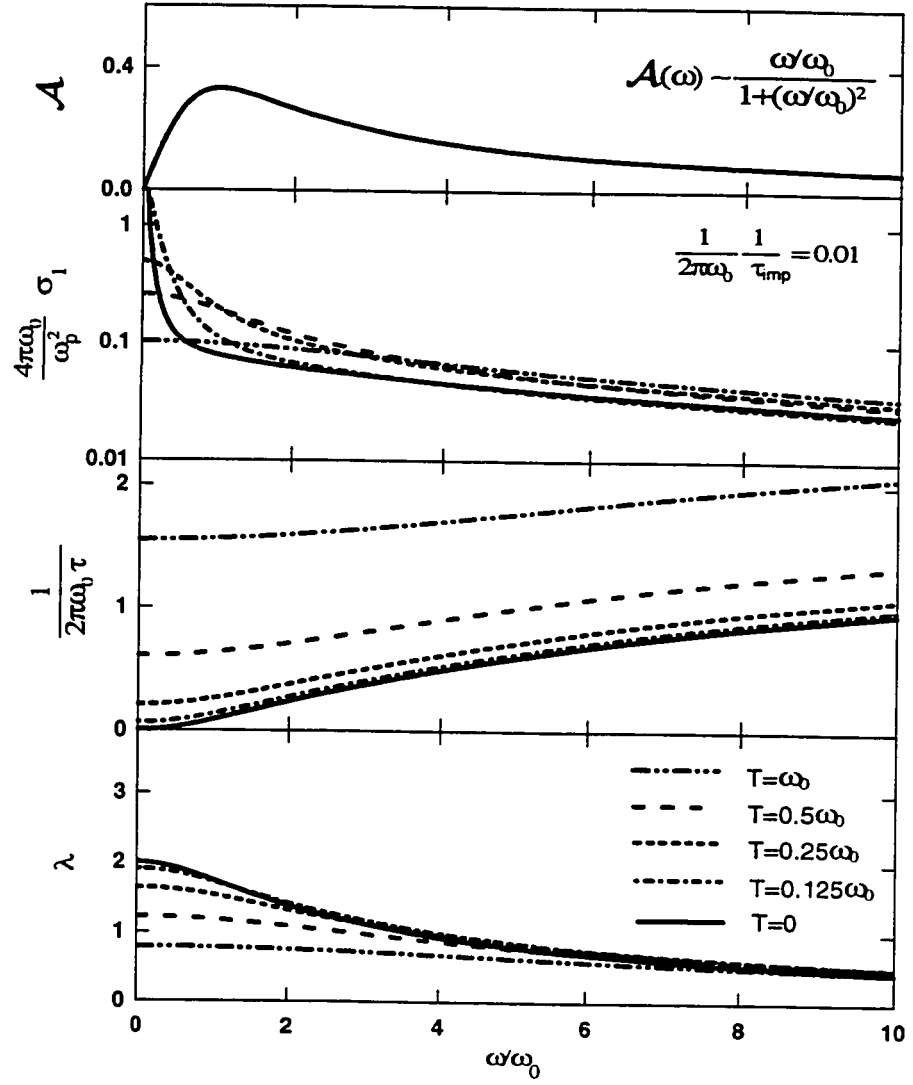


Figure A.3: Electron-boson model calculations for the "magnetic" boson spectral density.

Top panel shows the bosonic spectral density, $A_{tr}(\omega) \sim \Gamma\omega/(\Gamma^2 + \omega^2)$, next panel is the real part of the optical conductivity, next panel is the scattering rate, and bottom panel is the mass renormalization. The coupling constant is equal to 1.

Appendix B

Some useful information

B.1 Energy units:

$$1 \text{ eV} = 8065.5 \text{ cm}^{-1} = 2.41796 \times 10^{14} \text{ Hz} = 1160.4 \text{ K} = 1.602 \times 10^{-19} \text{ J}.$$

B.2 Material abbreviations:

$\text{YBa}_2\text{Cu}_3\text{O}_{7-\delta}$ (Y123)

$\text{YBa}_2\text{Cu}_4\text{O}_4$ (Y124)

$\text{Tl}_2\text{Ba}_2\text{CuO}_{6+\delta}$ (Tl2201)

$\text{Bi}_2\text{Sr}_2\text{CaCu}_2\text{O}_{8+\delta}$ (Bi2212)

$\text{Bi}_{2-x}\text{Pb}_x\text{Sr}_2\text{CaCu}_2\text{O}_{8+\delta}$ ((Bi/Pb)2212)

$\text{La}_{2-x}\text{Sr}_x\text{CuO}_4$ (La214)

$\text{Ba}_{1-x}\text{K}_x\text{BiO}_3$ (BKBO)

$\text{Ba}_{1-x}\text{Pb}_x\text{BiO}_3$ (BPBO)

Bibliography

- [Abrikosov75] Abrikosov A.A., L.P. Gorkov, and I.E. Dzyaloshinski, *Methods of Quantum Field Theory in Statistical Physics*, Dover Publications, New York, 1975.
- [Abrikosov93] Abrikosov A.A., J.C. Campuzano, and K. Gofron, *Physica C* **214**, 73 (1993).
- [Abrikosov94] Abrikosov A.A., *Physica C* **222**, 191 (1994).
- [Affronte93] Affronte M., J. Marcus and C. Escribe-Filippini, *Solid State Comm.* **85**, 501 (1993).
- [Alexandrov] Alexandrov A.S., V.V. Kabanov, and N.F. Mott, (unpublished)
- [Allen71] Allen P.B., *Phys. Rev. B* **3**, 305 (1971).
- [Allen76] Allen P.B., and J.C. Mikkelsen, *Phys. Rev. B* **15**, 2953 (1976).
- [Allen87] Allen P.B., W.E. Pickett, and H. Krakauer, *Phys. Rev. B* **36**, 3926 (1987).
- [Anderson73] Anderson P.W., *Mat. Res. Bull.* **8**, 153 (1973).
- [Anderson87] Anderson P.W., *Science* **235**, 1196 (1987).
- [Anderson90] Anderson P.W., *Phys. Rev. Lett.* **64**, 1839 (1990).
- [Ashcroft76] Ashcroft N.W., and N.D. Mermin, *Solid State Physics*, Saunders College, Philadelphia, 1976.

- [Bardeen57] Bardeen, J., L.N. Cooper, and J.R. Schrieffer, Phys. Rev. **108**, 1175 (1957).
- [Barzykin95] Barzykin V., and D. Pines, Phys. Rev. B **52**, 13585 (1995).
- [Basov94] Basov D.N., T. Timusk, B. Dabrowski and J.D. Jorgensen, Phys. Rev. B **50**, 3511 (1994).
- [Basov95] Basov D.N., H.A. Mook, B.Dabrowski, and T. Timusk, Phys. Rev. B **52**, R13141 (1995).
- [Basov96] Basov D.N., R. Liang, B. Dabrowski, D.A. Bonn, W.N. Hardy, and T. Timusk, preprint.
- [Batlogg88] Batlogg B., R.J. Cava, L.W. Rupp, Jr., A.M. Mujsce, J.J. Krajewski, J.P. Remeika, W.F. Peck, Jr., A.S. Cooper and G.P. Espinosa, Phys. Rev. Lett. **61**, 1670 (1988);
- [Batlogg89] Batlogg B., in *Mechnisms of High Temperature Superconductivity*, Editors: H. Kamimure, A. Oshiyama, Springer Series in Material Science, Vol. 11, p.342, 1989.
- [Batlogg94] Batlogg B., H.Y. Hwang, H. Takagi, R.J. Cava, H.L. Kao, and J. Kwo, Physica C **235–240**, 130 (1994).
- [Bednorz86] Bednorz J.G., and K.A. Müller, Z. Phys. B **64**, 189 (1986).
- [Blanton93] Blanton S.N., R.T. Collins, K.H. Kelleher, L.D. Rotter, Z. Schlesinger, D.G. Hinks and Z. Zheng, Phys. Rev. B **47**, 996 (1993).
- [Bonn88] Bonn D.A., J.D. Garret, and T. Timusk, Phys. Rev. Lett. **61**, 1305 (1988).
- [Bonn92] Bonn D.A., P. Dosanhi, R. Liang, and W.N. Hardy, Phys. Rev. Lett. **68**, 2390 (1992).
- [Bosovic90] Bosovic I., Phys. Rev. B **42**, 1969 (1990).

- [Bosovic92] Bosovic I., J.H. Kim, J.S. Harris, Jr., E.S. Hellman, E.H. Hartford, P.K. Chan, *Phys. Rev. B* **46**, 1182 (1992).
- [Bourges95] Bourges P., Y. Sidis, L.P. Regnault, B. Hennion, R. Villeneuve, G. Collin, C. Vettier, J.Y. Henry, and J.F. Marucco, *J. Phys. Chem Solids*, **56**, 1937 (1995).
- [Bucher93] Bucher B., P. Steiner, J. Karpinski, E. Kaldis, and P. Wachter, *Phys. Rev. Lett.* **70**, 2012 (1993).
- [Carbotte90] Carbotte J.P., *Rev. Mod. Phys.* **62**, 1027 (1990).
- [Carbotte95] Carbotte J.P., C. Jiang, D.N. Basov, and T. Timusk, *Phys. Rev. B* **51** 11798 (1995).
- [Jiang96] Jiang C., E. Schachinger, J.P. Carbotte, D. Basov, and T. Timusk, *Phys. Rev. B* **54**, 1264 (1996).
- [Cava89] Cava R.J., and B. Batlogg, *MSR Bull.* **14** (1), 49 (1989).
- [Chakravarty93] Chakravarty S., A. Suldø, P.W. Anderson, and S. Strong, *Science* **261**, 337 (1993).
- [Chen89] Chen Yi-Hong., F. Wilczek, E. Witten, and B.I. Halperin, *Int. J. Mod. Phys.* **3**, 1001 (1989).
- [Clarke95] Clarke D.G., S.P. Strong, and P.W. Anderson, *Phys. Rev. Lett.* **74**, 4499 (1995).
- [Collins90] Collins R.T., Z. Schlesinger, F. Holtzberg, P. Chaudhari, and C. Feild, *Phys. Rev. Lett.* **39**, 6571 (1990).
- [Cooper88] Cooper S.L., M.V. Klein, B.G. Pazol, D.M. Rice, and D.M. Ginsberg *Phys. Rev. B* **37**, 5920 (1988).
- [Cooper93] Cooper S.L., D. Reznik, A. Kotz, M.A. Karlow, R. Liu, M.V. Klein, W.C. Lee, J. Giapintzakis, D.M. Ginsberg, B.W. Veal, and A.P. Pulikas, *Phys. Rev. B* **47**, 8233 (1993).

- [Cooper94] Cooper S.L., and K.E. Gray in *Physical Properties of High Temperature Superconductors IV*, Donald M. Ginsberg, editor, (World Scientific, Singapore, 1994) p. 61.
- [Cox79] Cox D.E., and A.W. Sleight, *Acta Crystallogr. Sect. B* **35**, 1 (1979).
- [Dabrowskii] Dabrowski B., (unpublished).
- [Dabrowski92] Dabrowski B., K. Zhang, J.J. Pluth, J.L. Wagner, and D.G. Hinks, *Physica C* **202**, 271 (1992).
- [Ding96] Ding H., T. Tokoya, J.C. Campuzono, T. Takahashi, M. Randeria, M.R. Norman, T. Mochiku, K. Kadowaki, and J. Giapitzakis, *Nature* **382**, 51 (1996).
- [Dolgov95] Dolgov O.V., and S.V. Shulga, *J. of Superconductivity* **8**, 611 (1995).
- [Dunmore95] Dunmore F.J., H.D. Drew, E.J. Nicol, E.S. Hellman, E.H. Hartford, Preprint.
- [Egami94] Egami T., and S.J.L. Billinge, *Progress in Material Science* **38**, 359 (1994).
- [Emery95a] Emery V.J., and S.A. Kivelson, *Phys. Rev. Lett.* **74**, 3253 (1995).
- [Emery95b] Emery V.J., and S.A. Kivelson, *Nature* **374**, 434 (1995).
- [Fournier96] Fournier P., A. Kapitulnik, and A.F. Marshall, *Physica C* **257**, 291 (1996).
- [Friedl90] Friedl B., C. Thomsen, and M. Cardona, *Phys. Rev. Lett.* **76**, 1107 (1990).
- [Fukuyama92] Fukuyama H., *Prog. Theor. Phys. Supp.* **108**, 287 (1992).
- [Fukuzumi96] Fukuzumi Y., K. Mizuhashi, K. Takenaka, and S. Uchida, *Phys. Rev. Lett.* **76**, 684 (1996).

- [Gao93] Gao F., D.B. Romero, D.B. Tanner, J. Talvacchio, and M.G. Forrester, Phys. Rev. B **47**, 1036 (1993).
- [Glover56] Glover R.E., III, and M.Tinkham, Phys. Rev. **104**, 844 (1956).
- [Glover57] Glover R.E., III, and M.Tinkham, Phys. Rev. **108**, 243 (1957).
- [Götze72] Götze W., and P. Wölfe, Phys. Rev. B **6**, 1226 (1972).
- [Graebner89] Graebner I.E., L.F. Schneemeyer, and J.K. Thomas, Phys. Rev. B **39**, 9682 (1989).
- [Graf93] Graf M.J., D. Rainer, and J.A. Sauls, Phys. Rev. B **47**, 12089 (1995).
- [Gurvitch87] Gurvitch M., and A.T. Fiory, Phys. Rev. Lett. **59**, 1337 (1987).
- [Hardy93] Hardy W.N., D.A. Bonn, D.C. Morgan, R. Liang, and K. Zhang, Phys. Rev. Lett. **70**, 3999 (1993).
- [Hazen90] Hazen R.M., Crystal Structures of High-Temperature Superconductors, in *Physical Properties of High Temperature Superconductors II* D.M. Ginsberg, editor, (World Scientific, Singapore, 1990) pp. 121-198.
- [Hinks88] Hinks D.G., D.R. Richards, B. Dabrowski, D.T. Marx, and A.W. Mitchell, Nature **335**, 419 (1988).
- [Homes93a] Homes C.C., M.A. Reedyk, D.A. Crandles, and T. Timusk, Applied Optics **32**, 2976 (1993).
- [Homes93b] Homes C.C., T. Timusk, R. Liang, D.A. Bonn, and W.N. Hardy, Phys. Rev. Lett. **71**, 1645 (1993).
- [Homes95] Homes C.C., T. Timusk, R. Liang, D.A. Bonn, and W.H. Hardy, Physica C, **254**, 265-280, (1995).
- [Humliček90] Humliček J., E. Schmidt, L. Bočánek, M. Carriga, and M. Cardona, Solid State Comm. **73**, 127 (1990).

- [Ishida93] Ishida K., Y. Kitaoka, N. Ogata, T. Kamino, K. Asayama, and J.R. Cooper, *J. Phys. Soc. Jpn.* **62**, 2803 (1993).
- [Ito93] Ito T., K. Takenaka, and S. Uchida, *Phys. Rev. Lett.* **70**, 3995 (1993).
- [Ioffe93] Ioffe L.B., A.I. Larkin, A.A. Varlamov, L. Yu, *Phys. Rev. B* **47**, 8936 (1993).
- [Kamarás90] Kamarás K., S.L. Herr, C.D. Porter, N. Tache D.B. Tanner, S. Etemad, T. Venkatesan, E. Chase, A. Inham, X.D. Wu, M.S. Hegde, and B. Dutta, *Phys. Rev. Lett.* **64**, 84 (1990).
- [Kampf90] Kampf A.P., and J.R. Schrieffer, *Phys. Rev. B* **42**, 7967 (1990).
- [Karlo93] Karlow M.A., S.L. Cooper, A.L. Kotz, M.V. Klein, P.D. Han, D.A. Payne, *Phys. Rev. B.* **48**, 6499 (1993).
- [Katsufuji96] Katsufuji T., M. Kasai, and Y. Tokura, *Phys. Rev. Lett.* **76**, 126 (1996).
- [Kendziora93] Kendziora C., M.M. Martin, J. Hartge, and L. Mihaly, *Phys. Rev. B* **48**, 3531 (1993).
- [Kittel86] Kittel C., *Introduction to Solid State Physics*, John Wiley & Sons. Inc., (New York), 1986.
- [Kolesnikov95] Kolesnikov N.N., M.P. Kulakov, V.N. Molchanov, I.F. Schegolev, R.P. Shibaeva, V.I. Simonov, R.A. Tamazyan, and O.M. Vyasilev, *Physica C* **242**, 385 (1995).
- [Kostur96] Kostur V.N., *Phys. Rev. B* **53**, 2273 (1996).
- [Kotliar88] Kotliar G., and J. Liu, *Phys. Rev. B* **38**, 5142 (1988).
- [Kumar90] Kumar N., P.A. Lee, and B. Shapiro, *Physica A* **168**, 447 (1990).
- [Kumar92] Kumar N., and A.M. Jayannavar, *Phys. Rev. B* **50**, 438 (1992).

- [Landau84] Landau L.D., and E.M. Lifshits, *Electrodynamics of Continuous Media*, Pergamon (New York) (1984).
- [Laughlin88] Laughlin R.B., *Science* **242**, 525 (1988).
- [Lee92] Lee P.A., and N. Nagaosa, *Phys. Rev. B* **46**, 5621 (1992).
- [Leggett92] Leggett A.J., *Braz. J. Phys. B* **50**, 496 (1994).
- [Liang92] Liang R., P. Dosanih, D.A. Bonn, D.J. Baar, J.E. Carolan, and W.N. Hardy, *Physica C* **195**, 51 (1992).
- [Lynch85] Lynch D.W., Interband Absorption – Mechanisms and Interpretation, in *Handbook of Optical Constants*, E.D. Palik, Editor (Academic Press, 1985).
- [Litvinchuk92] Litvinchuk A.P., C. Thomsen, and M. Cardona, *Solid State Comm.* **83**, 343 (1992).
- [Loong91] Loong C.-K., D.G. Hinks, P. Vashishta, W. Jin, R.K. Kalia, M.H. Degani, D.L. Price, J.D. Jorgensen, B. Dabrowski, A.W. Mitchell, D.R. Richards, Y. Zheng, *Phys. Rev. Lett.* **66**, 3217 (1991).
- [Loram94] Loram J.W., K.A. Mirza, J.R. Cooper, and W.Y. Liang, *J. of Superconductivity*, **7**, 261 (1994).
- [Loeser96] Loeser A.G., Z.-X. Shen, D.S. Dessau, D.S. Marshall, C.H. Park, P. Fournier, and A. Kapitulnik, *Science* **273**, 325 (1996).
- [Manako92] Manako T., Y. Kubo, and Y. Shimakawa, *Phys. Rev. B* **46**, 11019 (1992).
- [Marshall96] Marshall D.S., D.S. Dessau, A.G. Loeser, C.H. Park, Z.-X. Shen, A.Y. Matsuura, J.N. Eckstein, I. Bozovik, P. Fournier, A. Kapitulnik, W.E. Spicer, and Z.-X. Shen, *Phys. Rev. Lett.* **76**, 4841 (1996).
- [Marsiglio95] Marsiglio F., and J.P. Carbotte, *Phys. Rev. B* **52**, 16192 (1995).

- [Marsiglio96] Marsiglio F., unpublished.
- [Mattheiss83] Mattheiss L.F., and D.R. Hamann, *Phys. Rev. B* **28**, 4227 (1983).
- [Mattheiss88] Mattheiss L.F., E.M. Gyorgy, and D.W. Johnson, Jr., *Phys. Rev. B* **37**, 3745 (1988).
- [Mattis58] Mattis D.C., and J. Bardeen, *Phys. Rev.* **111**, 412 (1958).
- [Micnas90] Micnas R., J. Ranninger, and S. Robaszkiewicz, *Rev.Mod. Phys.* **62**, 113 (1990).
- [Millis88] Millis A.J., S. Sachdev, and C.M. Varma, *Phys. Rev. B* **37**, 4975 (1988).
- [Millis90] Millis A.J., H. Monien, and D. Pines, *Phys. Rev. B* **42**, 167 (1990).
- [Montoux92] Monthoux P., and D. Pines, *Phys. Rev. Lett.* **69**, 961 (1992).
- [Mori65] Mori H., *Prog. Theor. Phys.* **34**, 399 (1965).
- [Mott90] Mott N.F., *Adv. Phys.* **39**, 55 (1990).
- [Niedermayer93] Niedermayer Ch., C. Bernhard, U. Binniger, H. Glücker, J.L. Tallon, E.J. Ansaldo, J.I. Budnick, *Phys. Rev. Lett.* **71**, 1764 (1993).
- [Nyhus95] Nyhus P., M.A. Karlow, S.L. Cooper, B. Veal, and A.P. Paulikas, *Phys. Rev. B* **50**, 13898 (1994).
- [Obertelli92] Obertelli S.D., J.R. Cooper, and J.L. Tallon, *Phys. Rev. B* **46**, 14928 (1992).
- [Ong87] Ong N.P., Z.Z. Wang, J. Clayhold, J.M. Tarascon, L.H. Green, and W.R. McKinnon, *Phys. Rev. B* **35**, 8807 (1987).
- [Orenstein90] Orenstein J., G.A. Thomas, A.J. Millis, S.L. Cooper, D. Rapkine, T. Timusk, L.F. Schneemeyer, and J.V. Waszczak, *Phys. Rev. B* **42**, 6342 (1990).

- [Palik85] Handbook of Optical Constants, E.D. Palik, Editor (Academic Press, 1985).
- [Pei90] Pei S., J.D. Jorgensen, B. Dabrowski, D.G. Hinks, D.R. Richards, A.W. Mitchell, J.M. Newsam, S.K. Sinha, D. Vaknin and A.J. Jacobson, Phys. Rev. B **41**, 4126 (1990).
- [Perkins93] Perkins J.D., J.M. M.A. Kastner, R.J. Birgenau, J.P. Falck, M. Greven, Phys. Rev. Lett. **71**, 1621 (1993).
- [Pickett92] Singh D.J., and W.E. Pickett, Physica C **203**, 193 (1992).
- [Pines94] Pines D., Physica C **235-240**, 113 (1994).
- [Pines96] Pines D., and P. Nozieres, *The Theory of Quantum Liquids*, Benjamin, New York, 1966.
- [Presland91] Presland M.R., J.L. Tallon, R.G. Buckley, R.S. Liu, and N.E. Flower, Physics C **176**, 95 (1991).
- [Puchkov95a] Puchkov A.V., T. Timusk, W.D. Mosley, R.N. Shelton, Phys. Rev. B. **50**, 4144 (1995).
- [Puchkov95b] Puchkov A.V. *et al.*, unpublished; A.V. Puchkov, T. Timusk, S. Doyle, and A.M. Hermann, Phys. Rev. B **51**, 3312 (1995).
- [Puchkov95c] Puchkov A.V., T. Timusk, M.A. Karlow, S.L. Cooper, P.D. Han, and D.A. Payne, Phys. Rev. B **52**, R9855 (1995).
- [Puchkov96a] Puchkov A.V., T. Timusk, M.A. Karlow, S.L. Cooper, P.D. Han, and P.A. Payne, Phys. Rev. B. **54**, 6686 (1996).
- [Puchkov96b] Puchkov A.V., P. Fournier, T. Timusk, and N.N. Kolesnikov, Phys. Rev. Lett. **77**, 1853 (1996).
- [Puchkov96c] Puchkov A.V., P. Fournier, D.N. Basov, T. Timusk, A. Kapitulnik, and N.N. Kolesnikov, Phys. Rev. Lett. **77**, 3212, (1996).

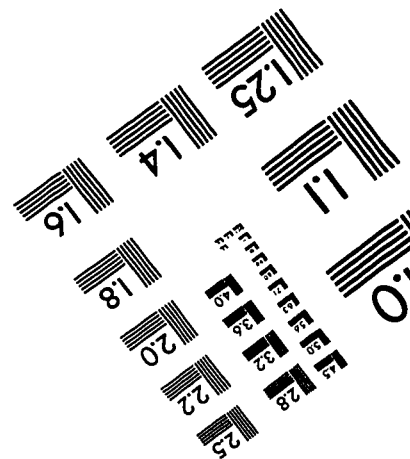
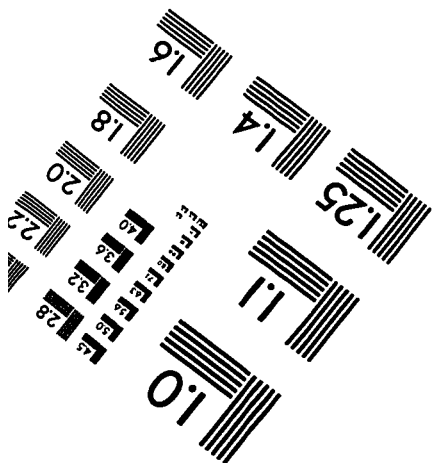
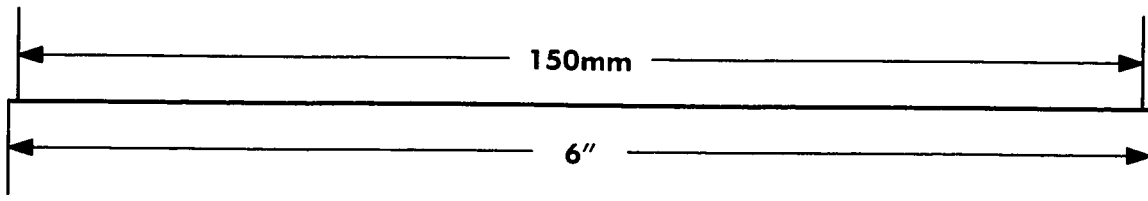
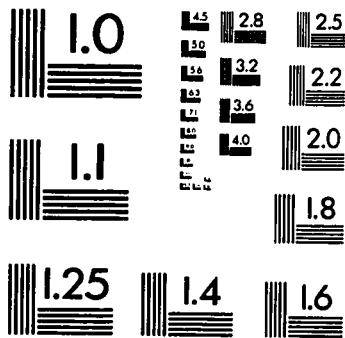
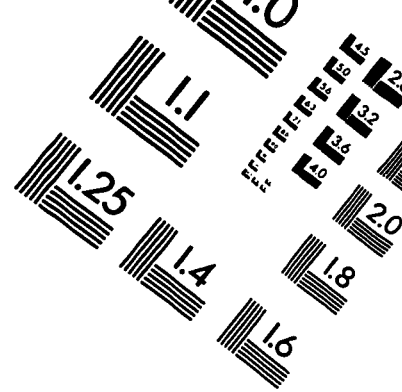
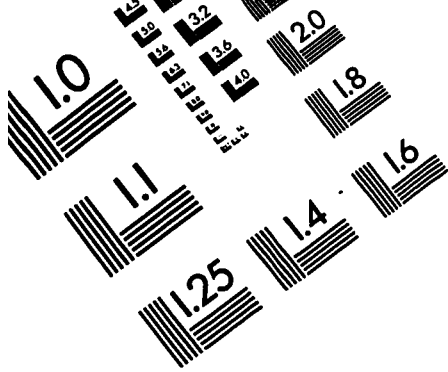
- [Puchkov96d] Puchkov A.V., D.N. Basov, and T. Timusk, submitted to *J. Phys. Cond. Matt* (1996).
- [Quinlan96] Quinlan S.M., P.J. Hirshfeld, and D.J. Scalapino, *Phys. Rev. B* **53**, 8575 (1996)
- [Reedyk88] Reedyk M., D.A. Bonn, J.D. Garrett, J.E. Greedan, C.V. Stager, T. Timusk, K. Kamarás, and D.B. Tanner, *Phys. Rev. B* **38**, 11981 (1988).
- [Reedyk92] Reedyk M., and T. Timusk, *Phys. Rev. Lett.* **69**, 2705 (1992).
- [Reedyk96] Reedyk M., (unpublished).
- [Renker88] Renker B., F. Gompf, E. Gering, D. Ewert, H. Rietschek, and A. Dianoux, *Z. Phys. B – Cond. Matt.* **73**, 309 (1988).
- [Rieck95] Rieck C.T., W.A. Little, J. Ruvalds, and A. Virosztek, *Phys. Rev. B* **51**, 3772 (1995).
- [Rice92] Rice T.M., in *The Physics and Chemistry of Oxide Superconductors*, edited by Y. Iye and H. Yasuoka (Springer-Verlag, Berlin, 1992), p. 313.
- [Romero92] Romero D.B., C.D. Porter, D.B. Tanner, L. Forro, D. Mandrus, L. Mihaly, G.L. Carr, and G.P. Williams, *Phys. Rev. Lett.* **68**, 1590 (1992).
- [Rossat-Mignod91] Rossat-Mignod J., L.P. Regnault, C. Vettier, P. Bourges, P. Burlet, J. Bossy, J.Y. Henry, and G. Lapertot, *Physica C* **185-189**, 86 (1991).
- [Rotter91] L.D. Rotter, Z. Schlesinger, R.T. Collins, F. Holtzberg, C. Feild, U. Welp, G.W. Crabtree, J.Z. Liu, Y. Fang, K.G. Vandervoort, and S. Flesher *Phys. Rev. Lett.* **67**, 2741 (1991).
- [Rojo93] Rojo A.G., and K. Levin, *Phys. Rev. B* **48**, 16861 (1993).

- [Sato89] Sato H., S. Tajima, H. Takagi, and S. Uchida, *Nature* **338**, 241 (1989).
- [Sato90] Sato H., H. Takagi and S. Uchida, *Physica C* **169**, 391 (1990).
- [Sato93] Sato H., T. Ido, S. Uchida, S. Tajima, M. Yoshida, K. Tanabe, K. Tatsuhara, N. Miura, *Phys. Rev. B* **48**, 6617 (1993).
- [Schlesinger89] Schlesinger Z., R.T. Collins, J.A. Calise, D.G. Hinks, A.W. Mitchell, Y. Zheng, B. Dabrowski, N.E. Bickers, and D.J. Scalapino, *Phys. Rev. B* **40**, 6862 (1989).
- [Schlesinger90] Schlesinger Z., R.T. Collins, F. Holtzberg, C. Feild, S.H. Blanton, U. Welp, G.W. Crabtree, Y. Fang, and J.Z. Liu, *Phys. Rev. Lett.* **65**, 801 (1990).
- [Schlesinger94] Schlesinger Z., R.T. Collins, L.D. Rotter, F. Holtzberg, C. Field, U. Welp, G.W. Grabtree, J.Z. Liu, Y. Fang, K.G. Vandervoort, and S. Fleshler, *Physica C* **235-240**, 49 (1994).
- [Schmitt-Rink88] Schmitt-Rink S., C.M. Varma, and A.E. Ruckenstein, *Phys. Rev. Lett.* **60**, 2793 (1988).
- [Sharifi91] Sharifi F., A. Pargellis, and R.C. Dynes, *Phys. Rev. Lett.* **67**, 509 (1991).
- [Shulga91] Shulga S.V., O.V. Dolgov, and E.G. Maksimov, *Physica C* **178**, 266 (1991).
- [Slakey90] Slakey F., M.V. Klein, J.P. Rice, and D.M. Ginsberg, *Phys. Rev. B* **42**, 2643 (1990).
- [Smith85] Smith D.Y., Dispersion theory, Sum Rules, and Their Application to the Analysis of Optical Data, in *Handbook of Optical Constants*, E.D. Palik, Editor (Academic Press, 1985).
- [Startseva] Startseva T., R.A. Hughes, A.V. Puchkov, D.N. Basov, T. Timusk, and H.A. Mook, (unpublished).

- [Sugai89] Sugai S., Y. Yntomoto, and T. Murakami, *Sol. State Comm.* **72**, 1193 (1989).
- [Stromer88] Stormer H.L., A.F.J. Levi, K.W. Baldwin, M. Anzlowar, and G.S. Boebinger, *Phys. Rev. B* **38**, 2472 (1988).
- [Tajima95] Tajima S., J. Schützmann, and S. Miyamoto, *Solid State Comm.* **95**, 759 (1995).
- [Takagi92] Takagi H., B. Batlogg, H.L. Kao, J. Kwo, R.J. Cava, J.J. Krajewski, and W.F. Peck, Jr., *Phys. Rev. Lett.* **69**, 2975 (1990).
- [Takegahara94] Takegahara K., *J. Electron Spectrosc. Relat. Phenom.* **66**, 303 (1994).
- [Takigawa91] Takigawa M., A.P. Reyes, P.C. Hammel, J.D. Thompson, R.H. Heffner, Z. Fisk, and K.C. Ott, *Phys. Rev. B* **43**, 247 (1991).
- [Tallon95] Tallon J.L., *Phys. Rev. B* **51**, 12911 (1995).
- [Tamasaku94] Tamasaku K., T. Ito, T. Takagi, and S. Uchida, *Phys. Rev. Lett.*, **72**, 3088 (1994).
- [Tanner92] Tanner D.B., and T. Timusk, *Optical Properties of High-Temperature Superconductors*, in *Physical Properties of High Temperature Superconductors III* D.M. Ginsberg, editor, (World Scientific, Singapore, 1992) p. 105.
- [Timusk88] Timusk T., S.L. Herr, K. Kamarás, C.D. Porter, D.B. Tanner, D.A. Bonn, J.D. Garrett, C.V. Stager, J.E. Greedan, and M. Reedyk, *Phys. Rev. B* **38**, 6683, (1988).
- [Timusk89] Timusk T., and D.B. Tanner, *Infrared Properties of High T_c Superconductors*, in *Physical Properties of High Temperature Superconductors I* D.M. Ginsberg, editor, (World Scientific, Singapore, 1989) p. 339.

- [Timusk91] Timusk T., C.D. Porter, and D.B. Tanner, Phys. Rev. Lett. **66**, 663 (1991).
- [Tinkham80] Tinkham M., *Introduction to Superconductivity*, Robert E. Krieger Publishing Company (Malabar, Florida), (1980).
- [Thomas88] Thomas G.A., J. Orenstein, D.H. Rapkine, M. Capizzi, A.J. Millis, R.N. Bhatt, L.F. Schneemeyer, and J.V. Waszczak, Phys. Rev. Lett. **61**, 1313 (1988).
- [Thomas91] Thomas G.A., D.H. Rapkine, S.L. Cooper, S.-W. Cheong, and A.S. Cooper Phys. Rev. Lett. **67**, 2906, (1991).
- [Tranquada92] Tranquada J.M., P.M. Gehring, G. Shirane, S. Shamoto, and M. Sato, Phys. Rev. **B 46**, 5561 (1992).
- [Marel91] van der Marel D., H.-U. Habermeier, D. Heitmann, W. König, and A. Wittlin, Physica C **176**, 1 (1991).
- [Uchida96] Uchida S., K. Tamasaku, and S. Tajima, Phys. Rev. B **53**, 14558, (1996).
- [Uemura89] Uemura Y.J., G.M. Luke, B.J. Sternlieb, J.H. Brewer, J.F. Carolan, W.N. Hardy, R. Kadono, J.R. Kempton, R.F. Kiefl, S.R. Kreitzman, P. Mulhern, T.M. Riseman, D.Ll. Williams, B.X. Yang, S. Uchida, H. Takagi, J. Gopalakrishnan, A.W. Sleight, M.A. Subramanian, C.L. Chien, M.Z. Cieplak, G. Xiao, V.Y. Lee, B.W. Statt, C.E. Stronach, W.J. Kossler, and X.H. Yu, Phys. Rev. Lett. **62**, 2317 (1989).
- [Uemura91] Uemura Y.J., L.P. Le, G.M. Luke, B.J. Sternlieb, W.D. Wu, J.H. Brewer, T.M. Riseman, C.L. Seaman, M.B. Maple, M. Ishikawa, D.G. Hinks, J.D. Jorgensen, G. Saito, and H. Yamochi, Phys. Rev. Lett. **66**, 2665 (1991).

- [Walkes93] Walkes D.R., A. Carrington, A.P. Mackenzie, and J.R. Cooper, (unpublished), cited in M. Gabay, and P. Lederer, *Phys. Rev. Lett.* **47**, 14462 (1993).
- [Warren89] Warren W.W., Jr., R.E. Walstedt, G.F. Brennert, R.J. Cava, R. Tycko, R.F. Bell, and G. Dabbagh, *Phys. Rev. Lett.* **62** 1193, (1989).
- [Webb86] Webb B.C., A.J. Sievers, and T. Mihalisin, *Phys. Rev. Lett* **57**, 1951 (1986).
- [Wen96] Wen X.-G., and P. Lee, *Phys. Rev. Lett.* **76**, 503 (1996).
- [Wooten72] Wooten F., *Optical properties of solids*, Academic Press (New York), 1972.
- [Yoshinari90] Yoshinari Y., H. Yasuoka, Y. Ueda, K. Koga, and K. Kosuge, *J. Phys. Soc. Jpn.* **59**, 3698 (1990); H. Alloul, T. Ohno, and P. Mendels, *J. Less-Common Met.* **164-165**, 1022 (1990).
- [Yu92] Yu R.C., M.B. Salamon, J.P. Lu, and W.C. Lee, *Phys. Rev. Lett.* **69**, 1431 (1992).
- [Zasadzinski89] Zasadzinski J.F., N. Tralshawala, D.G. Hinks, B. Dabrowski, A.W. Mitchell, D.R. Richards, *Physica C* **158**, 519 (1989).
- [Zhang94] Zhang K., D.A. Bonn, S. Kamal, R. Liang, D.J. Baar, W.N. Hardy, D. Basov, and T. Timusk, *Phys. Rev. Lett.* **73**, 2484 (1994).
- [Zheng93] Zheng G., T. Odaguchi, T. Mito, U. Kitaoka, K. Asayama, Y. Kodama, *J. Phys. Soc. Jpn.* **62**, 2591 (1993).



APPLIED IMAGE, Inc
1653 East Main Street
Rochester, NY 14609 USA
Phone: 716/482-0300
Fax: 716/288-5989

© 1993, Applied Image, Inc., All Rights Reserved